TECHNISCHE UNIVERSITÄT MÜNCHEN
Lehrstuhl für Turbomaschinen und Flugantriebe

Numerical Investigation of Combustion Characteristics in GO2/GCH4 Combustors with Reaction Mechanisms

Ye Hong

Vollständiger Abdruck der von der Fakultät für Maschinenwesen der Technischen Universität München zur Erlangung des akademischen Grades eines

Doktor -Ingenieurs

genehmigten Dissertation.

Vorsitzender: Priv.-Doz. Dr.-Ing. habil. Xiangyu Hu

Prüfer der Dissertation:

1. Prof. Dr. -Ing. Oskar J. Haidn
2. Prof. Dr. -Ing. Thomas Sattelmayer

Die Dissertation wurde am 05.09.2019 bei der Technischen Universität München eingereicht und durch die Fakultät für Maschinenwesen am 04.12.2019 angenommen.

Zusammenfassung

Durch den steigenden Wettbewerb auf dem Markt für Raumträgersysteme, messen immer mehr Wissenschaftler dem Methan als potentieller Treibstoff hohen Wert zu. Zum Zwecke der Entwicklung von Methan/Sauerstoff-Raketentriebwerken, wurden CFD-Simulationen weitgehend modifiziert, um die Kosten und Dauer der Auslegung zu senken. Für die Simulation von Reaktionsprozessen sind Reaktionsmechanismen unverzichtbar. Der GRI-Mech 3.0 wurde reduziert auf 22-Species und 58 Reaktionen. Die dazu verwendeten Methoden sind Sensitivitätsanalysen der Reaktionspfade und der Reaktionsraten. Die Reduktion wurde für einen spezifischen Betriebsbereich der ROF und Brennkammerdruck ausgelegt. Die Validierung erfolgte auf Basis der Kriterien der Zündverzögerung und der laminaren Flammenfrontgeschwindigkeit. Ferner stimmen die mit dem Mechanismus errechneten Simulationsresultatemit den Experimentalwerten überein. Die Abweichung zwischen der simulierten und gemessenen Druck- und Wärmestromverteilung ist nur gering. Ebenso wurde der Mechanismus sowohl mit dem EDC- als auch dem Flamelet-modell für eine GO2/GCH4-Verberennung getestet. Ein Vergleich zeigt, dass er mit dem EDC-Modell präzisere Resultate liefert. Der Grund dafür liegt in den zugrundeliegenden Annahmen und Transportgleichungen der Modelle.

Abstract

Given growing competition in the business space launch market, more researchers are evaluating the merit of methane as a potential propellant. Due to the need for the development of oxygen/methane rocket engines, computational fluid dynamics simulations are extensively adopted to lower the cost and shorten the design cycle. To simulate the reaction process in the combustion chambers, reaction mechanisms are indispensable. A 22-species, 58-step skeletal mechanism is reduced from GRI-Mech 3.0 based on the reaction path and reaction rate sensitivity analyses under the specification of operating pressure and ratio of oxidizer to fuel. The skeletal mechanism is validated against experimental data for ignition delay time and premixed laminar flame speed. The simulation results with the mechanism are in accordance with experimental results. The mechanism then is also taken into account in the EDC model and flamelet model for simulations of the combustion in a GO2/GCH4 combustor. The mechanism predicts pressure and heat flux in close agreement with the test results. Comparisons between the simulation results of EDC Mechanism 101 and flamelet Mechanism 101 indicate the EDC model predicts more precise results than the flamelet model, theoretically due to the models' assumptions and transport equations.

Acknowledgements

At the beginning of this dissertation, I would like to express my sincere thanks for the people who have helped me over the past five years. Without their assistance, guidance and support, I could not have finished the work of this dissertation.

I am extremely grateful for Professor Haidn's kind instruction, illuminating discussions and great encouragement during my studies. He enabled me to conduct research in this cross-subject field, involving the integration of different knowledge, and represented me an excellent example of a successful engineer. Furthermore, I would like to acknowledge my mentor, Dr. Paulo A. Beck, for his valuable discussions and ideas for my simulation. In addition, I sincerely appreciate Professor Thomas F. Sattelmayer's insightful and helpful comments for improvements, and PD Hu's work as a chairman of an examining board.

My colleagues' precious support and assistance over the past five years will be always remembered. I especially thank Meng Luo for his heartfelt advice and gentle accompany throughout the entire five years. I would also like to acknowledge Christian Bauer, Christof Roth, Nikolaos Perakis, Andrej Sternin, Julian Pauw, Hao Ma, Hongxin Wang, Jianing Liu, Yongchuan Yu, Zhendong Yu, Chengyu Zhang and Bin Dai for their fruitful discussions and amazing abilities to solve my problems. The pleasure collaboration and patient explanations from Simona Silvestri, Maria P. Celano, Fernanda Winter, Paul Lungu, Christoph von Sethe are also greatly appreciated. I extend my thanks to Professor Xianggeng Wei, who generously shared with me his vast experience in research, in career and in life during his visiting time here.

Contents

Nomenclature

Acronyms

CFD	Computational Fluid Dynamics
DNS	Direct Numerical Simulation
EDC	Eddy Dissipation Concept
LES	Large Eddy Simulation
LH_2	Liquid Hydrogen
LOX	Liquid Oxygen
MMH	Monomethyl Hydrazine
NTO	Nitrogen-tetroxide
RAMEC	RAM accelerator MEChanism
RANS	Reynolds-Averaged Navier-Stokes
REDRAM	REDuced RAM accelerator mechanism
PSR	Perfectly Stirred Reactor
SGS	Sub-grid Scale
UDMH	Unsymmetrical Dimethyl-hydrazine

Symbols

A_e	Exit area	m^2
A_{th}	Throat area	[m^2]
c_{eff}	Effective exhaust velocity	[m/s]
c_F	Thrust coefficient	[-]
c_p	Specific heat at constant pressure	[J/(kg· K)]
$\overline{C}_P^0$	Molar heat capacities	[J/(mol·K)]
c^*	Characteristic velocity	[m/s]
$\overline{G}^0$	Molar Gibbs energy	[kJ/mol]
$\overline{H}^0$	Molar enthalpy	[kJ/mol]
k	Specific heat ratio	[-]
K_p	Equilibrium constant	[-]
I_{sp}	Specific impulse	[s]
λ	Heat conductivity	[W/(m·K)]
$\dot{m}$	Mass flow rate of propellants	[Kg/s]
M_a	Mach number	[-]
p_a	Total pressure at exit	[Pa]
Φ	Equivalence ratio	[-]
Pr_t	Turbulent Prandtl number	[-]
p_c	Total pressure in the throat	[Pa]
v_e	Exit velocity	[m/s]
φ_{ch}	Chamber coefficient	[-]
R′	Universal gas constant	[J/(kmol·K)]
$\overline{S}^0$	Molar entropy	[J/(mol·K)]
Sc_t	Turbulent Schmidt number	[-]
τ_{ign}	Ignition delay time	[s]

List of Figures

List of Tables

1. Introduction

Given growing competition in the business space launch market, more and more researchers are evaluating the merit of methane as a potential propellant. Methane is safer, cheaper and more easily produced compared with currently used propellants. Commonly used liquid propellants are monomethyl hydrazine/nitrogen-tetroxide (MMH/NTO), unsymmetrical dimethyl-hydrazine/nitrogen-tetroxide (UDMH/NTO), liquid oxygen/liquid hydrogen (LOX/LH_2) and LOX/kerosene. Because of MMH/NTO and UDMH/NTO's toxicity and rising cost, methane is a promising substitute. In terms of cost, the replacement of liquid hydrogen with methane would reduce the total launch expense. Admittedly, methane has a lower specific impulse (~350s) than liquid hydrogen (451s). However, usually liquid hydrogen needs large fuel tanks and more complex insulation systems, thus, incurring higher costs than methane, because of liquid hydrogen's low density (70.85g/L) and boiling point (~21K). Compared with kerosene, methane is a more promising candidate for reusable engines because it not only has a lower cost, but also more 10s I_{sp}, better cooling performance, a lower pressure loss in cooling channels, higher coking temperature (950K) and less soot formation [1]. Equal heat flux can be taken away by methane, with half the flow rate of kerosene. This means, methane can more easily solve the problems of limited cooling ability and coking temperature range, that engineers must face when kerosene is used. Moreover, the cost of methane is only one-third that of kerosene [2]. In addition, space propulsion usually requires high-quality kerosene, whose reserve is low. Oppositely, methane, the main component of natural gas, exists widely on Earth. Furthermore, methane has also been found on Mars. Exploiting or manufacturing it there from CO_2 would provide a possible way to solve the refueling problem of a return journey from Mars.

Usually, chamber designs and performance evaluations of a new type of rocket engine require a series of development tests. To reduce the expense of this process, Computational Fluid Dynamics (CFD) simulations are commonly used. CFD simulations significantly cut the number of laboratory experiments and shorten the design cycles. In addition, CFD simulations inform designs of the combustion process in detail. In order to meet the needs of CFD simulations of combustion, reaction mechanisms have been developed and reduced by many studies during the past decades. Reaction mechanisms are categorized into global mechanisms, detailed mechanisms and reduced mechanisms. Several studies of methane chemical kinetics have been conducted and several detailed mechanisms have been generated. GRI Mech 3.0 [3] contains 53 species and 325 reactions. Aramco Mech 1.3 [4] includes 253 species and 1,542 reactions. Zhukov's Mech C1-C4 [5] involves 207 species and 2,329 reactions. Because of computational resource limits, detailed mechanisms are unaffordable for engineering applications. There are also many reduced mechanisms. Due to different application targets, usually the mechanisms are reduced under different assumptions.

Until now no oxygen/methane rocket engine has flown. Unresolved issues remain between the fundamental research and technology developments, and a final practical application. Therefore, detailed knowledge about heat transfer characteristics in such combustion chambers is among the most important issues, and some research work has

been done. Within the framework of the national research program Transregio SFB/TR-40 on “Technological Foundations for the Design of Thermally and Mechanically Highly Loaded Components of Future Space Transportation Systems”, a series of studies concerning mixing processes, chemical kinetics, heat fluxes on the wall, pressure distribution, interaction between turbulent mixing and chemical kinetics, and other aspects have been undertaken at the Institute of Turbomachinery and Flight Propulsion at the Technical University of Munich. Additionally, the continuously growing pressure for cost reduction has forced the aerospace industry to reduce as much as possible trial-and-error approaches, which include expensive experimental testing programs and rely more and more on advanced numerical design tools. Therefore, the numerical simulation has been combined in our effort with experimental results to investigate key phenomena occurring in combustion chambers. In this dissertation, a new skeletal mechanism is reduced from GRI 3.0 and validated against a test case from LTF. Furthermore, corresponding numerical simulation investigations are conducted. This dissertation comprises four parts. The fundamentals of rocket propulsion are briefly described first. The second section provides a brief description of the numerical simulation method. Then the sensitivity analysis approach to obtain the reduced mechanism, Mechanism 101, from the GRI 3.0 is introduced, and the final fourth part is dedicated to the comparisons among different modelling and testing results.

2. Basics of the Rocket Propulsion

2.1 Definitions and Fundamentals

The principles that apply to rocket engines propelled by chemicals, as well as the nomenclature of rocket propulsion, will be described and discussed below.

2.1.1 Thrust

Aero propulsion compares to space propulsion in that they both rely on chemical reactions; however, the latter is propelled by rocket engines whose liquid propellants have minimal inflow momentum. The rockets operate under a basic principle: that an engine can generate propulsion by the gas exhausted at a high velocity while conserving the momentum. Figure 2.1 demonstrates a combustion chamber with a nozzle, through which the propellant is exhausted.

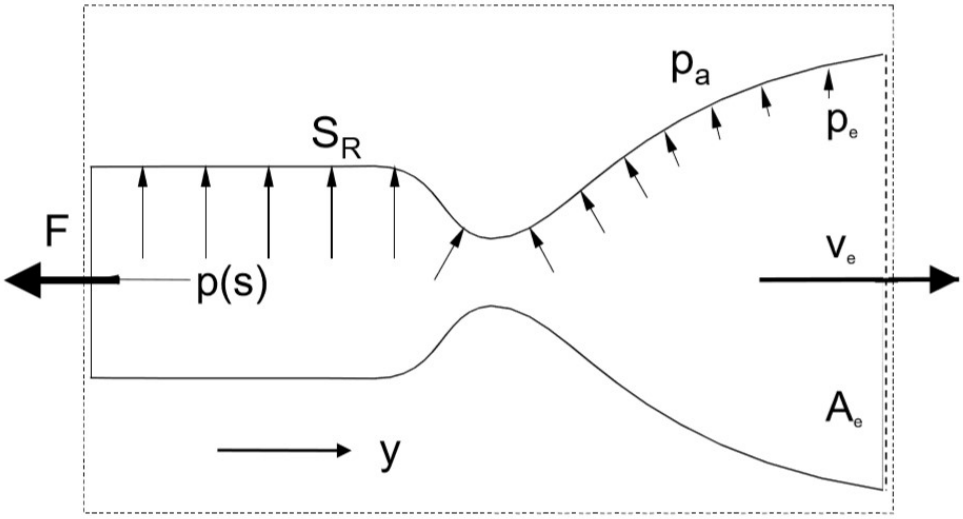

Figure 2.1 Schematic of a rocket engine

With ambient pressure p_a, the average values over the nozzle exit area for pressure p_e, the exit velocity v_e, a mass flow rate of exhausted gas $\dot{m}$ and the nozzle exit area A_e, the thrust F is calculated as:

$$F = \dot{m}v_e + (p_e - p_a)A_e = \dot{m}c_{eff} \tag{2.1}$$

The thrust is also a result of pressure exerted on the wall of the chamber. As the gas pressure outside cannot compensate for that on the bottom of the chamber, the difference between internal and external pressure generates the thrust. The effective exhaust velocity c_{eff} indicates the ideal condition of exit pressure equals the ambient pressure.

2.1.2 Definitions

The Tsiolkovsky-equation explains the relationship between the change of velocity Δv (the maximum change of velocity of the rocket without other external forces) and the combination of the effective exhaust velocity c_{eff}, the initial mass of the rocket m_0 and the final mass of the rocket m_B. This formulation was deduced by applying the conservation of momentum theorem. Imagine that a rocket has a mass m_R and velocity v_R with no force exerted on it. At a mass flow rate of $\dot{m}$, propellants are expelled from the rocket at velocity c_{eff}. Simultaneously, the rocket's mass is reduced by the exhausted mass. In addition, the velocity of the rocket increases by dv_R as shown in Fig. 2.2. For momentum:

$$\sum I \approx 0: m \cdot v_R = (m_R - \dot{m}dt) \cdot (v_R + dv_R) - \dot{m}dt \cdot c_{eff} \tag{2.2}$$

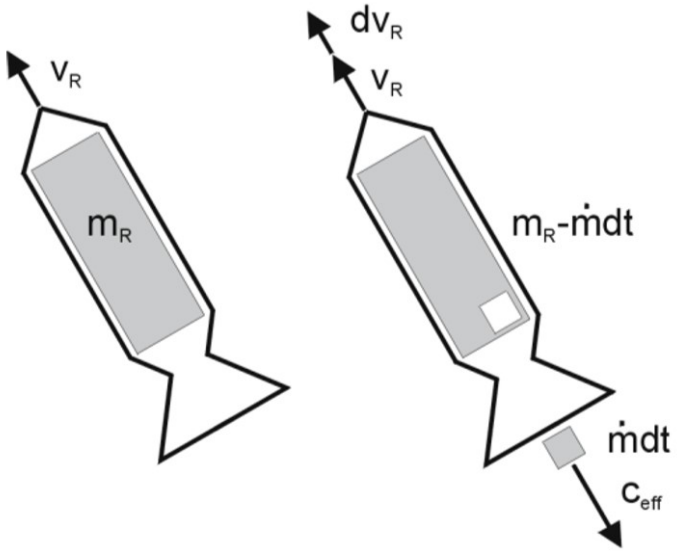

Figure 2.2 Schematic of application of the momentum theorem

Through integration of the regions both within the bounds of initial and final velocities and within the bounds of initial and final masses of the rocket, the change of velocity is calculated as:

$$\Delta v = c_{eff} \cdot ln(\frac{m_0}{m_B}) \tag{2.3}$$

Given that the structure and payload are inversely related in the final mass, significant reductions of the structure masses are preferred: for instance, reductions in the chamber size and weight, the mass of the tanks, pipes and valves. As higher amounts of the initial propellant raise the change velocity, this equation can be adopted to calculate how much propellant is needed to reach a new destination, for instance, Mars.
The specific impulse of a rocket, I_{sp}, represents the ratio of thrust F to the weight flow rate of propellants $\dot{W}$.

$$I_{sp}[s] = \frac{F}{\dot{W}} \tag{2.4}$$

The specific impulse denotes how effectively a rocket uses propellant. With higher specific impulses, the rocket engine burns the propellants more effectively in generating forward thrust, resulting in less propellant required for a given Δv, per the Tsiolkovsky-equation.
The characteristic velocity c^* is a measure of the energy available from the combustion process, which evaluates rocket performance. Typically, it is calculated by

$$c^* = \frac{p_c \cdot A_{th}}{\dot{m}} \tag{2.5}$$

where p_c represents total pressure in the throat, A_{th} is the throat area and $\dot{m}$ is the propellant mass flow rate. c^* is typically adopted to compare different propellants and propulsion systems. For instance, its values range from 1,333 m/s for monopropellant hydrazine to 2,360 m/s for cryogenic oxygen/hydrogen.

2.1.3 Thermodynamic Relations

Inside the chambers and nozzles, the fundamental thermodynamic relations can describe the complex physical and chemical processes. The following formulas illustrate a quasi-one-dimensional nozzle flow representing idealized and simplified equations of the complex multi-dimensional nozzle flows and the true aerothermochemical processes. Given the suppositions stated below, the equations obtain solutions for a variety of calculations of engine performance and determination of key design parameters for specific missions. In chemical rocket engines, the performance typically measures 1-6% below the calculated ideal value [6]. During conceptual design processes, optimizations of ideal rocket parameters, such as geometrical parameters for nozzles, with corrections have been commonly adopted. These suppositions are typically valid for an ideal rocket unit [6]:
1. The products of the chemical reactions are homogeneous.
2. All the species of the chemical reaction products are gaseous, and the mass of the working substance remains virtually unchanged by liquid or solid condensed phases.
3. These gaseous products conform to the perfect gas law.
4. No heat is transferred across the rocket walls, thus, the flow is adiabatic.
5. Friction is not a factor and no boundary layer effects exist.
6. The nozzle flow contains no shock waves or discontinuities.
7. The propellant flows steadily and at a constant rate. The working fluid's expansion is uniform, steady and with no vibration. Transient effects during start-up and shutdown have a short duration and are negligible.
8. The rocket's exhaust gases travel on an axially directed vector.
9. The gas velocity, pressure, temperature and density are uniform across any section vertical to the nozzle axis.
10. Within the rocket chamber, chemical equilibrium has been established and the gas composition in the nozzle remains unchanged.

The quasi-one-dimensional theory is derived from these assumptions. In a liquid bipropellant engine, this theory assumes an injection system that mixes the two propellants to create a homogeneous working substance. An efficient injector almost reaches this state. In solid rocket motors, the propellant must be perfectly mixed and uniform with a steady burn rate. The hot gases of nuclear, solar-heated or arc-heated rockets have an identical temperature at different cross sections and a steady state flow.
The temperatures of common propellants in the chamber are typically above 3,000 K, with all gases above their saturation conditions and following the perfect gas law. Under suppositions 4, 5, and 6, expansion in the nozzle obeys the isentropic flow relationships, thus delineating the maximum conversion of thermal energy to kinetic energy of the jet and indicating that the flow is a reversible process in thermodynamics. Friction losses at the walls are difficult to ascertain, but are typically negligible during the flow processes. Apart from remarkably small chambers, the heat loss through the rocket's walls typically comprises less than 1% of the total energy and is negligible. Typically, fluctuations of the propellants' mass flow rate and pressure are below 5% of the rated value, with minimal effect on engine performance.
The conservation of energy law can be adopted in the adiabatic flow without shaft work done inside the nozzle [6]. In the absence of shocks or friction, the flow entropy is constant. The theory of enthalpy, which encompasses the internal thermal energy and the flow work, can be employed to analyze flow systems. Under the assumptions of ideal gases, the enthalpy is a function of the specific heat c_p and temperature *T*, shown as a product of them. The total (stagnation) enthalpy per unit mass h_0 is given as:

$$h_0 = h + \frac{v^2}{2J} = constant \tag{2.6}$$

Here, with SI units (kg, m, sec), the mechanical equivalent of heat *J* is one. Applying the conservation of energy principle to the flow through any two sections *x* and *y* indicates that a fall in enthalpy corresponds to a rise in kinetic energy because any variations in potential energy are minimal.

$$h_x - h_y = \frac{{v_y}^2 - {v_x}^2}{2J} = c_p(T_x - T_y) \tag{2.7}$$

The mass conservation can be shown by equating the mass flow rate $\dot{m}$ between any sections *x* and *y*. In expressions of cross-sectional area *A*, velocity *v*, and specific volume *V*:

$$\dot{m}_x = \dot{m}_y \equiv \frac{Av}{V} \tag{2.8}$$

The perfect gas law is expressed as:

$$p_x V_x = RT_x \tag{2.9}$$

whereby the ratio of the universal gas constant R′ to the molecular mass of the gas equals the gas constant R. At standard conditions, the molecular volume becomes 22.41

m^3/kg−mol, corresponding to a value of R′ = 8,314.3 J/(kmol·K). The specific heat at constant pressure c_p, the specific heat at constant volume c_v, and their ratio k are constant for perfect gases over a wide range of temperatures and are connected as:

$$k = \frac{c_p}{c_v} \tag{2.10}$$

$$c_p - c_v = \frac{R}{J} \tag{2.11}$$

$$c_p = \frac{kR}{(k-1)J} \tag{2.12}$$

During isentropic flow processes, the relations apply between any points *x* and *y*:

$$\frac{T_x}{T_y} = \left(\frac{p_x}{p_y}\right)^{\frac{k-1}{k}} = \left(\frac{V_y}{V_x}\right)^{k-1} \tag{2.13}$$

The pressure falls significantly in an isentropic expansion inside the nozzle, while the absolute temperature declines less and the specific volume rises. If a flow is brought into fully motionless conditions in isentropic processes without other forces, these theoretical conditions are denoted as stagnation conditions and specified by the subscript 0. Equation 2.6 indicates that the stagnation enthalpy comprises the sum of the static enthalpy plus the fluid kinetic energy. The stagnation temperature T_0 is calculated as:

$$T_0 = T + \frac{v^2}{2c_pJ} \tag{2.14}$$

whereby T is the absolute fluid static temperature. The stagnation temperature is constant throughout an adiabatic flow. The stagnation pressure's relationship to the local pressure in the flow calculated from Eq. 2.13 and 2.14 are shown as:

$$\frac{p_0}{p} = \left[1 + \frac{v^2}{2c_pJT}\right]^{\frac{k}{k-1}} = \left(\frac{V}{V_0}\right)^k \tag{2.15}$$

When the local velocity of the gas approaches zero and most of the kinetic energy are converted to internal energy, the local temperature and pressure will reach the stagnation temperature and pressure. Within a rocket chamber, the gas Mach number is low, thus the local pressure equals the stagnation pressure. As the pressure and density contribute to sound velocity equally, whose effects cancel out, the velocity of sound a only depends on the temperature. It can be expressed as

$$a = \sqrt{kRT} \tag{2.16}$$

As the Mach number M_a represents the ratio of the local flow velocity v to the local velocity of sound a, this number is dimensionless:

$$M_a = \frac{v}{a} = \frac{v}{\sqrt{kRT}} \tag{2.17}$$

Subsonic conditions occur when the Mach number is less than one, while supersonic conditions occur for numbers greater than one. With the known Mach number, the

stagnation temperature can be derived from Eqs. 2.7, 2.12 and 2.15:

$$T_0 = T[1 + \frac{(k-1){M_a}^2}{2}] \tag{2.18}$$

or vice versa

$$M_a = \sqrt{\frac{2}{k-1}(\frac{T_0}{T} - 1)} \tag{2.19}$$

T_0 and p_0 identify the stagnation values of temperature and pressure. For isentropic processes, the stagnation pressure stays unchanged during an adiabatic expansion, expressed as:

$$p_0 = p\,[1 + \frac{(k-1){M_a}^2}{2}]^{\frac{k}{k-1}} \tag{2.20}$$

For given points x and y within the nozzle, the expansion area ratio for isentropic processes can be indicated as Mach numbers:

$$\frac{A_y}{A_x} = \frac{M_x}{M_y}\sqrt{\left\{\frac{1+[(k-1)/2]{M_y}^2}{1+[(k-1)/2]{M_x}^2}\right\}^{\frac{k+1}{k-1}}} \tag{2.21}$$

2. 2 Liquid Rocket Propellants

Rocket engines may use solid propellants, liquid propellants and a combination of them, hybrid propellants. In liquid rocket engines, the heat is typically obtained from the chemical reactions of the liquid propellants. Vehicles driven by liquid rocket engines carry both fuel and oxidizer. A rocket engine's propellant comprises the totality of substances in the chemical reaction that releases heat. Bipropellants (Fig. 2.3) consist of two separately stored fluids: an oxidizer such as liquid oxygen, nitric acid or liquid fluorine, and a fuel such as hydrogen, kerosene, alcohol or methane. Heat can be obtained not only from the chemical reactions of combustion, but also from other chemical reactions such as the decomposition of certain chemical compounds. Upon igniting a single-component propellant called a monopropellant, the decomposition reaction releases heat in the liquid propellant rocket engine. Another type of monopropellant comprises mixtures of fuel and oxidizer, which normally do not self-ignite and can be stored in a single container.

Additives are introduced into the propellant components either as catalysts to raise the combustion rate and efficiency in the reaction flow, or as inhibitors to reduce or stop the reaction. Hypergolic propellants ignite spontaneously when their components combine, whereas anergolic propellants do not burn spontaneously when their components come into contact with each other [7].

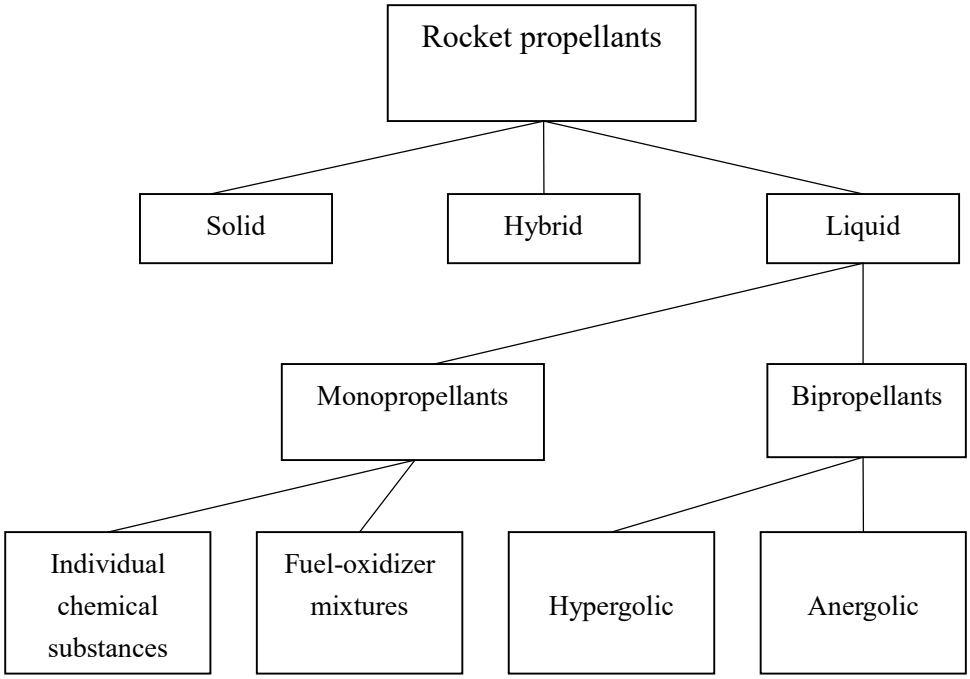

Figure 2.3 Classification of liquid rocket propellants [7]

The choice of a propellant for a liquid propellant rocket engine is based on the purpose of the engine and rocket as well as the state of current rocket technology. Currently, three propellant combinations are mostly utilized in high performance liquid propellant rocket engines. These are liquid oxygen/liquid hydrogen (LOX/LH_2), unsymmetrical dimethyl-hydrazine/nitrogen-tetroxide (UDMH/NTO), and LOX/kerosene. The advantage of LOX/LH_2 is the highest specific impulse among the three, while LH_2's low density and extremely low boiling point require bigger tanks and have limited storage times. The hypergolic and storable nature are the most attractive characteristics of UDMH/NTO, but its toxicity-related handling problems and pollution issues together with its rather poor performance make this propellant combination less and less acceptable, especially in modern societies. Therefore, as a compromise, LOX/kerosene has been used in rocket propulsion for decades because of its relatively low cost, low pollution and high performance. Many famous LOX/kerosene rocket engines, such F-1, NK-33, RD-180, were designed, manufactured and applied successfully in the United States and former Soviet Union. Even today, Falcon 9, ATLAS 5, Zenit 2/3 and Soyuz rockets are flying with LOX/kerosene rocket engines.

Although kerosene has some disadvantages in comparison with methane, it is still an important fuel in current propulsion systems. Firstly, the coking temperature of kerosene on the hot gas-side of the liner walls is the main limitation for its use in the regenerative cooling system which prevails in large thrust liquid rocket engines. Hence, almost all high pressure kerosene/oxygen engines apply some sort of film cooling in order to manage the high heat loads and stay within the coking limits. For pure methane instead,

the coking temperature is 970 K and thus much higher than that of kerosene (590 K). Secondly, methane provides not only a better specific impulse, but an improved heat transfer performance because of its high thermal conductivity, specific heat and low viscosity. In summary, from a system point of view, methane could, despite its lower density which yields larger propellant tanks, be a promising fuel as a propellant for a reusable rocket engine, which has been a concern for rocket engineers. Some research about this propellant combination of oxygen/methane has been conducted in some projects in the United States [8,9], Europe [10,11,12], Japan [13] and China [14,15]. However, until now no oxygen/methane rocket engine has flown. Unresolved issues still remain between the fundamental research and technology development, and a final practical application.

2.3 Thrust Chamber

In the thrust chamber, thrust is generated by the efficient conversion of the propellant's chemical energy into hot gas kinetic energy. To achieve that conversion, the propellants first react in the combustion chamber and are then accelerated through a convergent/divergent nozzle to attain high gas velocities and thrust. The thrust chamber consists of three basic parts: injector, combustion chamber and nozzle (Fig. 2.4).

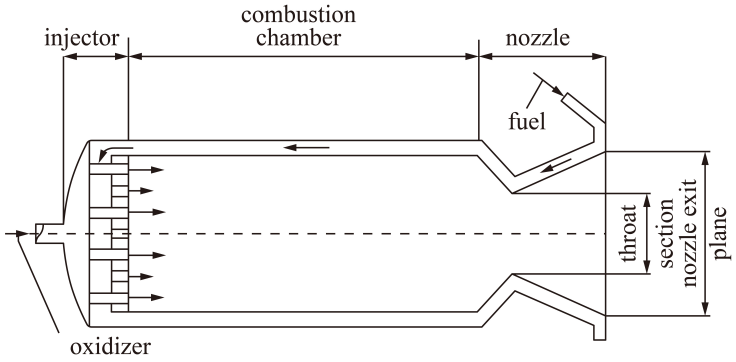

Figure 2.4 Diagram of thrust chamber

As part of the thrust chamber, the engine injector contains holes through which it feeds propellant components at the proper oxidizer/fuel ratio into the combustion chamber in a manner to promote propellant mixing, spraying, and droplet atomization. The number and design of sprayers determine the characteristics of the spraying and mixing of components. Many designs exist and are grouped into four classes: impinging injection, swirl injection, parallel injection in form of a showerhead, and shear coax injection. When both propellants enter the injector in liquid states, an impinging injector is typically employed whose operating principle is: when the jets impinge on each another, they form a liquid sheet; the sheet then decomposes, atomizes and reacts simultaneously in case of hypergolic propellants, while if it interacts with another liquid sheet, they then atomize and react. Swirl injectors are typically adopted in small thrusters, giving a

tangential velocity component to both propellants often in types of coax injectors. Because of small recirculation zones near the face plate, the injectors often mix the propellants effectively and achieve high combustion performance in addition to allowing for the formation of a cooling film. Shear coax injectors are typically used when one propellant is liquid. At the introduction of liquid oxygen, the area constriction guarantees a homogenous mass flow rate for every element. The restriction and the expansion afterwards precipitate large-scale turbulences in the liquid that support the atomization.

In the injector head, the oxidizer and fuel manifolds are arranged in a particular order: staggered, honey-combed, or concentric (Fig. 2.5).

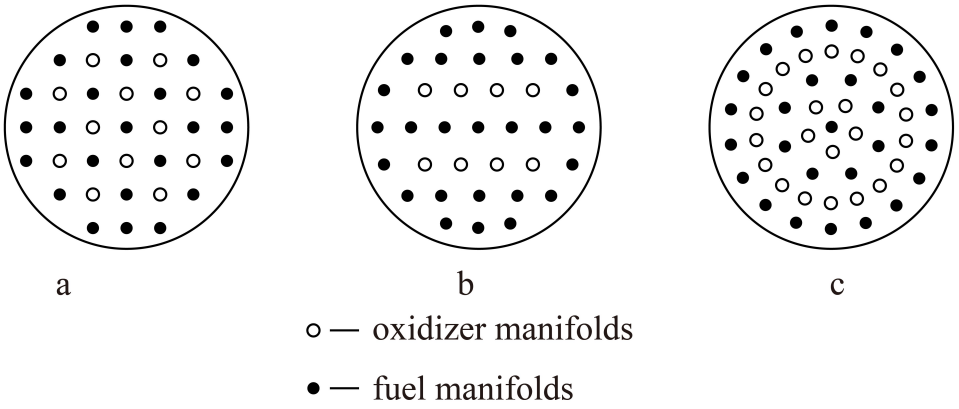

Figure 2.5 Arrangement of manifolds in injector,
a: staggered; b: honey-combed; c:concentric

The injector/wall interaction is an essential concern in the design and development of the injector plates. To avoid the attacks of the mixture of oxidizer-rich gases and cryogenic droplets on the chamber walls in the vicinity of the face plate, several fuel injection holes are provided along the injector's outermost row with a smaller mixture ratio. With adjustment of the mixture ratios, which is typically adopted in the gas generators, the temperature of the hot gas near the walls can be limited to protect the surfaces from the attacks by the hot gas and droplets. An alternative method to protect these components and achieve high life cycles is the injection of a coolant film, whose performance is influenced by a series of flow and geometric parameters. On the workbench at LTF, film cooling has been employed to protect the glass windows in the research of flame anchoring.

The fuel is mixed, heated, oxidized, and accelerated within the combustion chamber, and it is one of the most important components of the thrust chamber. Typically the injection, atomization, reaction and acceleration processes are at the millisecond order, and the combustion chamber must be specifically designed to meet the requirements of the thrust engine. The chamber's design and size must be such that the propellant can react completely, i.e., that the conversion of chemical energy to heat energy be as high as possible. The choices of the chamber shape and size are the main points in the preliminary design, and these parameters have a significant influence on the chamber's

performance, stability and reliability. Currently, the first preliminary step is still dependent on the existing design experience. To satisfy the technical and performance requirements of the launching concept, modifications and improvements will be made on the existing tried-and-true prototype with applications of statistical data to determine the shape and size. The reference of the prototype shortens the design and development period, even though in this method it is difficult to break the limits of existing prototype and the design quality is mainly based on the designers' practical experience.

As the series of physical and chemical processes of injection, atomization, evaporation, mixing and combustion are closely coupled and have complex interactions on each other, it is pretty difficult to determine which process has the most important influence. The chamber volume should make the propellant stay in the combustion chamber sufficiently long to provide complete mixture and combustion, and this residence time is a function of several parameters. The burn rate is determined by the mixture ratio, the phase state of the propellants, the chamber parameters (contraction ratio, Mach number, turbulence intensity) and the injector heads. The burn rate of the liquid propellants is also limited by the evaporation rate, mixture time and chemical reaction rates. The large chambers typically adopt large injectors and correspondingly the droplets are larger, resulting in longer time required for complete combustion. Thus the chamber volume has effects on the combustion efficiency. Theoretically, the chamber volume is a function of the propellant mass flow rate, the mean density of the products and time for chemistry reactions.

The residence time of propellants in the chamber t_r can be denoted as:

$$t_r = \tau_{ign} + t_{rg} \tag{2.22}$$

where τ_{ign} represents ignition delay, of which further details can be found in Chapter 4.8. t_{rg} is the time from chemistry reactions start to complete, approximately given as:

$$t_{rg} = \frac{\rho_c^*}{p_c} c^* L^* \tag{2.23}$$

Here ρ_c^* is the hot gas density of the inlet of the converging part of the nozzle. c^* is the characteristic velocity, given in Eq. 2.5. The L^* is characteristic length, namely the ratio of combustion chamber volume V_{ch} to the area of throat cross-section A_{th}:

$$L^* = \frac{V_{ch}}{A_{th}} \tag{2.24}$$

For the hot gas of liquid propellants, k can be given as a constant 1.2, and under this assumption, t_{rg} can be further approximated as:

$$t_{rg} = 2.38 \frac{L^*}{c^*} \tag{2.25}$$

Equation 2.25 indicates that t_{rg} is influenced by the propellant properties and the injectors. In a rocket engine, where $L^* = 2\text{m}$ and $c^* = 1500 m/s$ $t_{rg} = 3.17\, ms$. According to the experimental data with glass windows, in most cases for different

injectors, $1ms < t_{rg} < 8ms$. For instance, in the RD-120 LO_x/kerosene engine t_{rg} is 1.8 ms, and in RD-107 LO_x/kerosene it is 5.59 ms.

The completeness of combustion in the chamber is measured by c^*. The greater the c^*, the more complete propellant combustion. The c^* can be attained experimentally and by computation. Theoretical computation of c^* assumes that the transformation of reactants into products is complete. Comparison between the theoretical characteristic velocity and that determined experimentally indicates the chamber coefficient shows the portion of propellant injected into the combustion chamber that participates in the combustion reactions. Due to the incomplete combustion and inhomogeneities of spray, component distributions along the chamber cross sections, and mass flow densities and other factors, in practical situations the heat released is smaller than that in theory, resulting in the derivation of parameters of the combustion products (stagnation temperature and pressure, chemical components) from the theory values. An ideal rocket unit is under the assumptions in Chapter 2.1.3. The differentiation between theory and experiment makes the most important parameter of the thrust engine, I_{sp}, decline, as defined in Eq. 2.4. In addition, the chamber coefficient is given as:

$$\varphi_{ch} = \frac{c^*_{exp}}{c^*} \tag{2.26}$$

Here, as denoted in Eq. 2.5, c^*_{exp} represents the characteristic velocity in the experiments and c^* denotes the theory characteristic velocity. The combustion chambers of modern liquid propellant rocket engines have values of φ_{ch} from 0.96 to 0.99, which is determined by the mixture ratio and the chamber length; thus, virtually all of the chemical energy of the propellant in the combustion chamber is converted into heat energy.

At the end of the combustion chamber, the nozzle comprises of converging and diverging parts. The essential function of the nozzle is to convert the heat energy of the high temperature combustion productions to the dynamic energy, and accelerate the jets, resulting in a forward thrust moving the rocket obtained as a reaction to the rearward accelerated gases. Definitely, different type nozzles exert different reactions on the gas flows, and the task is to design the optimized parameters of the dimensions for reactive forces to the gases' acceleration. During the development history of the liquid rocket engines, research is investigated on two aspects, in addition to the improvement of the nozzle efficiency: 1) in the contexts of assurance of high nozzle efficiencies, the length of the nozzle should be shortened and the weight minimized; 2) the nozzle work efficiently at all altitudes. According to the gas dynamics, the flow fields inside the divergent part have close connections with the ambient pressure at the exit of the nozzle. During the launch process from the ground to the orbits, at the nozzle exit the ambient pressure changes with the height, and correspondingly the nozzle must be designed with high nozzle coefficients at all altitudes, and as a result bell shape nozzles with a parabolic contour are typically adopted. This contour is ideal and truncated, which is

employed in all Russian engines, or thrust optimized that is assembled in American, European and Japanese engines. Compared with that of the ideal one, optimized nozzle's cross-sectional area expands faster near throat, and correspondingly has a shorter length, even though this faster expansion may introduce internal shocks and restricted shock separation during the start-up and shutdown processes at certain stages.
During the acceleration process of the hot gases, several factors have influences on the nozzle coefficient, such as the energy loss due to the expansion from sonic velocities to supersonic velocities, frictional loss because of viscosity of the gases, heat loss through the nozzle walls, and kinetic energy loss of the velocity in the radial direction.
The energy loss in the converging region and throat is minor, and the main loss in the diverging part may come from two aspects: 1) near the throat, the gases in the center and near the walls are not accelerated to supersonic at the same time, resulting in potential shock wave in this region; 2) during acceleration process, pressure difference between the boundary layer and the center gas may be introduced because of the nozzle's contour, and correspondingly shock wave is formed. The influence of the energy loss in the divergent part on the nozzle coefficient can be denoted as φ_{N1}. Because of gas viscosity, the frictional loss in the boundary layer is unavoidable, and its effect on the nozzle coefficient is defined as φ_{N2}. At the exit of the nozzle, the velocity of the exhausted gas in the axial direction does not contribute to the thrust, and this loss's reaction on the nozzle coefficient is given as φ_{N3}. In addition, the heat loss through the nozzle walls is represented by φ_{N4}….
Thus the nozzle coefficient can be calculated as:

$$\varphi_N = \varphi_{N1} \cdot \varphi_{N2} \cdot \varphi_{N3} \cdot \varphi_{N4} \ldots. \tag{2.27}$$

As a result, the relationship between experimental specific impulse and the theory specific impulse can be given as

$$\frac{I_{exp}}{I_{theo}} = \varphi_{ch} \cdot \varphi_N \tag{2.28}$$

Equation 2.28 indicates how the injection, atomization, evaporation, mixing, combustion, contraction ratio, Mach number, turbulence intensity in the chamber and the expansion process, frictional loss, the velocity in the axial direction, the heat loss through the walls in the nozzle influence the most important parameter of the thrust chamber, I_{sp}.

3. Modeling of Turbulent Reacting Flows

3.1 Models Introduction

Rocket combustion flow fields comprise fluid-dynamics combined with all of the following: combustion, turbulence, radiation, spray atomization, vaporization and liquid fuel films. Numerical simulation techniques hold the promise of providing greater understanding about combustion in rocket engines. Despite the considerable progress achieved in experimental measurement methods, computational fluid dynamics can still offer detailed insights regarding situations in which experimental measurements have been heretofore impossible [16,17,18,19,20,21].

During the past few decades, improvements have been seen in computational fluid dynamic simulations for turbulent combustion modeling. Several solution methods for turbulent flow fields are discussed as following.

Among solution methods, direct numerical simulation (DNS) is set atop of the hierarchy. By implementing the DNS of turbulent combustion, one can comprehend the details of interaction between turbulence and combustion. However, this method is made much more difficult when the flow is accompanied with combustion than when it has none because the combustion will bring a large change in the flow's temperature by multiples of the initial measurement. As a result, it is difficult to define the turbulence scale, which will determine the grid scale. Furthermore, combustion itself may introduce some scales (such as flame thickness and reaction time) in space and time that are comparable to turbulent scales. Hence, in the DNS of turbulent combustion, in addition to limitations from a simple geometry and a low Reynolds number (Re), there is a limitation from a low Damkohler number. The direct numerical simulation of turbulent combustion has provided a method to understand the process of flame surface straining and wrinkling, counter gradient transport phenomena for passive scalar and the structure of premixed flames, as well as made great progress in these aspects [22,23,24,25]. However, because the DNS needs a large amount of computing resources, it can be used only within a small geometry and under a low Reynolds number. It cannot be used in engineering applications. Hence, such DNSs are unaffordable in real situations with large Reynolds numbers as usually occur in practice.

Large Eddy Simulation (LES) was first proposed by American meteorologist Smagorinsky of the National Center for Atmospheric Research in the 1960s. In commemoration of his pioneering work, his sub-grid scale (SGS) model was named after him. In this model, a portion of the turbulent fluctuation is directly simulated; the Navier-Stokes equation is averaged (or filtered) in a small spatial domain to remove small-scale vortices from the flow field; and then the equations needed by large vortices are derived. The influence of the small vortices on the large vortices appears in the equations of the large vortices, while the influence of the small vortices is simulated with a model such as SGS. The large eddy structures of turbulence are strongly dependent on the boundary geometries and boundary conditions of the flow field;

therefore, it is difficult to implement a general turbulence model to describe the large eddy structures with different boundary characteristics. On the contrary, small scale vortices have no direct dependence on boundary conditions and are usually isotropic. Therefore, the SGS model has greater applicability than the RANS model. Since 1970, when Deardorff first conducted LES simulation to examine its industrial utility, the LES method has become one of the most widely employed and powerful tools for simulating turbulence flows, and its application fields are gradually expanding. The high fidelity of LES allows the simulation to capture the large scale dynamic motion [26,27,28,29,30].

As a result, in the simulation of transient combustion, such as ignition and extinction processes, LES can provide precise statistical information of turbulent fluctuation in the investigation of the influence from turbulence because it demonstrates the minor turbulence and interaction between the combustion and turbulence.

However, LES selects a filter width between the large and small vortex scales (Kolmogorov scale) of turbulence to filter the Navier-Stokes equations and divides all flow variables into large and small scales while directly computing the large turbulent motions and, with the SGS model, modeling the small scale effects. In this way, whether LES predicts turbulent combustion precisely depends on the scale of the combustion. Many incidents of combustion contain vortexes equal or smaller than those found in the Kolmogorov scale, and they are filtered by LES and need to be simulated with models. Therefore, the SGS model directly influences the accuracy and effectiveness of the LES of turbulent combustion. In addition, the LES needs much less computing resources than the DNS, but it still requires a large number of grid points; modeling the fine-scale motions also requires a large amount of computing time. As a result, LES is still unaffordable for complicated engineering turbulent cases. Hence, instead of being implemented in engineering applications, it is typically used to validate macro models [31,32,33].

LES models are under fast development [34,35]. New models have been proposed and validated with improvement over results obtained with classical subgrid scale models such as the Smagorinsky model [36]. In addition, a new method of coupling between subgrid-scale modeling and the truncation error of numerical discretization is also developed [37]. Furthermore, promising novel mesh generation methods with a global optimization strategy are emerging [38].

Spalart proposed a model, that contains both merits of RANS and LES by offering RANS in the boundary layers and LES after massive separation within a single formulation [39]. To describe the transition process, the attached eddies internal to the boundary layer near the wall are modeled by turbulence models in the RANS method, while the detached ones in the regions far from the thin shear flows are resolved. Its principal weakness is its response to ambiguous grids, in which the wall-parallel grid spacing is of the order of the boundary-layer thickness. In some situations, DES on a specified grid is then less precise than RANS on the identical grid or DES on a coarser grid [40,41,42].

To model the turbulent flow, Reynolds-Averaged Navier-Stokes is still the most commonly used method in engineering applications [43]. In this method, the momentary value is decomposed into mean and fluctuating values so as to take a time-average of

N-S governing equations. Because the velocity fluctuations still appear in the RANS equations, in the nonlinear term from the convective acceleration known as the Reynolds stress, the Navier–Stokes equations have nonlinearity. To close the RANS equations, various models have been introduced to compute the Reynolds stress. These models can be classified into two categories: first-order closure models (eddy-viscosity models) and second-order closure models. The eddy viscosity hypothesis was firstly proposed by Boussinesq in 1877. Because of the great efficiency and high precision of the first-order closure models, they are the most commonly used approaches to compute the turbulent flows in practical computations. They can be divided further into zero-equation models, half-equation models, one-equation models and two-equation models [44, 45, 46]. By solving two separate transport equations, two-equation turbulence models allow the ascertainment of both turbulent length and time scale. Typical examples of the two-equation models are the k-epsilon and the k-omega models, which can provide high-precision calculations of mean velocity. They are among the most widely used models to study turbulent flows. However, all the turbulence models temporally and spatially ignore the effects of turbulence fluctuations and small vortices, thus resulting in imprecise predictions of the mixture of propellants, with a variance of 30%-40%. The key problem of RANS is the modeling of interactions between the turbulence and chemical reactions. At first, combustion releases heat, and the density in the combustion chamber has high gradients, thus making the turbulence more complex. Additionally, combustion raises the temperature, and increases are seen in momentum, density, energy exchange rate, and the transport coefficients of the flow.

A modeled transport equation for the kinematic eddy (turbulent) viscosity is solved by employing the one-equation Spalart-Allmaras model [47]. Designed specifically for aerospace applications involving wall-bounded flows, this model has shown its ability to provide precise results for boundary layers under adverse pressure gradients. It evolved for use with aerodynamic flows, and is increasingly used in turbomachinery applications. It lacks validation for general industrial flows, and predicts with larger errors some free shear flows, in particular plane and round jet flows. Moreover, its predictions of the decay of homogeneous, isotropic turbulence are unreliable.

Among turbulence models employed in engineering simulations, two-equation models have been the most relied upon in solving two transport equations and modeling the Reynolds Stresses with the Eddy Viscosity approach. Within this class of models, the standard $k-\varepsilon$ model has become the workhorse of practical engineering flow calculations since it was first proposed by Launder and Spalding [48]. It has prevailed in industrial flow and heat transfer simulations due to its robustness, economy, and good precision in a wide range of turbulent flows [43, 49]. The standard $k-\varepsilon$ model is based on model transport equations for the turbulence kinetic energy (k) and its dissipation rate (ε). The model transport equation for ε was derived by employing physical reasoning and consequently bears scant resemblance to its mathematically exact counterpart; in contrast, the model transport equation for k is developed from the precise equation.

The Wilcox $k-\omega$ model forms the basis for the standard $k-\omega$ model [50], which encompasses modifications for low-Reynolds number effects, compressibility, and shear

flow spreading. One disadvantage of the standard $k-\omega$ equation is its relatively strong sensitivity of a solution dependent upon the freestream values of and outside the shear layer.

Some models, such as the Spalart-Allmaras model, exhibit the disadvantage of insensitivity to adverse pressure gradients and boundary layer separation. In many simulations, they will predict a delayed and reduced separation relative to observations, resulting in erroneously optimistic design evaluations for flows that separate from smooth surfaces. Compared with those models, the $k-\omega$ model offers several advantages. Most prominent among them is its integration without the need for additional terms through the viscous sublayer, thus allowing for a relatively straight forward formulation of a robust-insensitive treatment. Furthermore, $k-\omega$ models are often superior predictors of adverse pressure gradient boundary layer flows and separation. Among other $k-\omega$ models, the SST versions were designed to compensate for the standard model's freestream sensitivity. Moreover, the SST model accurately computes flow separation from smooth surfaces.

Given the increased power of modern computers, more frequent use is made of CFD codes to perform detailed assessments of the flow behaviour in rocket engines. The goal is to understand observed variations in fluid properties and to find the source of any unexpected behaviours. However, such CFD methods require extensive computational times, thus rendering speedy parametric analyses impossible. Additionally, most require long input preparation times. Although the qualities of a thorough and full-depth analysis may be desirable in the study of specific single components and scenarios, for complex, multi-component systems, the long computational times become insurmountable.

The main problem in turbulent combustion modeling has been how to determine an average reaction rate in fluctuating turbulent flow. This problem is commonly referred to as the turbulence combustion closure problem, and development and improvement of the turbulent combustion model have been implemented to achieve turbulence combustion closure based on physics with greater precision [51,52,53].

3.2Governing Equations

The simulations are performed by applying ANSYS Fluent in a finite volume based method. Many research institutes have made great effort to perform reliable numerical simulations of gas-gas combustion flows and their research has indicated that the steady Reynolds averaged Navier-Stokes (RANS) method combined with appropriate chemical kinetic and turbulence modelling is an effective way to model such combustion chamber flows and predict heat fluxes which are in close agreement with experimental results [54,55,56,57,58].

a. Conservation equations of mass, momentum, and energy and the turbulence model are shown as [49]

$$\frac{\partial \rho}{\partial t} + \nabla \cdot (\rho \vec{v}) = 0 \tag{3.1}$$

$$\frac{\partial (\rho \vec{v})}{\partial t} + \nabla \cdot (\rho \vec{v} \vec{v}) = -\nabla p + \nabla \cdot (\bar{\bar{\tau}}) + \vec{F} \tag{3.2}$$

$$\frac{\partial}{\partial t}(\rho E) + \nabla \cdot [\vec{v}(\rho E + p)] = \nabla \cdot \left(k_{eff} \nabla T - \sum_j h_j \vec{J}_j\right) + S_h \tag{3.3}$$

ρ, $\vec{v}$ and $\vec{F}$ are the density, velocity and external body forces. $\bar{\bar{\tau}}$ is the stress tensor:

$$\bar{\bar{\tau}} = \mu \left[(\nabla \vec{v} + \nabla \vec{v}^T) - \frac{2}{3} \nabla \cdot \vec{v} I \right] \tag{3.4}$$

where μ is the molecular viscosity and I is the unit tensor.

In Equation 3.3,

$$E = h - \frac{p}{\rho} + \frac{v^2}{2} \tag{3.5}$$

here the sensible enthalpy *h* is defined as:

$$h = \sum_j Y_j h_j \tag{3.6}$$

where Y_j is the mass fraction of species j and

$$h_j = \int_{T_{ref}}^{T} c_{p,j}\, dT \tag{3.7}$$

where T_{ref} represents the reference temperature, 298.15 K and $c_{p,j}$ represents the heat capacity of species j. k_{eff} is the effective thermal conductivity:

$$k_{eff} = k + \frac{C_p \mu_t}{Pr_t} \tag{3.8}$$

k is the thermal conductivity, with Pr_t being the turbulent Prandtl number. In this study Pr_t is taken to be 0.85 for EDC, and 0.9 for flamelet. Here μ_t is the eddy viscosity. In Eq. 3.3, S_h denotes the source of energy due to chemical reaction [49]. $\vec{J}_i$ is the diffusion flux of species i, calculated by:

$$\vec{J}_i = -\left(\rho D_{i,m} + \frac{\mu_t}{Sc_t}\right) \nabla Y_i - D_{T,i} \frac{\nabla T}{T} \tag{3.9}$$

where $D_{i,m}$ denotes the mass diffusion coefficient for species i, and $D_{T,i}$ represents the thermal diffusion coefficient. Here Sc_t is the turbulent Schmidt number, given as 0.7. This value is recommended for high-Reynolds-number jet flows by Yimer [59].
Turbulence closure k-ε models are:

$$\frac{\partial}{\partial t}(\rho k) + \frac{\partial}{\partial x_i}(\rho k u_i) = \frac{\partial}{\partial x_j}\left[\left(\mu + \frac{\mu_t}{\sigma_k}\right)\frac{\partial k}{\partial x_j}\right] + G_k - \rho\varepsilon - Y_M \qquad (3.10)$$

$$\frac{\partial}{\partial t}(\rho\varepsilon) + \frac{\partial}{\partial x_i}(\rho\varepsilon u_i) = \frac{\partial}{\partial x_j}\left[\left(\mu + \frac{\mu_t}{\sigma_\varepsilon}\right)\frac{\partial \varepsilon}{\partial x_j}\right] + C_{1\varepsilon}\frac{\varepsilon}{k}G_k - C_{2\varepsilon}\rho\frac{\varepsilon^2}{k} \qquad (3.11)$$

The turbulent energy production tensor due to the mean velocity gradients, is given by:

$$G_k = -\rho\overline{u_i{}'u_j{}'}\frac{\partial u_j}{\partial x_j} \qquad (3.12)$$

Here, Y_M represents the dilatation dissipation, given as:

$$Y_M = 2\rho\varepsilon M_t{}^2 \qquad (3.13)$$

where M_t is the turbulent Mach number, calculated by:

$$M_t = \sqrt{\frac{k}{a^2}} \qquad (3.14)$$

where a is the velocity of sound, defined in Equation 2.16. μ_t is modeled by combining k and ε as:

$$\mu_t = \rho C_\mu \frac{k^2}{\varepsilon} \qquad (3.15)$$

$C_{1\varepsilon}$, $C_{2\varepsilon}$, C_μ, σ_k and σ_ε are constants, separately being 1.44, 1.92, 0.09, 1.0 and 1.3.

Species transport equations for EDC are:

$$\frac{\partial}{\partial t}(\rho Y_i) + \nabla\cdot(\rho\vec{v}Y_i) = -\nabla\cdot\vec{J}_i + R_i \qquad (3.16)$$

Here R_i represents the net rate of production of species i within chemical reactions.
Species transport equations for flamelet are:

$$\frac{\partial}{\partial t}\left(\rho\overline{f'^2}\right) + \nabla\cdot\left(\rho\vec{v}\overline{f'^2}\right) = \nabla\cdot\left(\frac{\mu_l+\mu_t}{\sigma_t}\nabla\overline{f'^2}\right) + C_g\mu_t\cdot\left(\nabla\bar{f}\right)^2 - C_d\rho\frac{\varepsilon}{k}\overline{f'^2} \qquad (3.17)$$

Here f represents the mixture fraction and f'=f-$\bar{f}$. The constants σ_t, C_g, and C_d are 0.85, 2.86 and 2.0.
The coupled algorithm is selected for the coupling between the pressure and velocity fields, along with a second order scheme for pressure and a second order upwind for all quantities. The ideal gas equation of state is adopted. The interaction between turbulence and chemistry is described by the EDC and flamelet separately.
The EDC model is:

$$\xi^* = C_\xi\left(\frac{\nu\varepsilon}{k^2}\right)^{1/4} \qquad (3.18)$$

Here * represents fine-scale quantities, and ν is kinematic viscosity. The volume fraction constant,C_ξ, is taken to be 2.1377. In addition, the volume fraction of the fine scales is given as ξ^{*3}. In the fine structures, species are considered to react over a time scale:

$$\tau^* = C_\tau \left(\frac{\nu}{\varepsilon}\right)^{1/2} \tag{3.19}$$

Here C_τ is the time scale constant, taken to be 0.48.
For flamelet simulation, combustion is simulated via the non-adiabatic flamelet approach. For calculation of the species mass fractions and temperature, the mixture fraction, the mixture fraction variance and the scalar dissipation rate are used. A β-PDF is implemented to obtain the interaction between the turbulence and combustion. χ, S_i and H_i denote the scalar dissipation, the reaction rate and specific enthalpy of species i separately.

$$\rho \frac{\partial Y_i}{\partial t} = \frac{1}{2}\rho\chi \frac{\partial^2 Y_i}{\partial f^2} + S_i \tag{3.20}$$

$$\rho \frac{\partial T}{\partial t} = \frac{1}{2}\rho\chi \frac{\partial^2 T}{\partial f^2} - \frac{1}{c_p}\sum_i H_i S_i + \frac{1}{2c_p}\rho\chi \left[\frac{\partial c_p}{\partial f} + \sum_i c_{p,i}\frac{\partial Y_i}{\partial f}\right]\frac{\partial T}{\partial f} \tag{3.21}$$

ϕ represents species mass fractions and temperature.

$$\overline{\phi} = \int\int \phi(f,\chi_{st}) p(f,\chi_{st}) df d\chi_{st} \tag{3.22}$$

Thermodynamic and transport properties are based on curve fits from NASA [60] and their mixing rules follow the kinetic theory [61].

b. Computational domain

A three-dimensional computational domain is used for the simulations. The reasons for this approach are, first, previous research indicates that for wall heat flux predictions, a 3D treatment is necessary since a 2D axisymmetric domain has inherent shortcomings. Moreover, the cross section of the present chamber is quadrate, and therefore a 2D approach neglects to a large extent the 3D effects in the corners. The computational domain chosen includes the combustion chamber, the nozzle and, in order to obtain a more precise injection status, the 80 mm long channels of propellants. Considering the high cost of computational resources, the computational domain has been simplified to a quarter of the chamber, where symmetry boundary conditions are imposed at the cut planes. Figure 3.1 provides the outline of the computational domain and the view is compressed by a factor of 0.1 in the z-direction.

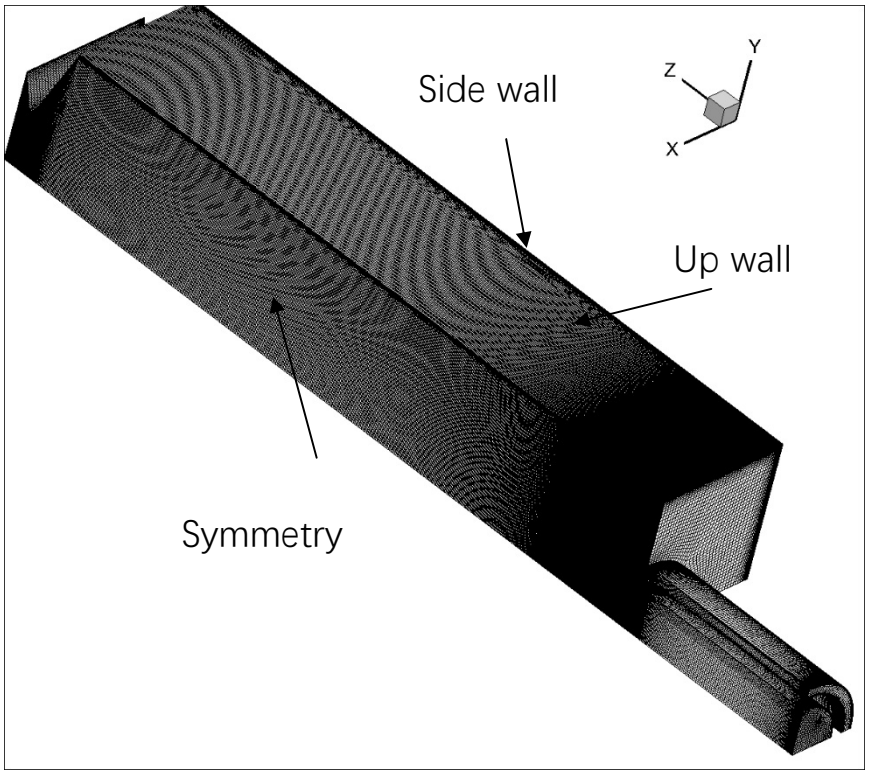

Figure 3.1 Computational domain

c. Reaction mechanisms

In the present case, methane kinetics is modelled by reduced chemical mechanisms Mechanism 101 with 22 species and 58 reactions, GRI 3.0 with 53 species and 325 reactions [3], REDRAM with 22 species and 34 reactions [62] and Slavinskaya with 24 species and 100 reactions are imported [63]. Mechanism 101, GRI 3.0 and REDRAM are implemented in EDC model and Mechanism 101 and Slavinskaya are adopted for flamelet tabulation.

d. Thermodynamics model

In this simulation, the ideal gas equation of state is utilized for the closure of governing equations, which is reasonable for present pressures and temperatures in the chamber.

e. Wall treatment and boundary conditions

Cells in the wall boundary layer play a crucial role in flow field prediction. The meshes in the vicinity of the wall should be very dense. To resolve the near-wall flow parameters, a two-layer k-ε model is enabled. An enhanced wall treatment is used to enable the near-wall region to be resolved down to the wall, which is important for heat transfer prediction [49,64]. A mesh containing 6.497 million hexahedral cells with near-wall resolutions of $y^+<1$ is generated with Pointwise [65]. Boundary conditions are shown in Table 3.1.

Table 3.1 Boundary conditions

Inlet of methane and oxygen	Mass flow inlet
Up wall	No slip condition; Temperature in Figure 3.2
Side wall	No slip condition; Temperature in Figure 3.2
Other walls	No slip condition; Adiabatic walls
Symmetry plane	Symmetry
Outlet pressure	Constant at 101325 Pa

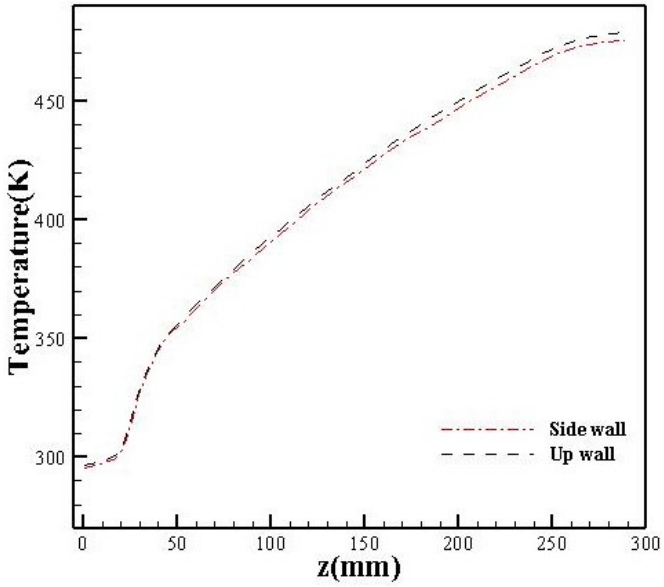

Figure 3.2 Axial wall surface temperature profile as boundary conditions

3.3 Mesh Verification

The mesh study is conducted by several refinements of the mesh following Richardson's Extrapolation Method [66,67]. By these means, to verify the discretization method, the eddy-dissipation model with a temperature limited to 3,700 K and adiabatic wall boundary conditions are used. A scalar Φ is approximated with

$$\Phi_0 \approx \Phi_1 + (\Phi_1 - \Phi_2)/(r_{1,2}^{\varphi} - 1) \tag{3.23}$$

Here Φ_1 and Φ_2 represent the simulation results from the fine and middle grids (refinement wise), $r_{1,2}$ represents the grid refinement ratio, and φ represents the observed order of grid convergence. φ is affected by the spatial discretization method. In the respect of three grids for a three-dimensional domain with decreasing numbers of cells (fine, middle and coarse), the grid refinment ratio $r_{1,2}$ is expressed as

$$\boldsymbol{r_{1,2} = [(\#\ \text{of cells of the fine grid})/(\#\ \text{of cells of the middle grid})]^{1/3}} \tag{3.24}$$

By solving the following equation iteratively, the observed order of convergence φ is computed.

$$\boldsymbol{\varepsilon_{2,3}\%/(r_{2,3}^{\varphi}-1)=r_{1,2}^{\varphi}[\varepsilon_{1,2}\%/(r_{1,2}^{\varphi}-1)]} \tag{3.25}$$

Here "3" represents the coarse grid and the Richardson Error Estimator $\varepsilon_{n,n+1}$ is given by

$$\boldsymbol{\varepsilon_{n,n+1}\%=100(\Phi_{n+1}-\Phi_n)/\Phi_n} \tag{3.26}$$

Here n=[1,2,3] represents the fine, middle and coarse grids. The GCI (grid convergence index) is obtained by

$$\boldsymbol{GCI_{1,2}\%=F_s|\varepsilon_{1,2}\%|/(r_{1,2}^{\varphi}-1)} \tag{3.27}$$

Here F_s represents the factor of safety, which is set to 1.25. Furthermore, α is expressed as

$$\boldsymbol{\alpha=GCI_{2,3}\%/GCI_{1,2}\%} \tag{3.28}$$

When $\boldsymbol{\alpha/r_{1,2}^{\varphi}\approx 1}$, the asymptotic value $\boldsymbol{\Phi_0}$ is recognized as grid independent. The $\boldsymbol{\Phi}$ in Eq. 3.23 is the static pressure at the point x,y,z (3mm, 3mm, 250mm). The results in Table 3.2 show that the grids are inside the asymptotic convergence region, because $\boldsymbol{\alpha/r_{1,2}^{\varphi}\approx 1}$. In addition, the observedorder of convergence is $\boldsymbol{\varphi\approx 2}$, which indicates second-order accuracy of discretization in space. Moreover, the uncertainty of $\boldsymbol{\Phi}$ is 0.12% for the fine grid, and 0.05% for middle grid. All the following simulation results have been achieved by apllying a mesh, which contains 6.497 million hexahedral cells.

Table 3.2 Grid convergent results and uncertainty verification

Grid n	# of Cells	Φ (p at point) (Pa)	$r_{1,2}$	1.4513	φ	2.082
1	7269708	1763200	$r_{2,3}$	1.4133	Φ_0 (Pa)	1763968
2	2378004	1762300	$GCI_{1,2}\%$	0.05	$\alpha/r_{1,2}^{\varphi}$	1.000803
3	842447	1760540	$GCI_{2,3}\%$	0.12		

4. Mechanism Reduction

4.1 Reaction Rates and Orders

The rate law offers a mathematical relationship of reaction rate with reactant concentrations. To measure reaction rates, chemists initiate the reaction, measure the concentration of the reactant or product at different times as the reaction progresses, perhaps plot the concentration as a function of time on a graph, and then calculate the change in the concentration per unit time. This law shall be introduced for a chemical reaction [68] that is expressed in general form by:

$$A + B + C + \ldots \xrightarrow{k} D + E + F + \ldots \tag{4.1}$$

where A,B,C… represent the species in the reaction. For species A, the rate is shown as

$$\frac{d[A]}{dt} = -k \cdot [A]^a [B]^b [C]^c \ldots \tag{4.2}$$

whereby, a,b,c… are reaction orders regarding the species A,B,C…., and k is the reaction's rate coefficient, which is specific for a particular reaction at a given temperature. The rate law can be determined experimentally using the method of initial rates, whereby the instantaneous reaction rate is measured immediately upon mixing the reactants. The process is repeated over several runs or trials, varying the concentration of one reactant at a time. These runs can then be compared so as to elucidate how changing the concentration of each reactant affects the initial rate. Rate laws are determined experimentally and cannot be predicted by reaction stoichiometry. The order of reaction describes how much a change in the amount of each substance affects the overall rate, and the overall order of a reaction is the sum of the orders for each substance present in the reaction. Reaction orders are typically first order, second order, or zero order, but fractional and even negative orders are possible. A surfeit of some species often exist; in these situations, their concentrations change little. By adopting $k_{exp} = k \cdot [B]^b [C]^c$ ..., one can express generically the simplified Eq. 4.2 in the following way:

$$\frac{d[A]}{dt} = -k_{exp} \cdot [A]^a \tag{4.3}$$

The instantaneous change of concentration of species *A* can be derived with the integration of Eq. 4.3. When a=1, the instantaneous behavior is given as:

$$ln\frac{[A]_t}{[A]_0} = -k_{exp}(t - t_0) \tag{4.4}$$

whereby $[\mathrm{A}]_0$ and $[\mathrm{A}]_\mathrm{t}$ denote the concentrations of species A at time t_0 and t, respectively. As a result, when a=2 this behavior is expressed as:

$$\frac{1}{[\mathrm{A}]_\mathrm{t}} - \frac{1}{[\mathrm{A}]_0} = k_{exp}(t - t_0) \tag{4.5}$$

If a=3, this behavior is shown as:

$$\frac{1}{[\mathrm{A}]_t^{\,2}} - \frac{1}{[\mathrm{A}]_0^{\,2}} = 2k_{exp}(t - t_0). \tag{4.6}$$

4.2 Relation of Forward and Reverse Reactions

Similar to Eq. 4.2, for the reverse reaction of Eq. 4.1 the rate law for production A can be developed as

$$\frac{d[A]}{dt} = k^{(r)}[D]^d[E]^e[F]^f \ldots \tag{4.7}$$

In theory, all thermal elementary reactions are reversible, which means that the reaction products may react with each other to reform the reactants. Reactions don't stop when they come to equilibrium, and the forward (f) and reverse (r) reactions are in balance at equilibrium, so there is no net change in the concentrations of the reactants or products, and the reaction appears to stop on macroscopic scale. Chemical equilibrium is an example of a dynamic balance between opposing forces-the forward and reverse reactions-not a static balance. Thus, the following equation can be derived:

$$k^{(f)} \cdot [A]^a[B]^b[C]^c \ldots = k^{(r)} \cdot [D]^d[E]^e[F]^f \ldots \tag{4.8a}$$

or

$$\frac{[D]^d[E]^e[F]^f \ldots}{[A]^a[B]^b[C]^c \ldots} = \frac{k^{(f)}}{k^{(r)}} \tag{4.8b}$$

Since $k^{(f)}$ and $k^{(r)}$ are constants, the ratio of $k^{(f)}$ divided by $k^{(r)}$ must also be a constant. This ratio is the equilibrium constant for the reaction, K_c. The ratio of the concentrations of the reactants and products is known as the equilibrium constant expression. No matter what combination of concentrations of reactants and products we start with, the reaction will reach equilibrium when the ratio of the concentrations defined by the equilibrium constant expression equals the equilibrium constant for the reaction. When the reaction reaches equilibrium, the relationship between the concentrations of the reactants and products described by the equilibrium constant expression will always be the same.

$$K_C = \frac{k^{(f)}}{k^{(r)}} = \exp(-\Delta_R \overline{A}^0 / RT). \tag{4.9}$$

4.3 Elementary Reactions

Reactions arising from a single collision between two molecules or ions are defined as elementary reactions, within which no macroscopically noticed intermediate exists between reactants and products. One such example of an elementary reaction is the formation of H_2O and H radicals from OH radicals and H_2:

$$OH + H_2 \rightarrow H_2O + H \tag{4.10}$$

Because of the constant random motion, in which the gaseous particles are at temperatures above absolute zero, the particles move in straight lines until the motion is interrupted by collisions with other particles or walls. For instance, during non-reactive collisions between OH radicals and H_2 molecules, they meet each other but bounce back, while in reactive collisions, they interact to cause a reaction and the formation of H_2O and H. In contrast, the reaction

$$2H_2 + O_2 \rightarrow 2H_2O \tag{4.11}$$

is not elementary: research has shown that a single collision among the three molecules will not produce water, and active radicals like H, O, and OH participate in the reaction process. In engineering applications, global reactions are extensively adopted within the characterization of reaction processes, assigning reaction coefficients to predict the reaction rates. Naturally, the merit of low cost comes with the narrow range of operating conditions. Typically, skeletal mechanisms are reduced with specific targets under given conditions such as temperature, equivalence ratio, and pressure. Any extrapolation outside these conditions can be imprecise or even disastrous.

Global reactions can be described by many elementary reactions that simulate the chemistry as it processes on a molecular level. The development of such detailed mechanisms is difficult and lengthy, while usage of these detailed mechanisms offers several merits. It provides the best accuracy and reliability. Several reaction systems interested in practical applications are characterized experimentally under different operating conditions. The detailed mechanisms can be adopted to interpret experimental results and to provide ideas for further research. In addition, the reaction order of elementary reactions is typically constant. This order represents the dependence of the reaction rate on the concentration of the reactants. It is common to determine the reaction order from experimental data: an assumption followed by validated tests. From molecularity, defined as the number of species which form the reaction complex, the reaction order can be easily obtained, as the molecularity often equals the order for elementary reactions. The molecularity is a parameter applied specifically to elementary reactions.

The empirical form of a unimolecular reaction is

$$A \rightarrow products \tag{4.12}$$

Unimolecular reactions typically represent a molecule's rearrangement or dissociation. For instance, the molecules A collide with others that exist in the mixture; this action supplies the energy required to overcome the energy barrier to a reaction, such as both the breaking and making of a bond.

Most gas phase reactions are bimolecular, a generic example is:

$$A + B \rightarrow products. \tag{4.13a}$$

or

$$A + A \rightarrow products. \tag{4.13b}$$

An alternate recombination reaction typically exists as shown in Eq. 4.13b. Several competing reaction pathways occur spontaneously. Pressure, temperature and equivalence ratio all affect the competitive outcome.

Trimolecular reactions, through which an active complex is formed from three species, do not commonly appear. Instead, a more careful examination of most trimolecular reactions reveals them to be multi-step reactions.

$$A + B + C \rightarrow products. \tag{4.14a}$$

or

$$A + A + B \rightarrow products. \tag{4.14b}$$

or

$$A + A + A \rightarrow products. \tag{4.14c}$$

In brief, for an elementary mechanism comprising *R* reactions of *S* species, given as

$$\sum_{s=1}^{S} \nu_{rs}^{(e)} A_s \xrightarrow{k_r} \sum_{s=1}^{S} \nu_{rs}^{(p)} A_s \quad \text{with r=1,…,R,} \tag{4.15}$$

the formation rate of a species *i* can be given by summation over all the rate equations:

$$\left(\frac{\partial[C_i]}{\partial t}\right)_{chem} = \sum_{r=1}^{R} k_r (\nu_{ri}^{(p)} - \nu_{ri}^{(e)}) \prod_{S=1}^{S} C_s^{\nu_{rs}^{(e)}} \quad \text{with i=1,…,S.} \tag{4.16}$$

where $\nu_{rs}^{(e)}$ and $\nu_{rs}^{(p)}$ represent stoichiometric coefficients of reactants and products.

4.4 Temperature and Pressure Dependence of Rate Coefficients

Typically, increasing the temperature raises the rates of chemical reactions; such rates are dependent upon the molecular collisions. Svante Arrhenius proposed that rate constants vary exponentially with the reciprocal of the absolute temperature:

$$k = A' \cdot exp\left(-\frac{E_a'}{RT}\right) \tag{4.17}$$

Experimental research has typically shown a slight temperature dependence of the pre-exponential factor A', compared with the exponential dependence,

$$k = AT^b \cdot exp\left(-\frac{E_a}{RT}\right) \tag{4.18}$$

The activation energy E_a represents an energy barrier that must be surpassed for reactive collisions to occur. This energy approximates the bond energies in the molecule, but it can be smaller if new bonds are made as the old bonds break.

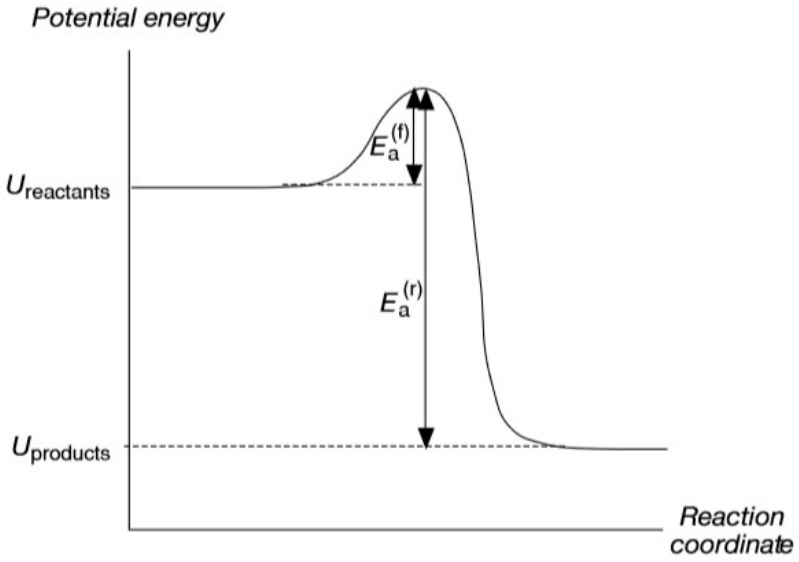

Figure 4.1 Energy diagram for a chemical reaction [68]

Resulting from Eq. 4.9, the formula $E_a^{(f)} - E_a^{(r)} = U_{products} - U_{reactants}$ can be derived. The reaction coordinate represents the path of minimum potential energy from reactants to products regarding the changing interatomic distance [68].
In general, the increase of pressure raises the rates of unimolecular reactions, in contrast with it decreasing the rates of chemically activated bimolecular reactions. At intermediate pressures (in fall-off region), the effect of pressure on the rate coefficients can be understood with the Lindemann model. Collisions among species in the gas create excited reactant species, among which the ones containing energy levels higher than a threshold decompose while others may be deactivated by collisions,

$$A + M \xrightarrow{k_a} A^* + M, \quad (activation) \tag{4.19a}$$

$$A^* + M \xrightarrow{k_{-a}} A + M, \quad (deactivation) \tag{4.19b}$$

$$A^* \xrightarrow{k_u} P(products) \ \ (unimolecular\ reaction) \tag{4.19c}$$

Following Eq. 4.3, the rate equations are shown as

$$\frac{d[\mathrm{P}]}{\mathrm{dt}} = k_u[A^*] \ \text{ and } \ \frac{d[A^*]}{\mathrm{dt}} = k_a[A][M] - k_{-a}[A^*][M] - k_u[A^*]. \tag{4.20}$$

Under the assumption that the concentration of the reactive intermediate A* is in a quasi-steady state,

$$\frac{d[A^*]}{\mathrm{dt}} \approx 0 \tag{4.21}$$

the concentration of the activated species $[A^*]$ and the formation of product P can be calculated as:

$$[A^*] = \frac{k_a[A][M]}{k_{-a}[M] + k_u} \tag{4.22a}$$

and

$$\frac{d[\mathrm{P}]}{\mathrm{dt}} = \frac{k_u k_a [A][M]}{k_{-a}[M] + k_u}. \tag{4.22b}$$

For calculations under the low- and high-pressure conditions, Arrhenius rate parameters are needed, which are blended by the Lindemann model to obtain the pressure-dependent rate expressions. Under low pressure, the concentration of collision partners M is minimal; under assumption that $k_{-a}[M] \ll k_u$, an approximate expression can be developed

$$\frac{d[\mathrm{P}]}{\mathrm{dt}} = k_a \cdot [A][M] = k_0 \cdot [A][M] \tag{4.23}$$

with a low-pressure rate coefficient typically referred to as k_0. The reaction rate varies with the concentrations of species A and the collision partner M, and the third-body collision is needed for providing the essential energy to lead the reaction because of the low activation under low pressures. Under high pressure, collision partner M has a large concentration and, together with $k_{-a}[M] \gg k_u$, an expression is shown as

$$\frac{d[\mathrm{P}]}{\mathrm{dt}} = \frac{k_u k_a}{k_{-a}}[A] = k_\infty \cdot [A] \tag{4.24}$$

with a high pressure rate coefficient k_∞. At high pressures, the effect from the collision partners on the reaction rate is negligible as species collide with each other frequently. As a result, the deactivation of molecule A* does not further limit the reaction rate.
Though the Lindemann model demonstrates that operating conditions have effects on the reaction orders, this model does not describe precisely the relation between the rate coefficients and the pressure variations. Typically, the theory of unimolecular reactions can be employed for the prediction of the pressure dependence of unimolecular reactions, as this theory contains a large number of activated molecules with different levels of activation.

Table 4.1 Example for Arrhenius parameters for pressure-dependent reactions

Reaction						A [cm, mol,s]		b	E/kJ· mol^{-1}
OH	+OH	+M(1)	$=H_2O_2$	+M(1)		$1.57 \cdot 10^{13}$		0.0	0.0
					LOW	$5.98 \cdot 10^{19}$		-0.8	0.0
					TROE	0.5	0.0	0.0	0.0

The correct treatment of pressure-dependent reactions is critical as experimental research on reaction kinetics is often conducted at atmospheric or lower pressures, while combustions occur at elevated pressures. Another description that involves more complex expressions is the F-Center treatment of Troe [69], whereby 10 parameters are employed to calculate a rate coefficient at a given operating condition (Table 4.1). In addition to the six Arrhenius parameters for the high pressure limit in the first line and low pressure limit in the second line, and the four parameters a, T***, T*, and T** used to calculate the F-center value are provided in the third line.

$$F_{cent} = a \cdot \exp(\frac{T}{T^*}) + \exp(\frac{T}{T^{**}}) + (1-a) \cdot \exp(\frac{T}{T^{***}}) \tag{4.25}$$

This is used to determine the value F via

$$\log F = \log F_{cent} \left\{ 1 + \left[\frac{\log P_r + c}{n - d \cdot (\log P_r + c)} \right]^2 \right\}^{-1} \tag{4.26}$$

with
C=-0.4-0.67logF$_{cent}$, n=0.75-1.27logF$_{cent}$, d=0.14, $P_r = k_0 \cdot [M]/k_\infty$
With this, one can compute the result

$$k = k_\infty \cdot \left(\frac{P_r}{1+P_r} \right) \cdot \mathrm{F} \tag{4.27}$$

4.6 The Full Methane Oxidation Mechanism

Many versions of a full mechanism, which reflects chemical reactions on a molecular level, have been developed for the numerical simulations, which are promising tools for the provision of more detailed information of the physical phenomenon. Full mechanisms exist in the modeling of premixed and non-premixed flames, ignition delay times, and burning velocities, and the simulations with these mechanisms correspond with the experiments. However, managing such high numbers of equations and species of full mechanisms typically requires expensive computational resource. As a result, reduced mechanisms are widely adopted in numerical simulations. These large chemical kinetic mechanisms can be reduced by many techniques, for example: 1) skeletal mechanisms, which can be achieved by removing unimportant reactions and species based on either specific or general applications, or 2) analytically reduced mechanisms, which typically assume a quasi-steady state or partial equilibrium.
Regarding hydrocarbon mechanisms, methane oxidation mechanisms are considered to be among the most highly investigated; thus, the most updated data of thermodynamic and transport properties from previous research exist for verification and validation. In this dissertation, GRI-Mech 3.0, which is developed for simulation of natural gas combustion containing NO generation and re-burn chemistry, is the full mechanism subject to reduction.
For the development of a mechanism adopted in the numerical simulation of combustion processes in a single-injector combustion chamber [70], the perfectly stirred reactor, PSR, with an adiabatic wall is implemented in Cantera [71] to analyze the 0D reaction path. In addition, the ignition delay is verified with the use of a constant pressure batch reactor against the experiments.

4.7 Zero-dimensional Computation of Combustion

A perfectly stirred reactor, PSR, is an idealization that contains continually injected fresh gases, which are supposed to mix instantaneously and perfectly with the gases in the reactor for the chemical reactions occurring. As a result, the reactants inside the reactor and exhausted productions are homogeneous, and descriptions of multidimensional compositions are obviated, thus allowing detailed reaction mechanisms to be adopted.

In a PSR, the cold condition solution and ignited ones are obtained at 2 MPa, according to the test case. In addition, the equivalence ratio ϕ of combustion is maintained at 1.51 by sustaining two continual injections of fresh gases at constant rates. To correspond to the test case, the fuel is injected at 269 K with oxygen temperature of 278 K. The gases in the reactor are kept at a ϕ of 1.51 at 300 K. In contrast with the autoignition in the batch reactors, radical induced ignition is adopted in the PSR. Propellants are ignited by an injection of H radicals as the temperature in the reactor is insufficient to stimulate the spontaneous ignition process. In rocket chambers, the chamber pressure is regulated by a convergent-divergent nozzle and influenced by the mass flow. In the PSR, this complex system is simplified by an exhaust tank included as a back pressure provider. As in the reactor, the nozzle is set with the same composition at 20 bar. Tables 4.2-4.4 indicate how the selected species concentrations vary with temperature. Theoretically, above 810 K ignition occurs spontaneously in the mixture of methane and air. In experiments, the spontaneous ignition of methane and air takes place above 873 K. At this temperature, Table 4.2 and 4.3 show the formation of HO_2 and consumption of methane, which indicate the ignition occurs in the PSR. These tables show the variation of the selected species concentrations at temperatures from 300 K to 3,424 K. The region beyond the tip of the test case, whereby the propellants meet prior to reaction, can be defined as the PSRs. In this region, velocity differences between the propellants generate shear forces that raise turbulence intensity, resulting in the mixture of two propellants at low temperatures. Under a well-mixed situation, the combustion process is dominated by the chemistry reactions. As shown in Tables 4.2-4.4, the mole fraction of CH_4 steadily declines above 873 K, while O_2 is gradually consumed from the beginning. As CH_4 is oxidized, CO is gently formed, and the generation of CO is one step earlier than that of CO_2, which is the final product. The fractions of OH and H, which are active radicals, sharply increase above 1,500 K. The HO_2 fractions in the PSR track similarly to those in CFD simulations of the combustion chamber (Fig. 5.21 and Fig. 5.22): they increase sharply before dropping, theoretically because the concentration of HO_2, which changes during the combustion process, is significantly influenced by other radicals and temperature.

Table 4.2 Comparison of O_2, CH_4, H_2O and CO_2 mole fractions with GRI 3.0 (GRI) and Mechanism 101 (101)

Tempera-ture (K)	Mole fraction of O_2		Mole fraction of CH_4		Mole fraction of H_2O		Mole fraction of CO_2	
	O_2(GRI)	O_2(101)	CH_4(GRI)	CH_4(101)	H_2O(GRI)	H_2O(101)	CO_2(GRI)	CO_2(101)
300.1882	0.5702309	0.57023	0.429731	0.429731	7.46E-09	3.68E-10	4.83E-21	1.68E-25
873.5028	0.524252	0.524869	0.41832	0.420242	0.015998	0.012866	2.93E-05	4.33E-06
900.9848	0.5202494	0.520774	0.414754	0.416767	0.021143	0.017761	5.02E-05	9.41E-06
1500.122	0.4196798	0.419361	0.316244	0.31022	0.156549	0.1574	0.002043	0.000726
2099.161	0.2854593	0.271617	0.185315	0.156374	0.284221	0.293562	0.010632	0.005408
2699.625	0.129808	0.122234	0.045275	0.030851	0.388075	0.416048	0.022547	0.02244
2849.463	0.096957	0.09078	0.011976	0.007552	0.413269	0.447931	0.029474	0.035337
3000.773	0.0667714	0.062005	0.002814	0.002755	0.416808	0.448738	0.036609	0.04645
3200.074	0.0308245	0.02951	0.000685	0.001826	0.412366	0.4418	0.044115	0.053028
3400.923	0.0038423	0.006027	7.76E-10	0.001056	0.391357	0.426824	0.05654	0.060289
3424.133	0.0040165	0.003531	7.67E-10	0.000575	0.385016	0.416816	0.053895	0.062302

Table 4.2 indicates that GRI 3.0 and Mechanism 101 predict same mole fractions of O_2, CH_4, H_2O and CO_2 with minor differences. O_2 and CH_4 are gradually consumed as the temperature increases. From 300 K to 873 K, approximately ten percent of O_2 has been consumed while only about two percent of CH_4 is burnt. The residual of O_2 and CH_4 with GRI 3.0 is slightly higher than those with Mechanism 101, while above 3,200 K more CH_4 is burnt with GRI 3.0. H_2O accumulates as the temperature increases to 3,200 K, after which a part of it decomposes. This decomposition is also found in the mole fraction of CO_2 with GRI 3.0 above 3,200 K, while the CO_2 concentration with Mechanism 101 rises along with the temperature increase.

Table 4.3 shows the mole fractions of active radicals O, OH and H, which may partially explain the difference between ignition delay with GRI 3.0 and Mechanism 101 in Table 4.5. The chain branching and propagating reactions are typically dominated by the active radical concentrations.

In the context of GRI 3.0, O and H radical concentrations are much lower than those with Mechanism 101 under 2,850 K, with OH concentration lower from 2,700 to 3,200 K. These active radical concentrations may also explain the relatively higher O_2 and CH_4 with GRI 3.0, as the more the active radicals, the faster the consumption of O_2 and CH_4.

Table 4.3 Comparison of O, OH, H and HO_2 mole fractions with GRI 3.0 and Mechanism 101

Tempera-ture (K)	Mole fraction of O		Mole fraction of OH		Mole fraction of H		Mole fraction of HO_2	
	O(GRI)	O(101)	OH(GRI)	OH(101)	H(GRI)	H(101)	HO_2(GRI)	HO_2(101)
300.1882	2.65E-14	5.12E-16	2.17E-13	1.30E-14	4.58E-13	4.62E-13	9.93E-07	9.98E-07
873.5028	3.25E-10	3.87E-08	4.92E-08	3.62E-08	4.98E-09	8.90E-09	8.43E-05	8.60E-05
900.9848	6.89E-10	8.27E-08	1.00E-07	7.63E-08	9.76E-09	2.01E-08	0.000112	0.000115
1500.122	7.00E-06	0.000116	0.000104	3.91E-05	3.75E-05	4.80E-05	0.001824	0.000661
2099.161	0.000116	0.000474	0.000742	0.00065	0.000538	0.000802	0.00096	0.000495
2699.625	0.000937	0.001767	0.00782	0.010323	0.008773	0.011157	0.000359	0.00027
2849.463	0.001852	0.003178	0.017733	0.024912	0.020574	0.023361	0.000163	0.000136
3000.773	0.002957	0.004108	0.027072	0.033878	0.030889	0.030389	7.49E-05	7.03E-05
3200.074	0.003878	0.004236	0.032737	0.03601	0.037325	0.033017	3.72E-05	4.35E-05
3400.923	0.005315	0.003954	0.039225	0.035541	0.391357	0.426824	1.68E-05	2.00E-05
3424.133	0.005779	0.003781	0.040888	0.034573	0.385016	0.416816	1.78E-05	1.37E-05

Table 4.4 explains the mole fractions of intermediate radicals H_2, CH_2O, CO and C_2H_6. CH_2O forms from the CH_3 and then dissociates to give HCO, which is the precursor to CO, representing an essential step on the C1 pathway. The C_2H_6 also comes from CH_3, whose appearance indicates the C2 pathway starts at low temperatures. H_2 radicals participate in many reactions including O, OH and typically H radicals, and have a close relationship with the active radical pool.

Table 4.4 Comparisons of H_2, CH_2O, CO and C_2H_6 mole fractions with GRI 3.0 and Mechanism 101

Temperature (K)	Mole fraction of H_2		Mole fraction of CH_2O		Mole fraction of CO		Mole fraction of C_2H_6	
	H_2(GRI)	H_2(101)	CH_2O (GRI)	CH_2O (101)	CO(GRI)	CO(101)	C_2H_6 (GRI)	C_2H_6 (101)
300.1882	4.45E-11	3.55E-13	7.09E-09	1.25E-11	7.63E-14	2.41E-22	5.33E-14	1.99E-19
873.5028	0.000442	0.000448	0.005919	0.006054	0.003405	0.002221	9.10E-05	2.38E-05
900.9848	0.000515	0.000563	0.007272	0.007663	0.004862	0.003582	0.000152	4.48E-05
1500.122	0.014183	0.020742	0.024507	0.029009	0.052173	0.052538	0.003712	0.005511
2099.161	0.065435	0.085916	0.010993	0.015474	0.121486	0.129529	0.005152	0.004572
2699.625	0.147538	0.134733	0.002955	0.006862	0.194507	0.180762	0.000336	0.000231
2849.463	0.172946	0.140272	0.001339	0.003787	0.229282	0.202191	2.74E-05	1.80E-05
3000.773	0.184887	0.15065	0.000547	0.002457	0.250888	0.218741	1.79E-06	2.57E-06
3200.074	0.191859	0.161905	0.000181	0.001778	0.258433	0.227892	1.15E-07	1.06E-06
3400.923	0.20949	0.18187	4.25E-07	0.000901	0.245876	0.238265	1.38E-19	3.09E-07
3424.133	0.214134	0.193568	4.33E-07	0.000446	0.244606	0.243417	1.38E-19	8.62E-08

4.8 Comparisons of Ignition Delay Times of Mechanisms in Batch Reactors

The batch reactor is a mathematical approximation of corresponding laboratory reactors that are typically adopted to investigate homogeneous mass-action kinetics, and it mixes the propellants without inlet or outlet as combustion occurs. This reactor is widely adopted to characterize explosion limits [72]. In explosions of hydrogen or hydrocarbon-air mixtures, the temperature rises and, as a result, the explosion occurs after a certain induction time. This time is denoted as ignition delay time, which is characteristic of radical chain explosions. When ignition commences, fuel is burned to generate exponentially increasing radicals during chain branching while temperature remains unchanged. After a critical amount of methane has been consumed by the accumulating active radicals, thermal energy is liberated and temperature rises. This ignition process comprises overlapping physical and chemical processes which have characteristic times that combine to form an overall induction. For gaseous methane and oxygen, the physical processes include heating, diffusion, and mixing of the propellants, while the chemical processes encompass the kinetics of reactions. These effects from physical and chemical processes also exist in the rocket chamber. Near the injectors, the combustion process is dominated by the flow fields, while in the rear chamber it is dominated by chemistry reactions. The precision of induction time definition is affected by the measurement methods, such as fuel consumption, CO or OH formation, increase of pressure in a constant volume vessel, and increase of temperature in an adiabatic vessel. An ideal constant pressure batch reactor with adiabatic walls is adopted in Cantera to characterize the ignition delay, which is one measure for validation of

mechanisms. The ignition delay is a readily measurable quantity that is a function of initial temperature, pressure, and the reactant mixture composition [73], especially temperature, because of the temperature dependence of the underlying elementary reactions. Typically the ignition delay depends exponentially on the reciprocal temperature. The times of GRI 3.0, Mechanism 101 and Slavinskaya are denoted as 14.16 s, 5.29 s and 5.37 s separately. Corresponding to the test case, the simulations are conducted at 20 bar and a ϕ of 1.51 at operating conditions which are equated to those in the PSR in Chapter 4.7, corresponding to the test case. The ignition method in this batch reactor is adopted as autoignition: a spontaneous process whereby a combustible mixture undergoes chemical reaction leading to the rapid liberation of energy at a rate sufficient to sustain combustion without external energy.

Table 4.5 Temperatures during ignition with GRI 3.0, Mechanism 101 and Slavinskaya at different times

GRI 3.0		Mechanism 101		Slavinskaya	
Time (s)	Temperature (K)	Time (s)	Temperature (K)	Time (s)	Temperature (K)
0.000112	1000	0.000112	1000	0.000113	1000
5.030293	1001.305	1.989986	1001	2.985731	1001.004
10.05042	1007.791	3.491014	1007.106	4.076276	1007.049
13.54155	1050.111	4.927155	1050.425	4.731714	1050.095
14.1376	1250.072	5.259834	1250.437	5.209956	1250.53
14.15527	1451.205	5.282737	1450.62	5.346096	1450.066
14.15873	1650.057	5.289505	1651.326	5.369462	1650.889
14.16041	2301.419	5.29248	2301.266	5.373955	2301.754
14.16053	2801.661	5.292633	2801.732	5.37408	2802.524
14.16055	3000.758	5.292661	3001.284	5.374104	3000.326
14.16056	3101.813	5.292674	3100.303	5.374116	3101.133
14.16057	3200.64	5.292688	3201.659	5.374131	3202.109
14.16059	3300.588	5.292705	3300.578	5.374153	3300.98
14.16061	3400.615	5.292727	3400.286	5.37421	3400.352
14.16062	3420.137	5.292733	3420.797	5.374244	3420.143
14.16067	3440.05	5.29274	3440.475	5.374337	3440.076
14.16077	3450.051	5.292744	3450.766	5.374545	3450.03
14.16087	3455.011	5.292766	3490.235	5.374612	3451
14.16203	3459.032	5.292829	3521.491	5.375616	3452.526
35.40973	3459.033	5.294641	3459.033	5.375929	3452.527

The calculated temperature variations up to time are shown in Table 4.5, which demonstrates that GRI 3.0 and Mechanism 101 predict a temperature increase from 1,250 K to 3,460 K within 0.03 seconds, while that of Slavinskaya is within 0.16 seconds. The shorter increase time of GRI 3.0 and Mechanism 101 compared with that of Slavinskaya is theoretically because Mechanism 101 is reduced from GRI 3.0, and it inherits some characteristics of ignition delay from GRI 3.0 at high temperatures.

Interestingly, the ignition delay time of Mechanism 101 is 5.29 s, significantly different from that of GRI 3.0, 14.16 s, and is closer to that of Slavinskaya, 5.37 s. One explanation for this difference is the addition of CH_3O_2, which exists in the Slavinskaya mechanism. This influence is further discussed in Chapter 4.12. Another explanation of the difference in ignition delay time between GRI 3.0 and Mechanism 101 is that during the reduction process, the number of reactions has been reduced to 58. As GRI 3.0 encompasses more reactions, which might consume the active radicals during the accumulation process of the radical pool, GRI 3.0 takes more time for accumulation, but after ignition the active radicals are more than those in Mechanism 101, as shown in Tables 4.2-4.4. A phenomenon is that the temperature with Mechanism 101 reaches a peak of 3,521 K, and then rapidly declines back to 3,459 K, which is identical to that in GRI 3.0. This phenomenon is presumably because Mechanism 101's fewer reactions result in greater sensitivity in temperature in reacting to variations in species during the ignition process. After variations, the solution reaches equilibrium temperature with the GRI 3.0. Those different numbers of reactions of GRI 3.0 and Mechanism 101 result in different ignition delay times and processes.

4.9 Computation of Counterflow Non-premixed Flames

Typically, the movements of fuel and oxidizer are dominated by convection, and then they mix due to diffusion. In most cases, this is a three-dimensional process in which the convection is complex. To further investigate the non-premixed flames, experiments with simplification of these three-dimensional convections to one spatial dimension have been proposed, such as the Tsuji burner and the opposed-jet flow burner in which flow emanates from two ducts in an opposed-flow configuration. This burner is adopted under the assumption that the velocities of propellants leaving ducts are uniform across the duct surface at uniform temperature with homogeneous composition distributions. One laminar flow of methane leaves one duct and stagnates against the other flow of oxidizer from the opposing duct. Theoretically the stagnation surface is dominated by the two propellants' momentum fluxes, which is similar near the tip region in the rocket chamber. When the propellant momentum fluxes equal each other, the stagnation plane lies in the middle of the two ducts. If the momentum of one side surpasses that of the other, the stagnation nears the lower heat flux duct. With the restricted calculation of flow properties along the stagnation surface, adoption of the boundary layer approximation of Prandtl significantly simplifies the mathematical treatment of the flame to one spatial coordinate; thus, one obtains equations that have only time t and the spatial coordinate z as independent variables [68].

According to specific applications, solving equations requires setting boundary conditions, which are consistent with the test case conducted at the workbench at LTF in these simulations [70]. One flow stream is methane, which enters through the fuel pipe at 269 K, and the other is oxygen, which travels through the pipe at 278 K. The

equivalence ratio ϕ is set to 1.51 at 20 bar according to the test case [70]. For accuracy, the equations should be solved based on adequately fine mesh placement, typically in locations that have high gradients such as flame fronts. Due to the computational cost, the adoption of fine mesh in the whole region is impractical. As a result, computations proceed with iterative solutions. After the solutions converge based on the coarse mesh, the grids are refined to resolve the large gradient in the solution profile, or coarsened if over-resolved. In the 1D domains [71], the solution variables are evaluated, followed by further distributions to grid points for this 14 mm long reactor.

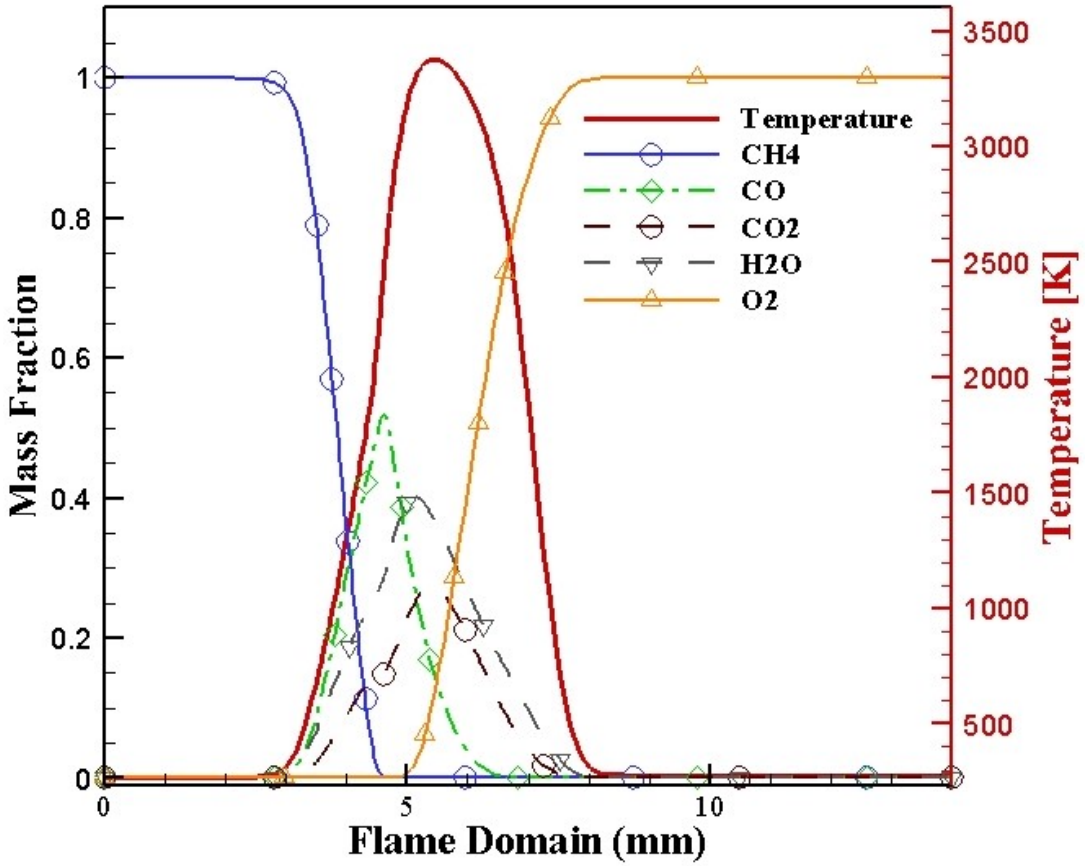

Figure 4.2 Mass fractions of selected species under counterflow flame structures

In this counterflow flame simulation, the methane is injected towards the surface at 0.51 kg/(m^2·s) and the oxygen at 1.35 kg/(m^2·s). Figure 4.2 shows the calculated temperature and selected species concentrations in the simulation results. The flame is centered at 5.425 mm, as recognized by the sharp temperature peak at 3,375 K and the radical species peaks. Typically, with high fractions of active radical species, such as H, O and OH, the highest reaction intensity exists at the peak temperature. Figure 4.3 clarifies that these active species and relatively active species HO_2 abound within the flame region in both the methane and oxygen sides, where these species concentrations hugely increase as temperature rises. Some penetration of oxygen through the flame into the fuel side is observed, while the CH_4 is consumed within the fuel rich side flame without penetration to the oxidizer side. The H_2O concentration has a broad peak, theoretically because this stable product diffuses outside the intense reaction zone along with its

radial outward convection. The CO accumulates on the fuel side of the flame, while the CO_2 exists in the center of the flame, nearer to the oxidizer side. During the reaction process, most heat is generated by the reaction OH+CO<=>H+CO_2. Figures 4.2 and 4.3 also indicate the C1 and C2 pathways at different temperatures. Theoretically the C2 pathway exists at low temperatures. This may explain the sharp increase and drop of C_2H_2 fractions. Figure 4.3 shows that the C_2H_2 accumulates during the ignition process when the temperature keeps constant, and reaches its peak near the region at 2,000 K. Then it drops steeply above 2,000 K, as more CH_3 go through the C1 pathway at high temperatures. Figure 4.3 also clarifies that the CH_2O fraction rapidly increases as the temperature rises, especially above 2,000 K, when the C_2H_2 drops. Due to the continued increase in temperature and number of active radicals, the CH_2O converts to CO, which then is oxidized to CO_2. Because of the oxidation of CO, the mass fraction of CO_2 increases and that of CO decreases, as shown in Figure 4.2. Figures 4.2 and 4.3 may indicate the C1 and C2 pathways inside the rocket chambers, especially in the region of film cooling, which is at low temperatures and at fuel rich conditions. At low temperatures, a part of the CH_3 goes through the C2 path, represented by the formation of C_2H_2. As the temperature increases, the CH_3 is transformed to CH_2O, CO and CO_2.

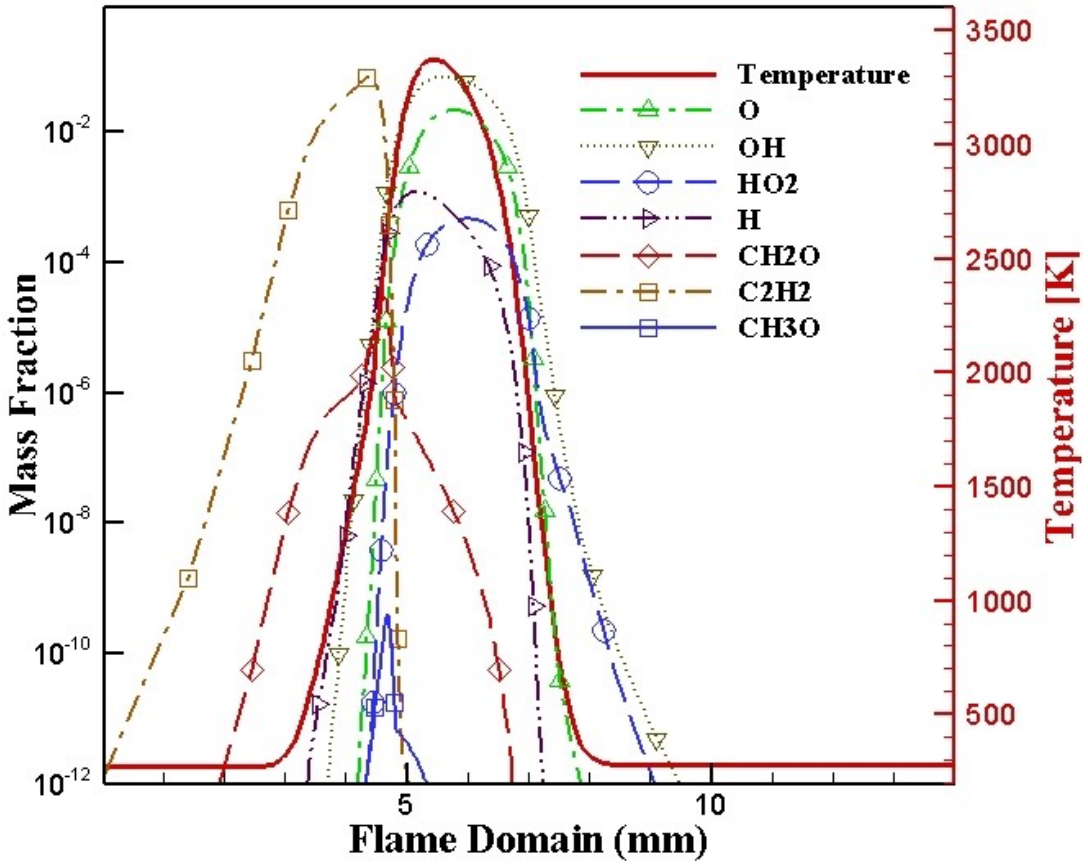

Figure 4.3 Mass fractions of active radicals, CH_2O, HO_2 and C_2H_2 under counterflow flame structures

4.10 Reduction Procedure

4.10.1 Reaction Path Analyses

Typically, species can be divided into important species, necessary species and redundant species. Important species here are the CH_4, O_2, CO, CO_2, H_2O, H, OH, O, HO_2 and other radicals that significantly influence the heat flux, combustion efficiency, corrosion of the chamber walls, soot formation and other parameters in the rocket chambers. Species that must be included to predict accurate results are defined as necessary species. These species are typically coupled to important species via significant reactions, such as CH_3O_2, which influences the ignition delay time at low temperatures and whose addition would improve the ignition delay prediction accuracy of GRI 3.0. Redundant species are not significantly coupled to the set of important or necessary species, and can be removed to reduce the computational cost. These removals of redundant species are studied by the analyses of the pathway of species. The formation and consumption paths of species in different flames, such as counterflow flames and PSRs, have been investigated. Net element fluxes between different species are calculated and shown. These flux calculations are summed as an integral of reaction rates of both forward and reversible reactions between the two species at the ends of the edges. The element fluxes have been standardized, as shown in Fig. 4.5 with the wider lines representing larger numbers and the narrower lines representing smaller figures. If the standardized value is lower than 20%, this species is removed.

4.10.2 Sensitivity Coefficients Analyses

Reduction methods are under fast development, such as sensitivity analysis, computational singular perturbation and quasi steady state approximation [68, 74,75,76,77]. Changes in the rate coefficients of many elementary reactions have negligible effects on the time-dependent solutions. However, changes in rate coefficients in several reactions have significant influences on the results, and these reactions are denoted as rate limiting reactions, which are typically identified by sensitivity analyses. Adiabatic flame temperature is selected as a target criterion because in a rocket combustion chamber, the temperature will influence the chamber pressure, heat flux through the walls and the performance of an engine. Sensitivity represents how the temperatures T at different times depends on the reaction *r*'s reaction rate k_r. Sensitivity coefficients are obtained by [68]:

$$S_r = \frac{k_r}{T}\frac{\partial T}{\partial k_r} \tag{4.38}$$

Under different conditions, dominant reactions for combustion are typically different. The maximum temperature T_{max}, the maximum temperature gradients against time T_{mag}, 1,700 K and 800 K are selected, as they represent the flame surface, high and low temperature regions respectively. Reactions whose sensitivity coefficients are higher than threshold are viewed as rate limiting reactions. In addition to the functions supported by Cantera in 0D calculations, 1D calculations' S_r in Eq. 4.38 can be

computed by increasing the reaction rate of every reaction. After equations of the counterflow flame are solved with the reaction rates from selected mechanisms (an intermediate mechanism and Slavinskaya), those equations will be solved again with a 1% increase in a reaction rate iteratively, applying the identical mesh. A finite-difference approximation provides a means to compute the sensitivity coefficient, which equals the ratio of the difference between the temperatures calculated with the increased reaction rates and the predicted temperatures with the initial reaction rates to the increase in the reaction rate.

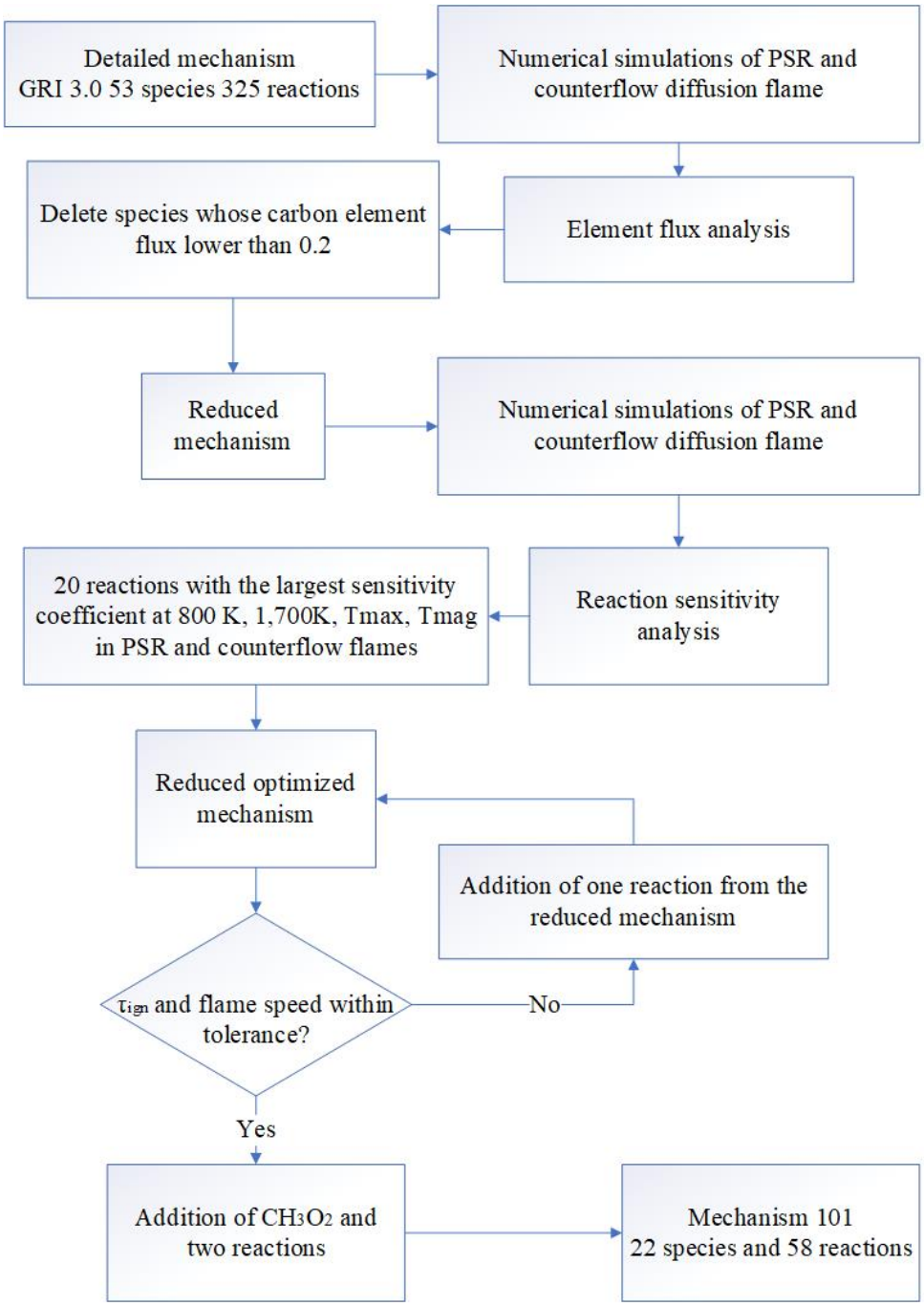

Figure 4.4 Development process of Mechanism 101

A flow chart of the reduction procedure is shown in Fig. 4.4, with the GRI-Mech 3.0 selected as the detailed mechanism. With it, the 0D simulation of the combustion process is performed using a PSR model, and a 1D simulation of a counter-flow diffusion flame is undertaken. In solutions from 0D and 1D simulations, reaction rates are integrated to calculate the element flux. If a species' element flux is smaller than 0.2, this species is removed and reactions that contain the species are correspondingly omitted. In this way, from the reduced mechanism (24S 130R) the next reduction cycle starts. With the reduced mechanism, 0D simulation of the combustion process is performed using PSR model and 1D simulation of a counter-flow diffusion flame is undertaken. Reaction rate sensitivity is analyzed at different temperatures. Reactions that have the highest 20 sensitivity coefficients at each temperature are selected, and other reactions are expurgated as unimportant reactions. Every reaction from unimportant reaction candidates is iteratively added to the first version of the skeletal mechanism to find reactions that have significant influence on τ_{ign} and flame speed with low sensitivity coefficients. Next, the redundant species in the first version of the skeletal mechanism without any reaction related to it are removed. Finally, Mechanism101 is obtained.

4.11 Mechanism Reduction Results

4.11.1 Comparisons of Reaction Paths with Different Mechanisms

0D simulations and 1D simulations have been conducted at 800 K, 1,700 K, and the maximum temperature gradient points T_{mag}. 0D simulations are performed in the reactor and at operating conditions described in Chapter 4.7. The maximum temperature gradient points of different mechanisms are at different temperatures. In the context of GRI 3.0, the highest temperature gradient is at 2,954.29 K. This gradient of Mechanism 101 is at 2,334.7 K, and that of Slavinskaya is at 2,388.48 K. This track corresponds to the temperature results in Table 4.5. The predicted temperatures of Mechanism 101 and Slavinskaya increase sharply within 5.4 s, while this process of GRI 3.0 takes more than 14 s. The pathways of different mechanisms at different temperatures may partially explain this time difference, even though the ignition type of PSRs and batch reactors are different.

The main pathway of C elements in the PSR simulations with GRI 3.0 at 800 K is:

$$CH_4 \rightarrow CH_3 \rightarrow CH_3O \rightarrow CH_2O \rightarrow HCO \rightarrow CO \rightarrow CO_2 \qquad \text{(Path 4.1)}$$

with Mechanism 101 this pathway is:

$$CH_4 \rightarrow CH_3 \begin{matrix} \nearrow CH_3O_2 \cdot \\ \searrow \end{matrix} CH_3O \rightarrow CH_2O \rightarrow HCO \rightarrow CO \rightarrow CO_2 \qquad \text{(Path 4.2)}$$

And with Slavinskaya this pathway is:

$$CH_4 \rightarrow CH_3 \begin{matrix} \nearrow CH_3O_2 \cdot \\ \searrow \end{matrix} CH_3O \rightarrow CH_2O \rightarrow HCO \rightarrow CO \rightarrow CO_2 \qquad \text{(Path 4.3)}$$

Comparisons of C elements pathways at 800 K among these three mechanisms indicate that the existence of CH_3O_2 significantly influences the formation pathway of CH_3O and the addition of CH_3O_2 promotes the ignition through the reaction $CH_3+O_2<=>CH_3O_2$. The effects of CH_3O_2 have been investigated in Huang's research [78]. At 1,050 K and 1,250 K, they also find the identical pathway of Path 4.1. A large proportion of methane reacts with OH to produce CH_3, from which CH_3O is generated through the reaction $HO_2+CH_3<=>OH+CH_3O$. In turn, the CH_3O is converted to CH_2O through the reactions $H+CH_2O(+M)<=>CH_3O(+M)$ and $CH_3O+O_2<=>HO_2+CH_2O$. These two reactions are much faster than the reaction $HO_2+CH_3 <=>OH+CH_3O$, because the concentration of CH_2O is higher than that of CH_3O by four orders of magnitude. This fraction difference is not only found in Huang's research, but also in Fig. 4.3: the mass fraction of CH_2O is several orders higher than that of CH_3O, thus the formation rate of CH_3O is considered to largely influence the ignition process. The addition of CH_3O_2 significantly promotes the ignition by providing a parallel pathway from CH_3 to CH_3O. In Mechanism101, this pathway is through reactions $CH_3+O_2<=>CH_3O_2$ and $CH_3O_2+CH_3<=>CH_3O+CH_3O$, and this pathway in Slavinskaya encompasses several reactions: $CH_3+O_2(+M)=CH_3O_2(+M)$, $CH_3O_2+CH_3=2CH_3O$, $2CH_3O_2=O_2+2CH_3O$, $CH_3O_2+H=CH_3O+OH$, $CH_3O_2+O=CH_3O+O_2$, and $CH_3O_2+CH_2O=CH_3O+OH+HCO$. Though the reactions in Mechanism101 differentiate from those in Slavinskaya, the addition of CH_3O_2 in these two mechanisms shows their influence on promoting ignition. The effects of the addition of CH_3O_2 are further shown in the ignition delay time validation in Chapter 4.12.

In addition to Path 4.1, the reaction pathways with GRI 3.0 at 1,700 K encompasses another C2 pathway:

$$\begin{array}{l} CH_4\rightarrow CH_3\rightarrow C_2H_6\rightarrow C_2H_5\rightarrow C_2H_4\rightarrow C_2H_3\rightarrow HCO\rightarrow CO\rightarrow CO_2 \\ \qquad\qquad\qquad\qquad\qquad\qquad\qquad\qquad\qquad\quad \downarrow \qquad\qquad \uparrow \\ \qquad\qquad\qquad\qquad\qquad\qquad\qquad\qquad\quad CH_2CHO\rightarrow CH_2CO\rightarrow HCCO \end{array} \qquad \text{(Path 4.4)}$$

The C2 pathway with Mechanism 101 at 1,700 K is:

$$CH_4\rightarrow CH_3\rightarrow C_2H_6\rightarrow C_2H_5\rightarrow C_2H_4\rightarrow C_2H_3\rightarrow C_2H_2\rightarrow CO\rightarrow CO_2 \qquad \text{(Path 4.5)}$$

During the development of Mechanism 101, CH_2CHO, CH_2CO, and HCCO have been eliminated from GRI 3.0, in which the complex network from C_2H_3 to CO has been simplified to $C_2H_3\rightarrow C_2H_2\rightarrow CO$ and $C_2H_3\rightarrow C_2H_2\rightarrow CH_2\rightarrow CO$ in Mechanism 101. The formation of CH_2 from C_2H_2 is also found in Wang's research [79].

The C2 pathway with Slavinskaya at 1,700 K is:

$$CH_4\rightarrow CH_3\rightarrow C_2H_6\rightarrow C_2H_5\rightarrow C_2H_4\rightarrow C_2H_3\rightarrow HCO\rightarrow CO\rightarrow CO_2 \qquad \text{(Path 4.6)}$$

In Slavinskaya, HCCO is an essential species, as it is involved in several reactions related to CO, CH_2O, HCO and O_2, but this mechanism does not contain C_2H_2. In contrast, Mechanism 101 includes C_2H_2 instead of HCCO. As temperature increases, the C element fluxes through CH_3O_2 gradually diminish.

At 2,954 K, when the temperature increases fastest, one pathway in GRI 3.0 becomes active:

$$CH_4\rightarrow CH_3\rightarrow CH_2O\rightarrow HCO\rightarrow CO\rightarrow CO_2 \qquad \text{(Path 4.7)}$$

and a part of C elements go directly through the path:

$$CH_4 \rightarrow CH_3 \rightarrow CO \rightarrow CO_2 \quad \text{(Path 4.8)}$$

In addition, with GRI 3.0 and Mechanism 101 the CH_2 appears in more pathways than at 800 K and 1,700 K.

At 2,940 K, with Mechanism 101 fewer C elements travel on the path through CH_3O_2 compared with 800 K and 1,700 K. Correspondingly, this path also exists similarly with GRI 3.0:

$$CH_4 \rightarrow CH_3 \rightarrow CH_2O \rightarrow HCO \rightarrow CO \rightarrow CO_2 \quad \text{(Path 4.9)}$$

At 2,892 K, with Slavinskaya the reduction of C element through CH_3O_2 is also noticed as with Mechanism 101. In addition, more CH_3 goes directly to C_2H_5 instead of C_2H_6 than in the path at 1,700 K:

$$CH_4 \rightarrow CH_3 \rightarrow C_2H_5 \rightarrow C_2H_4 \rightarrow C_2H_3 \rightarrow HCO \rightarrow CO \rightarrow CO_2 \quad \text{(Path 4.10)}$$

In Slavinskaya, at 2,892 K more C_2H_3 goes directly to CO than at 1,700 K. Wang [79] also explains the enhancement of combustion from the addition of hydrogen to methane in the view of an element ratio. Another factor could be bond energy. Admittedly, the energy of the H-H bond is 432 kJ/mol. It has no significant difference with the C-H bond (414 kJ/mol) in methane. However, each dissociation of H-H bond brings two hydrogen radicals, while a C-H bond brings one. In other words, more H radicals could be generated by the hydrogen molecule than the methane molecule, with the same number of dissociated bonds.

4.11.2 Comparison of 1D Reaction Path with Different Mechanisms

The 1D simulations are investigated in the counterflow flames at ϕ 1.51, which are introduced in Chapter 4.9. A representative reaction pathway with GRI 3.0 at T_{mag} (2,349.01 K) is shown in Fig. 4.5. Perez-Ramirez et al. [80] state that in general, methane is oxidized in one of two ways. One is through oxidation of CH_3, and then through further oxidation of CH_3O and CH_2O. The other way is that, after oxidation, CH_3 recombines with another CH_3 to format C2 hydrocarbons. The fuel equivalence ratio selects which way CH_3 will follow [80]. Under fuel-rich conditions, the formation of C2 hydrocarbons becomes easier. Under fuel-lean conditions, the likelihood of direct oxidation increases. In the counterflow flame, the C2 mechanism plays a more important role and the C2 mechanism's dominant influence is also found in Zhukov's research [81].

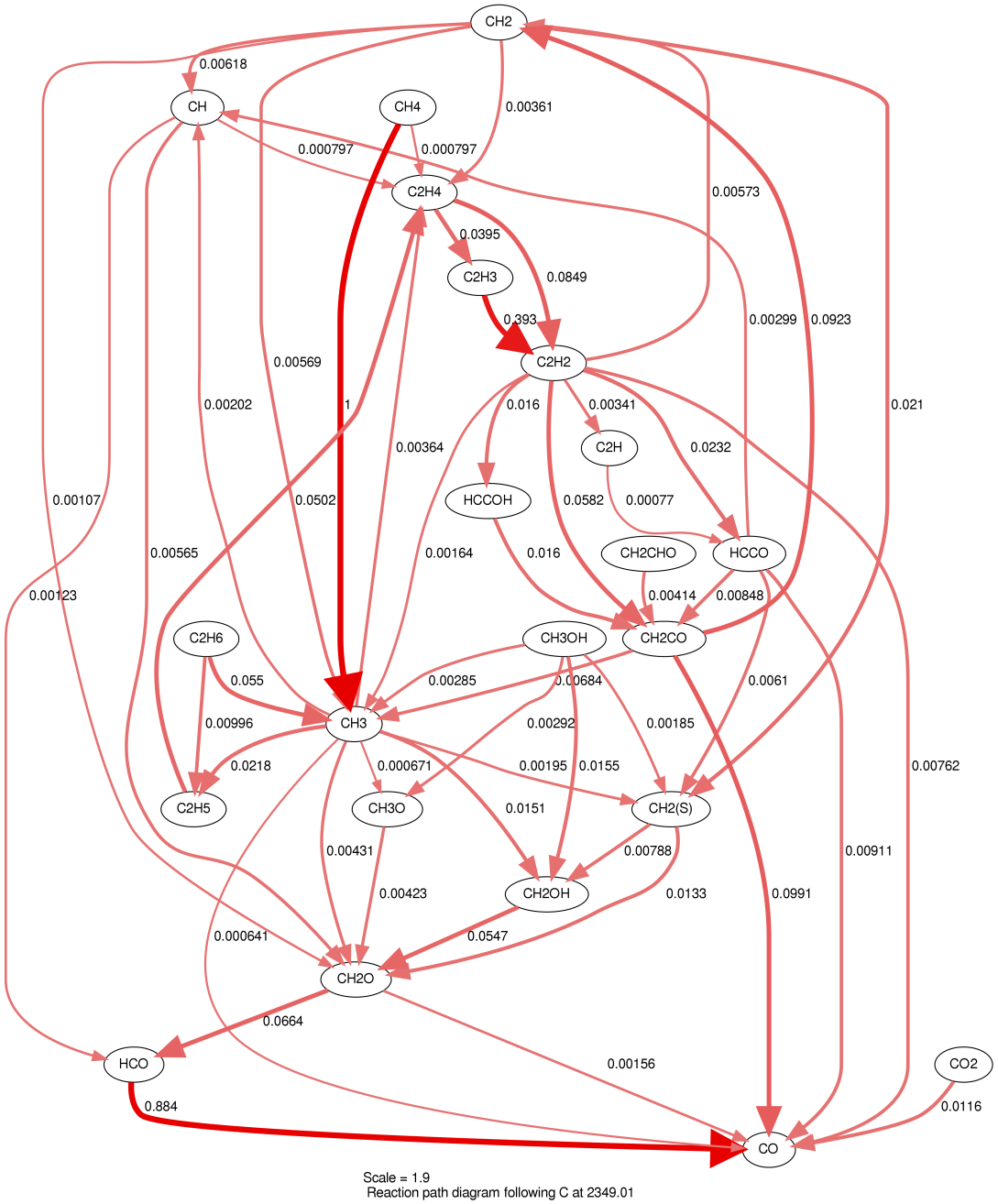

Figure 4.5 Pathway analysis at the location where T= 2,349.01 K

In the 1D counterflow flame, more CH_3 radicals go through the C2 pathway in all three mechanisms compared with those in the 0D PSRs at 800 K, presumably because of the equivalence ratio. As shown in Fig. 4.2, at 800 K the reactions are under fuel-rich conditions and the CH_3 prefers to go through the C2 pathway. Correspondingly, less CH_3 goes through the CH_3O_2 path both in Mechanism 101 and Slavinskaya.

4.11.3 Comparison of Sensitivity Coefficients in 0D and 1D Simulations with Different Mechanisms

At 800 K, 1,700 K, T_{mag}, and T_{max} sensitivity coefficients have been calculated for each reaction in both 0D and 1D simulations, following the procedure described in Chapter 4.10.2. These coefficients calculated with the reduced mechanism (24 species 130 reactions) are compared with those of Slavinskaya.

Table 4.6 Comparison of sensitivity coefficients of Slavinskaya and the reduced mechanism at T= 800 K in 0D PSR

Thirty reactions in Slavinskaya mechanism at 800K	Sensitivity coefficient	Thirty reactions in reduced mechanism(24s 130R) at 800K	Sensitivity coefficient
2OH (+M) <=> H2O2 (+M)	1	CH4 + OH <=> CH3 + H2O	1
H + H2O2 <=> H2O + OH	0.361761888	2OH (+M) <=> H2O2 (+M)	0.93422849
H + O2 (+M) <=> HO2 (+M)	-0.31331371	H2O2 + OH <=> H2O + HO2	-0.8219202
H + O2 (+O2) <=> HO2 (+O2)	-0.30486314	CH3 + HO2 <=> CH3O + OH	0.75141468
CH4 + OH <=> CH3 + H2O	0.251694729	H + H2O2 <=> H2O + OH	0.66621219
H2O2 + OH <=> H2O + HO2	-0.22080102	H + O2 + M <=> HO2 + M	-0.5603534
H + HO2 <=> 2 OH	0.217411946	CH3 + H2O2 <=> CH4 + HO2	-0.4815905
CH2O+CH3O2<=>CH3O+HCO+OH	0.166138801	H + 2O2 <=> HO2 + O2	-0.4155495
2OH (+H2O) <=> H2O2 (+H2O)	0.154606769	2HO2 <=> H2O2 + O2	-0.372928
2HO2 <=> H2O2 + O2	-0.10148666	H + HO2 <=> 2 OH	0.15848832
2CH3O2 <=> 2CH3O + O2	-0.08547375	CH2O + OH <=> H2O + HCO	-0.1540066
HCO + O2 <=> CO + HO2	-0.04189236	CH2O+HO2 <=> H2O2+HCO	0.12404014
HCO + O2 <=> CO2 + OH	0.041296283	2HO2 <=> H2O2 + O2	-0.1226393
H + O2 <=> O + OH	0.038509819	CH4 + H <=> CH3 + H2	0.12016699
CH3O2 + H <=> CH3O + OH	0.037392454	CH3 + HO2 <=> CH4 + O2	-0.1155743
CH2O + HO2 <=> H2O2 + HCO	0.02993105	H + O2 <=> O + OH	0.07640991
H + H2O2 <=> H2 + HO2	-0.02391015	H + H2O2 <=> H2 + HO2	-0.0277979
CH3 + HO2 <=> CH3O + OH	0.023870202	HO2 + OH <=> H2O + O2	-0.0204263
H + HO2 <=> H2 + O2	-0.01976923	CH2O + CH3 <=> CH4 + HCO	-0.0169772
CH3O + O2 <=> CH2O + HO2	-0.01879344	2 CH3 (+M) <=> C2H6 (+M)	-0.0166951
CH2O + H (+M) <=> CH3O(+M)	0.018629665	H + H2O + O2 <=> H2O+HO2	-0.0144884
2HO2 <=> H2O2 + O2	-0.01722344	CH3O + O2 <=> CH2O + HO2	-0.0102097
CH2O + OH <=> H2O+HCO	-0.01695746	CH2O+H(+M)<=>CH3O(+M)	0.01010183
CH4 + H <=> CH3 + H2	0.016574307	H + HO2 <=> H2 + O2	-0.0079218
HO2 + OH <=> H2O + O2	-0.01319699	CH4 + O <=> CH3 + OH	0.00755713
H + O2 (+H2O) <=> HO2 (+H2O)	-0.01091863	H + HO2 <=> H2O + O	0.00660312
CH4 + HO2 <=> CH3 + H2O2	0.005145395	H2O2 + O <=> HO2 + OH	-0.0055307
CH3 + CH3O2 <=> 2 CH3O	-0.00436761	CO + HO2 <=> CO2 + OH	0.00334553
CH3+O2 (+M)<=> CH3O2(+M)	-0.00317429	H2O2 + OH <=> H2O + HO2	-0.0024813
H + HO2 <=> H2O + O	0.002342545	CH2O + O <=> HCO + OH	-0.001258

Table 4.6 indicates that the reduced mechanism (24S 130R) predicts similar results with those of Slavinskaya, which can be explained by Huang's research [78]. This research points out that even though CH_4 reacts with HO_2, H and O radicals, the main proportion of CH_4 converted under attack of OH radicals; correspondingly, the reactions $CH_4+OH<=>CH_3+H_2O$, $2OH(+M)<=>H_2O_2(+M)$, and $H_2O_2+OH<=>H_2O+HO_2$ have the largest three sensitivity coefficients in the reduced mechanism from GRI 3.0 at 800 K. In the next step, CH_3 is mainly oxidized to CH_3O by HO_2. The importance of H_2O_2 and HO_2 is also verified by others [81,82].

Table 4.7 Comparison of sensitivity coefficients of Slavinskaya and the reduced mechanism at T=1,700 K

Thirty reactions in Slavinskaya mechanism at 1700K	Sensitivity coefficient	Thirty reactions in reduced mechanism(24s 130R) at 1700K	Sensitivity coefficient
2 OH (+M) <=> H2O2 (+M)	1	2 OH (+M) <=> H2O2 (+M)	1
H + H2O2 <=> H2O + OH	0.291686064	CH4 + OH <=> CH3 + H2O	0.572396
CH4 + OH <=> CH3 + H2O	0.273985525	CH3 + HO2 <=> CH3O + OH	0.56849316
H + O2 (+M) <=> HO2 (+M)	-0.25736163	H2O2 + OH <=> H2O + HO2	-0.4229762
H + O2 (+O2) <=> HO2 (+O2)	-0.25030662	CH3 + H2O2 <=> CH4 + HO2	-0.3510292
H2O2 + OH <=> H2O + HO2	-0.21887345	H + H2O2 <=> H2O + OH	0.24411969
2 OH (+H2O) <=> H2O2 (+H2O)	0.201518397	2 HO2 <=> H2O2 + O2	-0.2197265
H + HO2 <=> 2 OH	0.183699612	H + O2 + M <=> HO2 + M	-0.2079063
CH2O+CH3O2<=> CH3O+HCO+OH	0.174561195	H + 2O2 <=> HO2 + O2	-0.1524259
2 HO2 <=> H2O2 + O2	-0.08756292	2 HO2 <=> H2O2 + O2	-0.1311589
2 CH3O2 <=> 2 CH3O + O2	-0.08647252	CH2O + OH <=> H2O + HCO	-0.1282747
CH3 + HO2 <=> CH3O + OH	0.047916489	CH2O + HO2 <=> H2O2 + HCO	0.10923838
HCO + O2 <=> CO2 + OH	0.046015116	CH3 + HO2 <=> CH4 + O2	-0.0719452
HCO + O2 <=> CO + HO2	-0.04432711	H + HO2 <=> 2 OH	0.05771994
H + O2 <=> O + OH	0.042611672	CH4 + H <=> CH3 + H2	0.04751188
CH3O2 + H <=> CH3O + OH	0.034416593	H + O2 <=> O + OH	0.03618301
CH2O + OH <=> H2O + HCO	-0.0337307	2 CH3 (+M) <=> C2H6 (+M)	-0.0337007
CH2O + HO2 <=> H2O2 + HCO	0.032343388	CH2O + CH3 <=> CH4 + HCO	-0.0210223
CH2O + H (+M) <=> CH3O (+M)	0.027501341	H + H2O2 <=> H2 + HO2	-0.0137393
CH3O + O2 <=> CH2O + HO2	-0.02407263	CH3O + O2 <=> CH2O + HO2	-0.0135114
2 HO2 <=> H2O2 + O2	-0.02318787	CH2O + H (+M) <=> CH3O (+M)	0.01349446
H + HO2 <=> H2 + O2	-0.02189232	HO2 + OH <=> H2O + O2	-0.0131222
HO2 + OH <=> H2O + O2	-0.02076833	H + H2O + O2 <=> H2O + HO2	-0.0087899
H + H2O2 <=> H2 + HO2	-0.02052856	H2O2 + OH <=> H2O + HO2	-0.0062837
2 CH3 (+M) <=> C2H6 (+M)	-0.0161162	CO + HO2 <=> CO2 + OH	0.00550789
CH4 + H <=> CH3 + H2	0.010607956	H + HO2 <=> H2 + O2	-0.0038272
H + O2 (+H2O) <=> HO2 (+H2O)	-0.00951145	CH4 + O <=> CH3 + OH	0.00332814
CH3 + O2 <=> CH2O + OH	0.00771777	H + HO2 <=> H2O + O	0.00240861
CH4 + HO2 <=> CH3 + H2O2	0.004931722	H2O2 + O <=> HO2 + OH	-0.0023833
CH3 + CH3O <=> CH2O + CH4	-0.00378679	CH2O + O2 <=> HCO + HO2	0.00159628

Furthermore, as explained in Chapter 4.11.1, the formation of CH_3O, whose mole fraction is several orders lower than that of CH_2O as shown in Fig. 4.5, is the rate limiting reaction of the overall reaction rate. As a result, reactions $CH_3+HO_2<=>CH_3O+OH$, $H+O_2+M<=>HO_2+M$, $CH_3+H_2O_2<=>CH_4+HO_2$, $H+2O_2<=>HO_2+O_2$, $2HO_2<=> H_2O_2+O_2$, and $H+HO_2<=>2OH$ have the 4th, 6th, 7th, 8th, 9th and 10th largest sensitivity coefficients. The reactions $CH_2O+OH <=> H_2O+HCO$ and $CH_2O+HO_2 <=> H_2O_2+HCO$ describe the conversion from CH_2O to HCO, and this conversion is an essential step in all three mechanisms. Most of these reactions containing high sensitivity coefficients exist among the top ranked reactions in the Slavinskaya mechanism.

The 30 reactions with the highest sensitivity coefficients at 1,700 K in Slavinskaya and the reduced mechanism are listed in Table 4.7. A comparison of the top 30 reactions with Slavinskaya between 1,700 K and 800 K indicates that the rankings of several reactions slightly improve, such as the reaction $CH_4 + OH <=> CH_3 + H_2O$ rises from the fifth to the second, and the ranking of $CH_3 + HO_2 <=> CH_3O + OH$ climbs from 18th to 12nd. This climb also exists in several reactions in the reduced mechanism, for instance, the $2CH_3 (+M) <=> C_2H_6 (+M)$, which rises from 20th to 17th.

Comparing the coefficients of the reactions in Slavinskaya at 1,700 K and those at 3,420 K predicts that the rankings of the coefficients change slightly as the temperature increases. In the reduced mechanism from GRI 3.0, the coefficient of the reaction $CH_4 + OH <=> CH_3 + H_2O$ ranks first at 800 K, and then drops to second at 1,700 K. At 3,420 K, its ranking further drops to fourth, while that of this reaction in Slavinskaya maintains third position from 1,700 K to 3,420 K.

Tables 4.9 and 4.10 show the comparisons of sensitivity coefficients of reactions in Slavinskaya and the reduced mechanism at 800 K and T_{max} (3,377 K). As the equivalence ratio ϕ is 1.51 in the test case, under fuel rich conditions, coefficients are calculated at the fuel side, namely in the region smaller than 5.425 mm in Fig. 4.3. Different from the results in PSRs shown in Tables 4.6-4.8, the recombination pathways show large sensitivities both in Slavinskaya and the reduced mechanism in Tables 4.9 and 4.10, theoretically because of the equivalence ratio discussed in Chapter 4.11.2. The selection of C1 and C2 pathways is conducted by the equivalence ratio. As shown in Fig. 4.2, at the location where temperature is 800 K on the fuel side, the oxygen has been consumed before its penetration of the flame. As a result, the recombination reactions in the counterflow flames are much more sensitive than those in the PSRs.

The reaction $C_2H_2 + H (+M) <=> C_2H_3(+M)$ has the highest sensitivity in the reduced mechanism at 800 K. The influence of hydrogen addition onto C_2H_2 to generate C_2H_3 radicals on the burning velocities of alkanes has been investigated in other research [83,84,85]. The bond energy between the H atoms and C_2H_2 radicals are minor, and C_2H_3 tends to be dissociated. Correspondingly, the H atom generated through the reaction acts to promote the chain branching through the $H+ O_2 <=> OH+O$ reaction.

The reaction $2CH_3 (+M) <=> C_2H_6 (+M)$ is a well-known chain-termination reaction. At 1,250 K, 36 % of CH_3 radicals are converted through this reaction, and correspondingly in this way the ignition is inhibited. The reaction $2CH_3 <=> C_2H_5 + H$ is considered to act similarly with $CH_3 (+M) <=> C_2H_6 (+M)$ in the ignition-inhibiting step. In addition, the reaction $CH_3 + H (+M) <=> CH_4 (+M)$ reduces the activation energy at temperatures below 1,300 K by influencing on the methane decomposition. The reaction $C_2H_6 + H <=> C_2H_5 + H_2$ has the fifth largest coefficient in the reduced

mechanism from GRI 3.0, and its rate-determining role in the pathway from $C_2H_6 \rightarrow C_2H_4$ has been verified by Cao et al. [86].

Table 4.8 Comparison of sensitivity coefficients of Slavinskaya and the reduced mechanism at T= 3,420 K

Thirty reactions in Slavinskaya mechanism at maximum T 3420K	Sensitivity coefficient	Thirty reactions in reduced mechanism (24s 130R) at maximum T 3420K	Sensitivity coefficient
2 OH (+M) <=> H2O2 (+M)	1	2 OH (+M) <=> H2O2 (+M)	1
H + H2O2 <=> H2O + OH	0.29255372	CH3 + HO2 <=> CH3O + OH	0.67824138
CH4 + OH <=> CH3 + H2O	0.275332365	H2O2 + OH <=> H2O + HO2	-0.4937956
H + O2 (+M) <=> HO2 (+M)	-0.2568722	CH4 + OH <=> CH3 + H2O	0.44240832
H + O2 (+O2) <=> HO2 (+O2)	-0.2319558	CH3 + H2O2 <=> CH4 + HO2	-0.3416644
H2O2 + OH <=> H2O + HO2	-0.22231792	2 HO2 <=> H2O2 + O2	-0.2563521
2 OH (+H2O) <=> H2O2 (+H2O)	0.199790253	H + H2O2 <=> H2O + OH	0.20415389
CH2O +CH3O2<=>CH3O+HCO+OH	0.178358176	H + O2 + M <=> HO2 + M	-0.2038447
H + HO2 <=> 2 OH	0.170382029	H + 2 O2 <=> HO2 + O2	-0.14638
2 CH3O2 <=> 2 CH3O + O2	-0.08903978	2 HO2 <=> H2O2 + O2	-0.1418768
2 HO2 <=> H2O2 + O2	-0.08839153	CH2O + HO2 <=> H2O2 + HCO	0.11303513
CH3 + HO2 <=> CH3O + OH	0.055092177	CH2O + OH <=> H2O + HCO	-0.1087766
H + O2 <=> O + OH	0.048607679	CH3 + HO2 <=> CH4 + O2	-0.0637216
HCO + O2 <=> CO2 + OH	0.047222372	H + HO2 <=> 2 OH	0.0594876
HCO + O2 <=> CO + HO2	-0.03987885	CH4 + H <=> CH3 + H2	0.04494504
CH2O + OH <=> H2O + HCO	-0.03770286	H + O2 <=> O + OH	0.04002747
CH3O2 + H <=> CH3O + OH	0.035362801	2 CH3 (+M) <=> C2H6 (+M)	-0.0363448
CH2O + HO2 <=> H2O2 + HCO	0.033651649	CH2O + CH3 <=> CH4 + HCO	-0.0182383
CH2O + H (+M) <=> CH3O (+M)	0.029171827	H + H2O2 <=> H2 + HO2	-0.0134155
2 HO2 <=> H2O2 + O2	-0.02573917	HO2 + OH <=> H2O + O2	-0.0133593
2 CH3 (+M) <=> C2H6 (+M)	-0.02294768	CH3O + O2 <=> CH2O + HO2	-0.0130889
H + HO2 <=> H2 + O2	-0.02264798	CH2O + H(+M) <=> CH3O(+M)	0.01250338
CH3O + O2 <=> CH2O + HO2	-0.02256558	H + H2O + O2 <=> H2O + HO2	-0.0079191
HO2 + OH <=> H2O + O2	-0.02254381	H2O2 + OH <=> H2O + HO2	-0.0075413
H + H2O2 <=> H2 + HO2	-0.01882323	CO + HO2 <=> CO2 + OH	0.00549677
CH3 + O2 <=> CH2O + OH	0.010795686	CH4 + O <=> CH3 + OH	0.00435795
H + O2 (+H2O) <=> HO2 (+H2O)	-0.00860018	H + HO2 <=> H2 + O2	-0.003862
CH4 + H <=> CH3 + H2	0.008571564	H + HO2 <=> H2O + O	0.00295853
CH2O + O2 <=> HCO + HO2	0.005366959	CH2O + O2 <=> HCO + HO2	0.00183695
CH4 + HO2 <=> CH3 + H2O2	0.005228059	H2O2 + O <=> HO2 + OH	-0.001774

The sensitivity coefficients in counterflow flame at 800 K in Slavinskaya differentiate from those of the reduced mechanism. The reaction containing the largest coefficient is not C_2H_2 + H (+M) <=> C_2H_3(+M) because Slavinskaya does not include C_2H_2. As the operating condition is fuel rich, most sensitive reactions in Slavinskaya are also in the C2 pathways.

Table 4.9 Comparison of sensitivity coefficients of Slavinskaya and the reduced mechanism at T= 800 K

Thirty reactions in Slavinskaya mechanism at 800K	Sensitivity coefficient	Thirty reactions in reduced mechanism(24s 130R) at 800K	Sensitivity coefficient
C2H4 + OH <=> CH2O + CH3	-1	C2H2 + H (+M) <=> C2H3 (+M)	1
C2H4 + H (+M) <=> C2H5 (+M)	0.124291028	2 CH3 <=> C2H5 + H	-0.6810067
CH3 + CH4 <=> C2H5 + H2	0.079040999	2 CH3 (+M) <=> C2H6 (+M)	-0.562423
CH3O + CO <=> CH3 + CO2	-0.06641008	CH3 + H (+M) <=> CH4 (+M)	-0.4166254
CH4 + H <=> CH3 + H2	0.06095641	C2H6 + H <=> C2H5 + H2	-0.3707136
2 CH3 <=> C2H5 + H	-0.05881617	C2H4 (+M) <=> C2H2 + H2 (+M)	0.24707967
CO + OH <=> CO2 + H	0.044079608	C2H4 + H (+M) <=> C2H5 (+M)	-0.1866165
2 CH3 (+M) <=> C2H6 (+M)	-0.03890178	CO + OH <=> CO2 + H	0.17520719
C2H6 + H <=> C2H5 + H2	0.036841097	C2H2 + O <=> CH2 + CO	0.11200486
CH3 + H (+M) <=> CH4 (+M)	-0.02407829	C2H4 + H <=> C2H3 + H2	0.11069694
CO + OH <=> CO2 + H	0.018796629	C2H5 + H (+M) <=> C2H6 (+M)	-0.0462999
CO + OH <=> CO2 + H	0.017769735	C2H2 + OH <=> CH3 + CO	0.03670088
CH2O + H (+M) <=> CH3O(+M)	-0.01640265	C2H6 + OH <=> C2H5 + H2O	-0.0269924
C2H6 + CH3 <=> C2H5 + CH4	0.015615559	CH2 + CH3 <=> C2H4 + H	-0.0211488
CH3 + CH4 <=> C2H6 + H	-0.01041307	C2H4 + CH3 <=> C2H3 + CH4	0.01538155
H2 + OH <=> H + H2O	0.005418581	CH + H2O <=> CH2O + H	0.01247193
C2H4 + O <=> CH3 + HCO	-0.00370648	H2 + OH <=> H + H2O	0.00959996
C2H4 + M <=> C2H3 + H + M	-0.00265693	C2H6 + CH3 <=> C2H5 + CH4	-0.0095142
CH3 + O <=> CH2O + H	-0.00228371	H2 + O <=> H + OH	0.00826936
CH4 + OH <=> CH3 + H2O	0.001170004	CH + CH4 <=> C2H4 + H	-0.0053054
HCO + M <=> CO + H + M	-0.00107639	C2H3 + H (+M) <=> C2H4 (+M)	-0.0032143
CH2O + H <=> H2 + HCO	-0.00089609	CH2 + OH <=> CH2O + H	0.00245696
C2H4 + H <=> C2H3 + H2	0.000765352	CH3 + O <=> CH2O + H	0.00236057
CO + O + M <=> CO2 + M	0.000683835	C2H4 + OH <=> C2H3 + H2O	0.00217248
CH3 + HCO <=> CH4 + CO	0.000637257	CH3 + HCO <=> CH4 + CO	-0.0019431
C2H4 + OH <=> C2H3 + H2O	0.00059887	CH3 + OH => CH2O + H2	0.00189837
CH3 + OH <=> CH3O + H	-0.00054208	CH2 + H2 <=> CH3 + H	-0.0018583
CH2O + M <=> H + HCO + M	-0.00050545	C2H3 + H <=> C2H2 + H2	0.00179138
CH2O + OH <=> H2O + HCO	-0.00049607	CH3 + OH <=> CH2 + H2O	-0.0016277
C2H3 + C2H6 <=> C2H4+C2H5	0.000396866	CH4 + H <=> CH3 + H2	0.00151814

The comparison of sensitivity coefficients in Slavinskaya at 3,377 K and 800 K illustrates that the rankings of coefficients vary moderately. For instance, the ranking of reaction CO + OH <=> CO_2 + H rises from seventh to second position. One explanation for this increase of ranking is that most of the heat is released through this reaction, and the rate of this reaction has a more significant influence than at low temperatures. The ranking of the reaction CH_3O + CO <=> CH_3 + CO_2 drops from fourth to 23rd. Theoretically, this drop is because at 800K the reactions are under fuel rich conditions and little CH_3 goes through the C1 path. As a result, a minor change of the reaction rate of CH_3O + CO <=> CH_3 + CO_2 significantly influences the overall C1 pathway. However, at 3,377 K the equivalence ratio is much closer to 1 and a large part of CH_3 radicals go through the C1 path; correspondingly, the dominant effect of this reaction

decreases. The comparison of sensitivity coefficients in the reduced mechanism (24S 130R) in the counterflow flame between at 800 K and 3,377 K demonstrates that several rankings of reactions vary. The reaction containing the largest sensitivity has changed from C_2H_2 + H (+M) <=> C_2H_3 (+M) to C_2H_2 + O <=> CH_2 + CO. This difference can partially be explained by the element fluxes. At 800 K, the C element flux between the C_2H_2 is 0.215, while at 3,377 K it is 1. The difference between the fluxes at different temperatures indicates that as the temperature increases, the conversion rate from C_2H_3 to C_2H_2 also increases. As a result, the perturbation of the reaction C_2H_2 + H (+M) <=> C_2H_3 (+M) at 800 K is much less sensitive compared with that at 3,377K.

Table 4.10 Comparison of sensitivity coefficients of Slavinskaya and the reduced mechanism at maximum temperature T= 3,377 K

Thirty reactions in Slavinskaya mechanism at 3377K	Sensitivity coefficient	Thirty reactions in reduced mechanism(24s 130R) at 3377K	Sensitivity coefficient
C2H4 + OH <=> CH2O + CH3	1	C2H2 + O <=> CH2 + CO	1
CO + OH <=> CO2 + H	0.263733495	2 CH3 <=> C2H5 + H	-0.4533159
C2H4 + H (+M) <=> C2H5(+M)	0.190284484	C2H2 + OH <=> CH3 + CO	0.35284048
CH3 + CH4 <=> C2H5 + H2	0.146804986	C2H2 + H (+M) <=> C2H3 (+M)	0.33464271
CO + OH <=> CO2 + H	0.113514763	2 CH3 (+M) <=> C2H6 (+M)	-0.2880088
CO + OH <=> CO2 + H	0.111004135	C2H6 + H <=> C2H5 + H2	-0.2421992
H2 + OH <=> H + H2O	0.093276045	CO + OH <=> CO2 + H	0.22404209
CH4 + H <=> CH3 + H2	0.092699275	C2H4 + H (+M) <=> C2H5 (+M)	-0.1730243
2 CH3 (+M) <=> C2H6 (+M)	-0.06046945	CH + H2O <=> CH2O + H	0.1715742
C2H6 + H <=> C2H5 + H2	0.03090007	CH3 + OH => CH2O + H2	0.15273597
2 CH3 <=> C2H5 + H	-0.0274647	CH3 + H (+M) <=> CH4 (+M)	-0.1513317
CH3 + O <=> CH2O + H	0.018533914	H2 + O <=> H + OH	0.09183558
CH3 + H (+M) <=> CH4 (+M)	-0.01617572	C2H4 (+M) <=> C2H2 + H2 (+M)	0.08307661
C2H4 + OH <=> C2H3 + H2O	0.014994613	CH2 + CH3 <=> C2H4 + H	-0.0590241
C2H6 + CH3 <=> C2H5 + CH4	0.01343602	CH2 + OH <=> CH2O + H	0.04111836
CH2O + CH3 <=> CH4 + HCO	0.01057659	CH + CO2 <=> CO + HCO	0.03745412
C2H4 + O <=> CH3 + HCO	0.009771105	CH3 + O <=> CH2O + H	0.03548983
CH4 + OH <=> CH3 + H2O	0.008607044	C2H4 + H <=> C2H3 + H2	0.03318769
CH2O + H <=> H2 + HCO	0.008101673	CH3O + H <=> CH3 + OH	0.03231086
CH3 + OH <=> CH3O + H	0.006720756	CH + H2 <=> CH2 + H	0.02885717
CH3 + CH4 <=> C2H6 + H	-0.00576135	CH3 + O => CO + H + H2	0.02367072
HCO + HO2 <=> CO2 + H+OH	0.005640532	C2H5 + H (+M) <=> C2H6 (+M)	-0.0230432
CH3O + CO <=> CH3 + CO2	0.00534585	C2H6 + OH <=> C2H5 + H2O	-0.018364
C2H4 + H <=> C2H3 + H2	0.005021504	H2 + OH <=> H + H2O	0.01651006
CH3 + O2 <=> CH3O + O	0.004917059	CH + CH4 <=> C2H4 + H	-0.0152839
CO + HO2 <=> CO2 + OH	0.004569078	2 OH <=> H2O + O	0.01094204
CH2O + H (+M) <=>CH3O(+M)	0.004551656	CH2 + H2 <=> CH3 + H	-0.0070221
CH2O + HO2 <=> H2O2 + HCO	0.004457552	C2H6 + CH3 <=> C2H5 + CH4	-0.0062108
C2H5 + O <=> CH2O + CH3	0.004237321	CH3 + OH <=> CH2 + H2O	-0.0061295
CH3O + HO2 <=> CH2+ H2O2	0.00410329	C2H4 + O <=> CH3 + HCO	0.00530105

The conversion of C_2H_2 to CO encompasses several pathways: C_2H_2 directly to CO, $C_2H_2 \rightarrow CH_3 \rightarrow CH_2O \rightarrow HCO \rightarrow CO$ or $C_2H_2 \rightarrow CH_2 \rightarrow CH_2O \rightarrow HCO \rightarrow CO$. The high sensitivity coefficient of the reaction $C_2H_2 + O <=> CH_2 + CO$ indicates that the transformation from C_2H_2 to CH_2 is still a significant step at 3,377 K. Furthermore, the ranking of the reaction $CH_3+H(+M) <=> CH_4(+M)$ drops from fourth position at 800 K to 11th at 3,377 K. The analyzed reason is that at fuel rich condition the OH radical is insufficient and the CH_4 is attacked by the H radicals, while at 3,377 K more oxidizer is available and the CH_4 is converted with OH radicals, so that the sensitivity of the reaction $CH_3+H(+M) <=> CH_4(+M)$ decreases as the equivalence ratio changes.
Reactions containing the top 20 largest sensitivity coefficients in the reduced mechanism (24 species 130 reactions) are selected. During the research process, reactions $CH_3+O_2 \rightarrow CH_3O+O$ and $CH_3+O_2 \rightarrow CH_2O+OH$ are added because they are essential for the calculation of ignition delays, theoretically because the conversion from CH_3 to CH_3O is the rate limiting step in this pathway. In addition, reactions $CH_3O_2+CH_3 \rightarrow CH_3O+CH_3O$ and $CH_3+O_2 \rightarrow CH_3O_2$ are included from REDRAM [62] because of CH_3O_2's significant influence on the low temperature oxidation. Five reactions $H+H_2O+O_2 \rightarrow H_2O+HO_2$, $HO_2+OH \rightarrow H_2O+O_2$, $HO_2+O \rightarrow O_2+OH$, $CH_2+O_2 \rightarrow CO_2+2H$, and $CH_2O+H (+M) \rightarrow CH_3O (+M)$ are added for the accurate predictions of flame speeds at different equivalence ratios. Finally, Mechanism 101, containing 22 species and 58 reactions, is obtained.

4.12 Mechanism 101 Validation

Simulations of sets of experiments have been conducted to verify the validity of Mechanism101. A comparison with several other mechanisms has also been conducted, such as REDRAM (22 species 34 reactions)[62], RAMEC (38 species 190 reactions) [87], Slavinskaya et al. (24 species 100 reactions)[63], Tianfeng Lu et al. (17 species 73 reactions)[88], GRI Mech 3.0 (53 species 325 reactions)[3], Zhukov & Kong (23 species 51 reactions)[81], and Aramcomech 1.3 (253 species 1,542 reactions)[89].
The above-mentioned mechanisms have been validated against a series of experimental data under different conditions of equivalence ratios and pressures [90,91,92,93]. The predicted ignition delay times are shown in Fig. 4.6a-e. In Fig. 4.6a, it can be seen that at temperatures lower than 1,100 K, the GRI-Mech 3.0 overpredicts the ignition delay. This phenomenon is also pointed out in Goy's research [94]. This overprediction occurs because GRI-Mech 3.0 is only validated for temperatures greater than 1,350 K. As GRI-Mech 3.0 is unable to reflect the change in activation energy, which is seen in experiments, the predicted delay times diverge quickly from the experimentally measured delay times. As a descendent mechanism from GRI-Mech 3.0, Mechanism101 without CH_3O_2 shows the same trend. However, after the addition of CH_3O_2, Mechanism101's predictions have close agreements with the experiments.

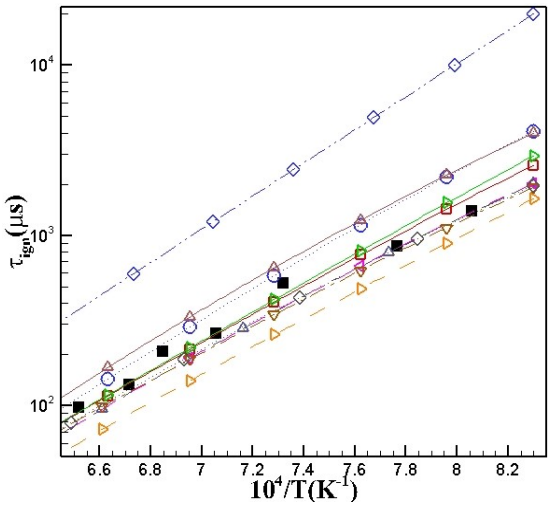

a)Φ=0.5 at 20atm, Petersen et.al (2007)

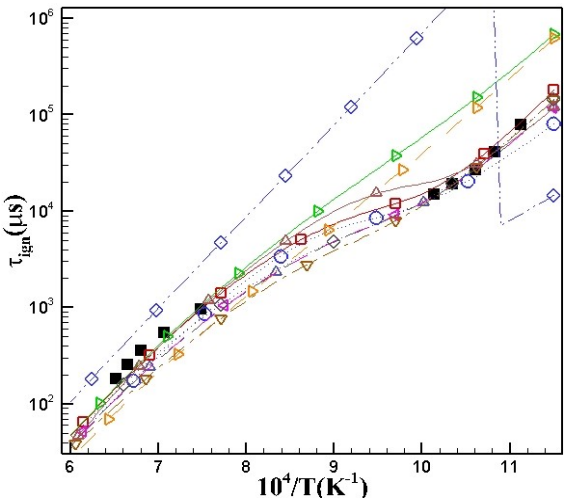

b)Φ=2 at 25atm, Burke et.al (2014)

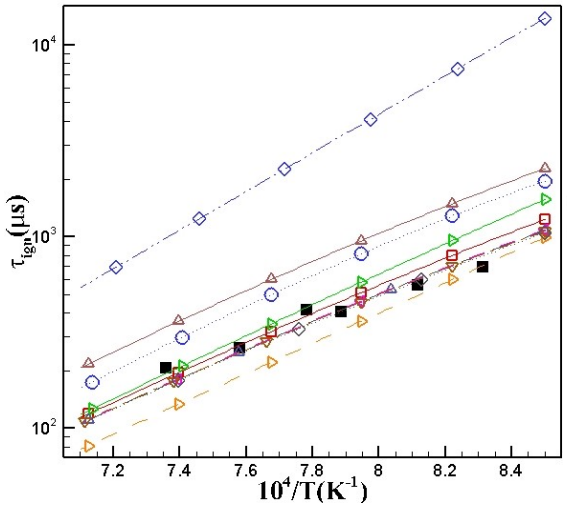

c)Φ=0.4 at 50atm, Petersen et.al (1999)

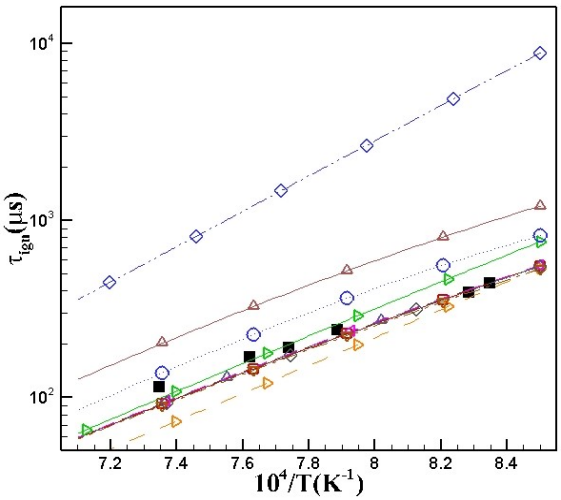

d)Φ=0.4 at 100atm, Petersen et.al (1999)

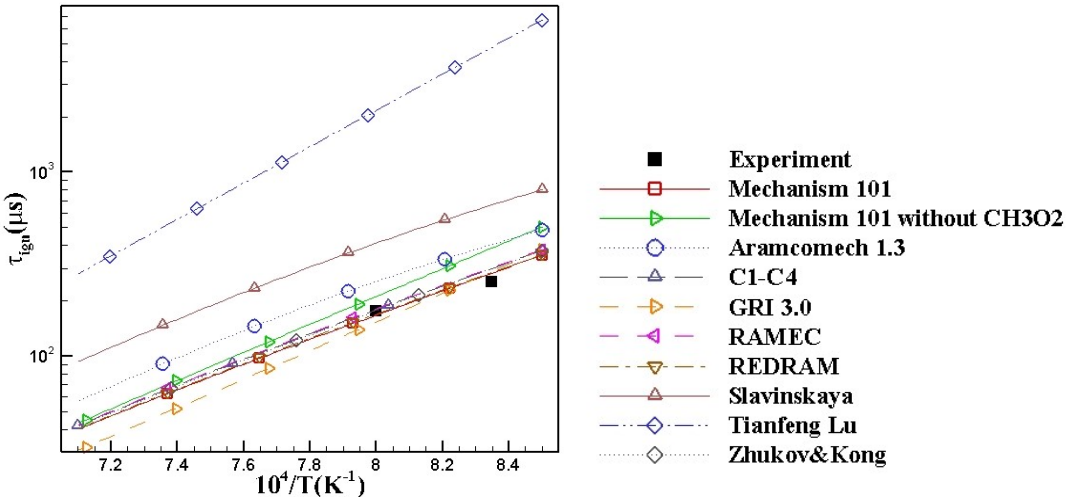

e) Φ=0.4 at 150atm, Petersen et.al (1999)

Figure 4.6 Comparison of performance of ignition delay prediction with other mechanisms

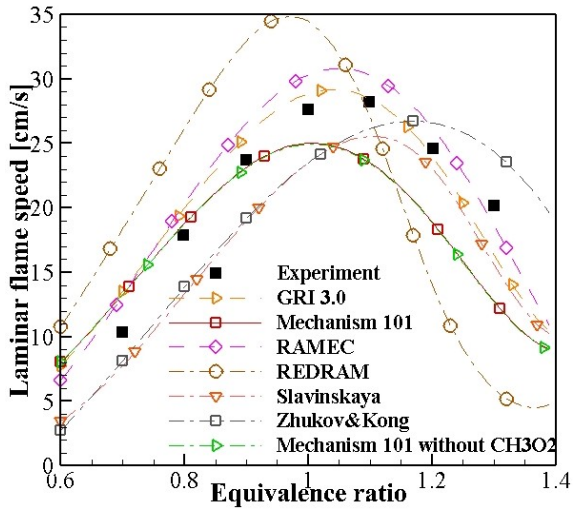

a) at 2atm, Rozenchan et.al (2002)

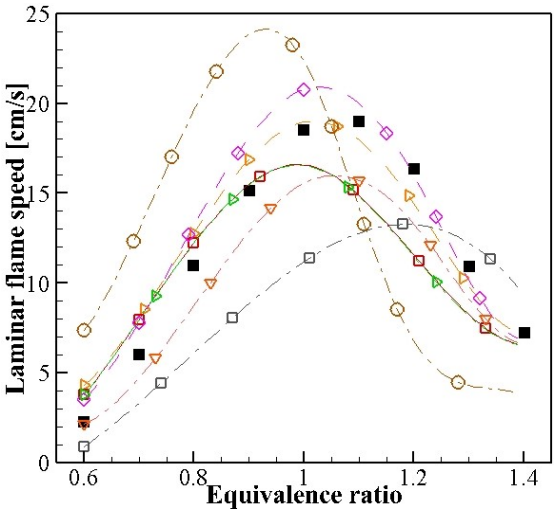

b) at 5atm, Rozenchan et.al (2002)

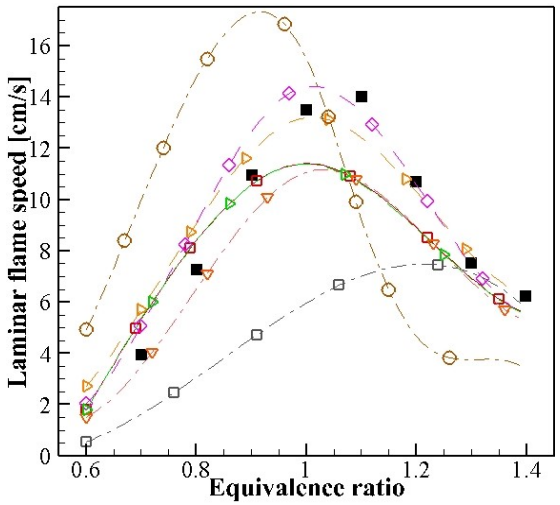

c) at 10atm, Rozenchan et.al (2002)

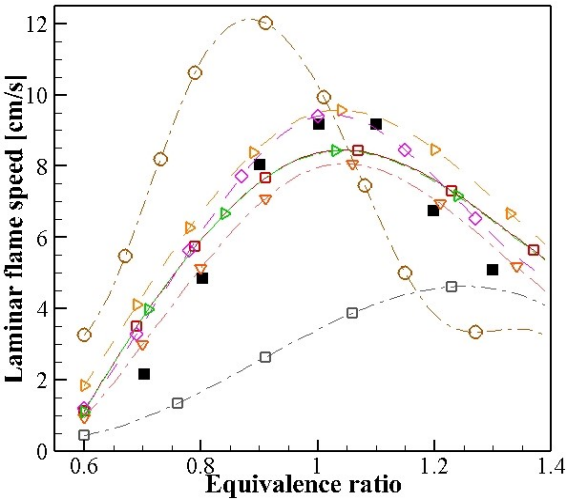

d) at 20atm, Rozenchan et.al (2002)

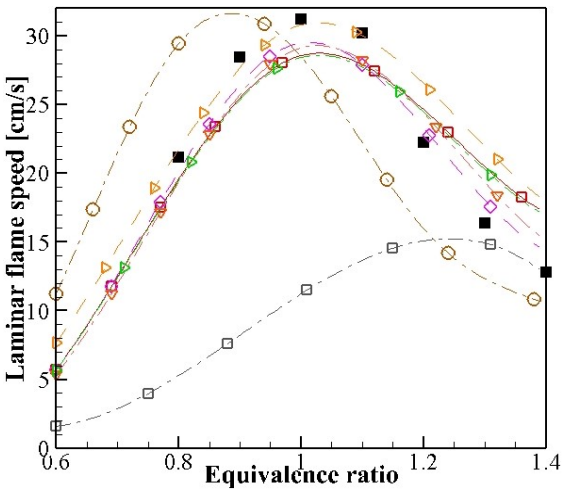

e) at 40atm, Rozenchan et.al (2002)

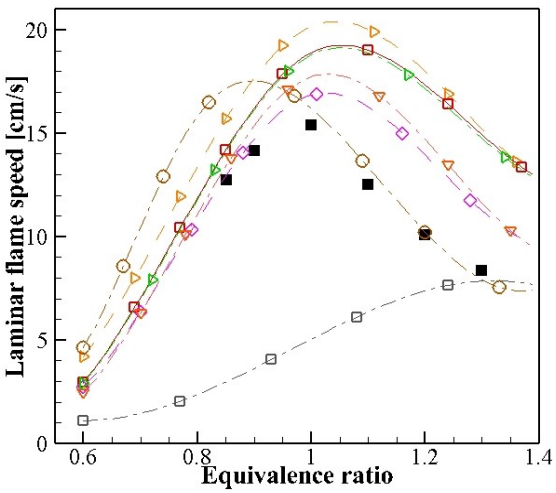

f) at 60atm, Rozenchan et.al (2002)

Figure 4.7 Laminar flame speed calculations with different mechanisms under selected operating conditions

Furthermore, Fig. 4.6 a-e illustrate that Mechanism101 gives reliable performance of ignition delay time predictions at different equivalence ratios and pressures. This performance indicates Mechanism101's potential to be used in numerical simulations for the combustion in the test case.

The laminar flame speed is one of the most important parameters of physicochemical properties of a combustible mixture, typically determined by the mixture ratio, initial temperature and pressure. As flame anchoring is an interesting topic for rocket engineers, an accuracy prediction of flame speed is essential for the simulations of flames and predictions of flame propagation speeds in the chambers. For instance, the simulations accurately reflecting the injectors' recess effects require mechanisms that exactly predict the laminar flame speeds and precise TCI models that accurately describe the complex combustion processes within millimeter regions. The flame speed is validated against a series of experiments under different conditions [95]. Calculation results are shown in Fig. 4.7 a-f. In sum, Mechanism101 precisely predicts flame speeds, and its utility in the simulation has been validated against the experiments.

5. Simulation Results and Discussion

The experiments have been carried out in the Institute of Turbomachinery and Flight Propulsion's Lab at the Technical University of Munich. The test rig comprises a coaxial shear injector, a square combustion chamber and a nozzle. The nozzle has a throat with a rectangular cross section. The rig features a contraction ratio of 2.5 which yields a Mach number of 0.25 similar to that of real rocket engine conditions. The single coaxial injector is flush mounted to the chamber faceplate. The dimensions of the chamber and injector can be found in [70]. Gaseous oxygen at 278 K enters the combustion chamber from the inner channel of the injector, and gaseous methane at 269 K enters from the outer channel. The mass flow of oxygen is 45 g/s and the parameter of methane is 17 g/s. The combustion chamber with a length of 290 mm has no cooling measures. The material used for the chamber and nozzle segments is oxygen-free copper. The nozzle is designed to control the chamber pressure. With the mass flow rate given above and the throat area, the nominal chamber pressure is set to 2 MPa. In the following, the results of the CFD simulations and the comparisons between experiment and numerical results with different models and mechanisms are presented and discussed, beginning with the flame structure and the combustion processes.

5.1 Temperature Distribution

The total temperature distribution of EDC Mechanism 101 in a plane perpendicular to the injection faceplate is shown in Fig. 5.1. A hot zone exists in the recirculation area of the post tip. The hot zone is the source of the flame which provides for flame anchoring at the post tip and downstream; the reaction zone expands gradually. This hot zone also indicates that the velocity difference between the methane and oxygen creates a shear force between these propellants, and the turbulence intensifies so that the mixture is strengthened and the chemical reactions speed up, resulting in an increasing temperature of hot gas near the tip between the two injectors. In the mixing region near the tip, the turbulence is intense: as the methane and oxygen are injected into the chamber through the inlet pipes, the sudden expansion of the gases induces violent disturbance. Though the temperature in this mixing region is moderate, the turbulence furthers the mixture of the propellants and, correspondingly, the chemistry reactions quicken. The acceleration of the flow near the injectors is rapid. Along the chamber length, the flow gradually plateaus and the turbulence caused by the injection expansion decreases. The flame is characterized by a rather moderate broadening of the reacting shear layer which approaches the combustion chamber wall slowly and helps to establish a thin low temperature boundary layer. But as the central hot gas gets closer to the wall, this low temperature layer shrinks to a roughly constant thickness from d=150 mm (d represents the distance from the faceplate) on downstream. Additionally, the flame seems to spread rather quickly towards the walls, which indicates a strong recirculation area that stretches only a few centimetres downstream. This flow behaviour results in both a heat flux peak and a wall pressure peak. Obviously, the entire evolution of flame behaviour and wall boundary layer will influence the local wall heat fluxes. Furthermore, as calculated based on CEA [96], the adiabatic flame temperature at equilibrium is 3,444 K,

which is at a stoichiometric value of 4.0 with oxygen and methane (O/F). The simulation cases in the present research are fuel rich (O/F=2.6). Due to the inhomogeneous mixing of the fuel and oxidizer in the chamber, some regions inside the chamber with O/F mixture ratio of 4.0 will exist, which makes the simulated maximum temperature comparable with the CEA results. Varying the selected thermodynamic data and product species results in little variation of this value, which denotes the maximum temperature that can be achieved during a combustion process. In the present view, the maximum temperature is 3,473 K, which approximates the adiabatic flame temperature.

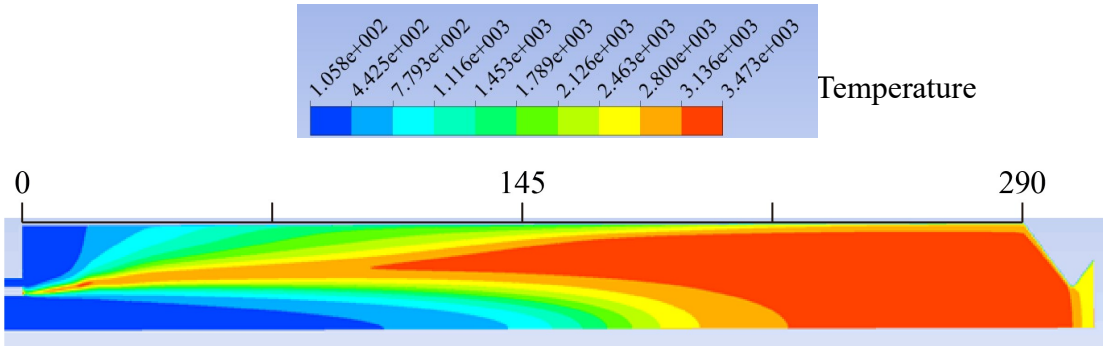

Figure 5.1 Static temperature distribution in the combustion chamber

5.2 Heat Flux Results

A comparison of experimental and numerical heat flux results is shown in Fig. 5.2. As stated in the data processing section, the experimentally determined heat flux at each axial position is an average, and therefore the results from the simulation presented here are also averaged in circumferential direction with an area-averaged method. In the test data, a steep rise shows at the beginning of the chamber, then after a slight decrease, a gradual ascent appears, followed by a relatively flat trend in the rear part of the combustor. As for the simulation result, in general, it evolves similarly to the experimental one. In the simulation result of EDC GRI 3.0, the heat flux rises sharply in the near injector region because the heat flux is influenced not only by chemical reactions but also by the turbulence flow. Heat released by the chemical reactions is brought to the wall by the recirculation of the methane. Consequently, the wall heat flux increases. As the flow leaves the intense recirculation region, the turbulent intensity decreases. In turn, the heat flux slightly declines. As the chemical reactions proceed, the combustion core in the centre gradually approaches the wall, accompanied by an enhancement of heat and mass transfer between the combustion core and boundary layers on the wall. As a result, the heat flux gradually increases along the axis direction. In the rear segment of the chamber, reactions are nearly completed, and the temperature becomes stable with minor fluctuations. The simulations of EDC GRI 3.0 and EDC Mechanism 101 precisely predict the position of the heat flux peak, even though the simulation result still has a quantitative difference with the experiment data in the near injector region. This difference, the peak heat flux value deviates from the experimental one, is also found in other works [97,98]. The reasons are twofold. Firstly, in the test rig, an insufficient number of thermocouples are equipped in the near injection region,

which leads to a lack of more detailed heat flux distribution information. Furthermore, the temperature difference between the propellants in the recirculation region and the wall is minimal, which increases the difficulty of precisely calculating the heat flux. Secondly, simulation is likely to underestimate the heat conveyed by the recirculating methane. This might come from an underestimation of the reaction rate in the mixing region near the tip. The intensive mixing in the tip region magnifies the reaction rate differences between experiment and simulation, which are negligible in other regions. Figure 5.2 illustrates that compared with the EDC Mechanism 101 results, the flamelet Mechanism 101 result reaches a plateau at d=200 mm (d represents the distance away from the faceplate), which presumably occurs when the combustion approaches equilibrium earlier than the other results. At this point, several factors may contribute to the formation of this plateau. The first conjecture, the effect on the heat flux from the gas compositions on the walls, is supported by the inherent attributes of the PDF methods: a mean parameter, i.e., the mixture fraction, is employed to calculate the intermediate species that are assessed for equilibrium conditions. Achieving a valid estimate of the real flame behavior in a state absent equilibrium is unlikely even if a non-equilibrium approach with the flamelet description is introduced [99]. Another factor may be attributed to the flamelet model, which is implemented in the non-premixed combustion model to account for chemical non-equilibrium. The flamelet model considers the turbulent flame as one group comprising thin, laminar, locally one-dimensional flamelet structures embedded within the turbulent flow field; in contrast, the EDC model assumes a steady state under which reactions occur in small turbulent structures. The EDC model simulates an “in-evolution chemistry phenomena” while a steady configuration is achieved in the flamelet model much more quickly. A third conjecture assumes that the EDC model clearly accounts for species transport properties, whereas the flamelet takes into consideration an overall transport property [100]. The figure also demonstrates that the result of the Large-Eddy simulation (LES) in Selle’s study [98] provides a close calculation of the axial evolution of the wall heat flux, indicating an accurate description of the flow and flame dynamics. However, in the recirculation zone the values are slightly underestimated and in the rest of the chamber somewhat overestimated. This overestimation was assumed to result from an insufficient mesh refinement at the walls [98]. The heat flux is influenced not only by the compositions on the walls, but also by the temperature gradient, which is affected by the grid resolution at the walls (the value of y^+). The computational cost of a wall-bounded Large-Eddy simulation depends strongly on the Reynolds number. For simulations with a high Reynolds number, such as the wall-bounded flows in this test case, the RANS EDC model significantly reduces the computational cost compared with that of the LES model.

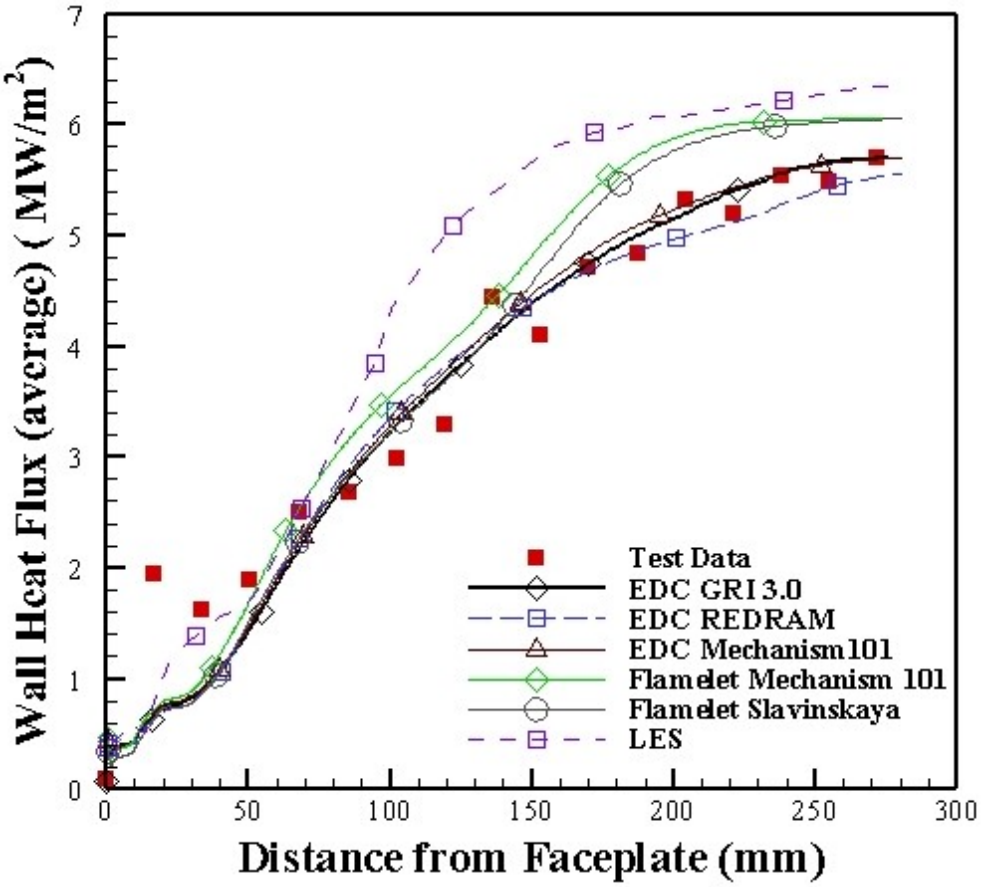

Figure 5.2 Heat flux distribution in the combustion chamber

5.3 Pressure Distribution

In addition to heat flux profiles, the experimental data for pressure distribution is also available, which allows for a different type of quantitative comparison between test and simulation results. Generally, the axial wall pressure profile can be considered a footprint of the axial distribution of the heat release. Heat addition due to the chemical reaction yields an acceleration of the flow and, as a result, a quadratic shape of the wall pressure decrease. Figure 5.3 illustrates the measured pressure distribution and pressure distribution of simulations in the axial direction. From the experimental data, it can be seen that a sudden rise occurs close to the injector, which is followed by a descent that tends to flatten out at the end of the chamber. This figure also shows the track of pressure in the simulation of EDC GRI 3.0， EDC Mechanism 101 and EDC REDRAM. In the near injector region, because of the sudden expansion, a low pressure recirculation zone is formed. At the rear stagnation point of the recirculation region, the highest pressure is achieved. The position of this rear stagnation point is determined by the interaction between combustion reactions and turbulence flow. Before this stagnation point, the reaction flow is dominated by the turbulence flow of the propellants and influenced by the geometries of the injector and chamber. Near the injector, where turbulence is intense and reaction rate is low, the pressure achieved in the recirculation area is manipulated by the turbulence flow field. Beyond the stagnation point, the reaction flow is dominated by the combustion reactions. As the reactions release heat, the combustion reaction rates climb, the temperature of the reaction flow rises and the speed of the flow increases. With the acceleration of the reaction flow, the

pressure gradually drops. When the combustion approximates the equilibrium condition, the heat release rate decreases, the acceleration of flow reduces and the descending of the pressure slows. Compared with GRI 3.0, REDRAM predicts a much lower pressure, theoretically because of incomplete burning. During the combustion process at the millisecond order, the propellants' chemical energy is converted to thermal energy by chemical reactions, which are described by mechanisms. The comparison between results of REDRAM and GRI 3.0 expresses that the REDRAM mechanism underpredicts the scale of oxygen conversion and the resultant heat generated and pressure. The high residual oxygen fraction indicates a non-equilibrium output, which may account for the REDRAM mechanism's lower heat flux and pressure compared with those of GRI 3.0.

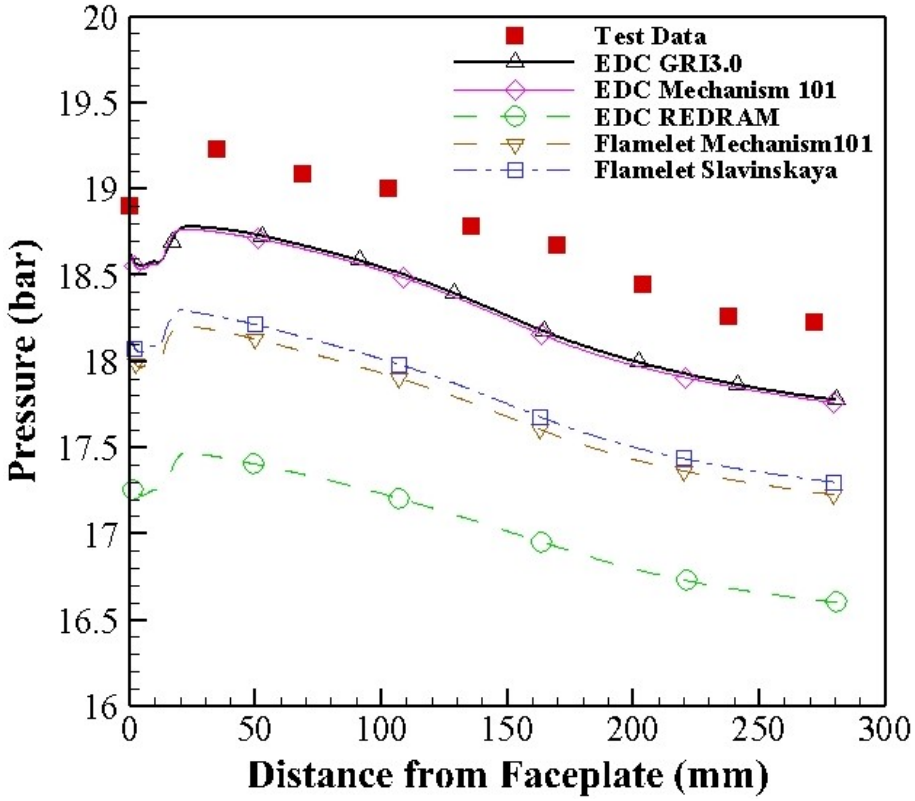

Figure 5.3 Pressure distribution in the chamber

To understand the differences regarding pressure between the mechanisms, the CFD simulation results of the test case were compared with the CEA calculation. Table 5.1 gives the simulation results of the residual oxygen at the chamber outlet. The CEA calculates a 1D flow with adiabatic walls and homogenous mixing. The table shows that REDRAM calculates a higher oxygen mass at the chamber outlet, which implies an incomplete combustion resulting in a lower chamber pressure. With GRI 3.0, the table shows that the oxygen fraction at the chamber outlet is approximately 3.3%, which is closer to the CEA results (0.4%) compared with that of REDRAM. This oxygen fraction implies a near-complete combustion, which leads to a higher chamber pressure than predicted with REDRAM. Applied to the EDC model, GRI 3.0 calculates lower residual oxygen fractions than does REDRAM, perhaps as a result of the differences in reactions quantities and the Arrhenius parameters. While GRI 3.0 encompasses 325, the REDRAM model contains only 34 reactions, which may account for its comparably

higher residual fractions. Regarding the parameters, in REDRAM they are derived from RAMEC/GRI 1.2 [87,101]. The REDRAM mechanism is reduced from the RAMEC, which comprises 38 species and 190 reactions, and represents an improvement over the core CH_4/O_2 mechanism from GRI 1.2 with its 32 species and 174 reactions. The GRI 1.2 rate coefficients were updated and integrated in the formation of GRI 2.11, which gradually evolved into GRI 3.0 with its improved and optimized rate coefficients compared with those of REDRAM. In this study, these updates may partially account for the differences in the concentrations of residual oxygen between REDRAM and GRI 3.0.

Table 5.1 Mass fraction of the residual oxygen at outlet with GRI 3.0 and REDRAM

GRI 3.0	REDRAM	CEA
3.3%	8.6%	0.4%

5.4 Species Distribution

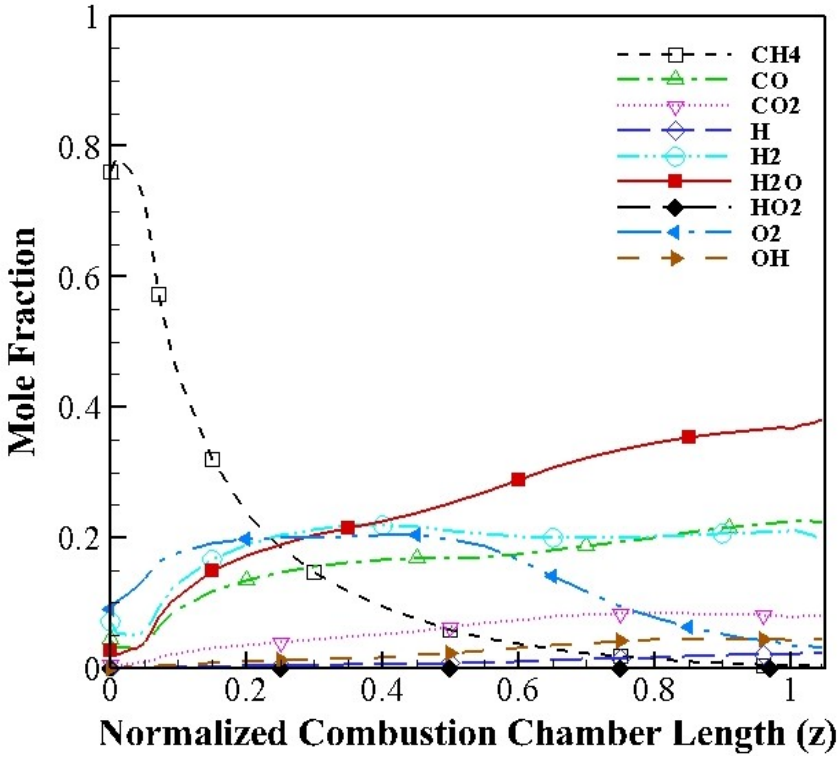

Figure 5.4 Species fractions in the simulation result of flamelet Slavinskaya

The mole fraction results shown in Chapter 5.4 have been area-averaged at different cross-sections along the chamber length. Figure 5.4 indicates that at z=0, two propellants, methane and oxygen are injected through the pipes. Here the main components of the gas, such as H_2, CO and H_2O, accumulate in the recirculation region near the tip, where the turbulence is enhanced because of the velocity difference between the two propellants. This is detailed in the discussion of the following contours of different radicals. The flamelet-Slavinskaya and flamelet-Mechanism 101 both predict the primary tracks of the radicals, while they still have differences with the EDC

results.

Several studies have implemented the Slavinskaya mechanism in the flamelet model [97], and it is shown that the transport properties largely influence the results. With the same transport properties, the flamelet results show a negligible difference with different mechanisms. The differences between the flamelet-Slavinskaya and flamelet-Mechanism 101 are minor compared with those between EDC-Mechanism 101 and EDC-REDRAM. Attempts have been made to implement the Slavinskaya mechanism with EDC model; however, this implementation is less stable than that of other mechanisms, presumably because of this mechanism's stiffness, as it has improved the reaction coefficients.

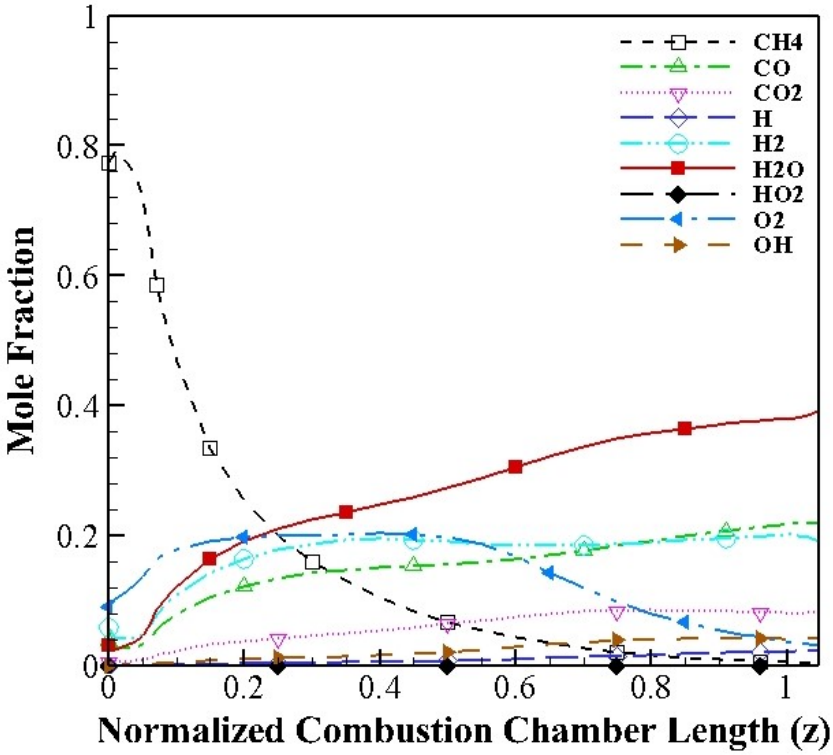

Figure 5.5 Species fractions in the simulation results of flamelet Mechanism 101

Figure 5.5 demonstrates that the CH_4 fraction drops in the region within $0<z<0.3$, and then gradually declines. Because of the recirculation of CH_4, the O_2 fraction increases within $0<z<0.15$, staying constant between $0.2<z<0.6$, before steadily decreasing to the end of the chamber. Most of other species fractions rise, after that they slowly remain stable. A comparison between the flamelet-Mechanism 101 and EDC-Mechanism 101 indicates the differences between the TCI models. As shown in Chapter 3, flamelet calculates the mean enthalpy as well as the mean mixture fraction and its variance, while EDC solves every species' transport equation. The chemical reactions are included under one-dimensional laminar flamelet structures, and tabulated to establish a flamelet library. The flamelet is then included via transferring data. The main differences between the results of the flamelet model and the EDC model are significant in species CO, CO_2, H and H_2. It is assumed that the flamelet model predicts higher intermediate species in the front part of the chamber and in the recirculation region of the methane, because the flamelet model predicts an earlier equilibrium condition than

does the EDC model, as illustrated and examined in the following contours.

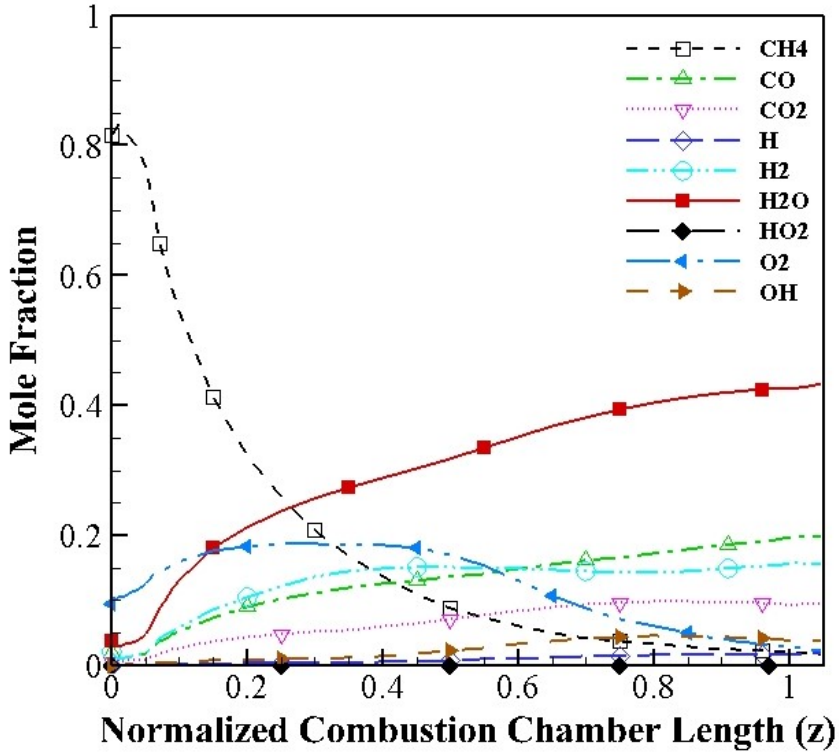

Figure 5.6 Species fractions in the simulation results of EDC Mechanism 101

Figure 5.6 demonstrates that as a reduced mechanism developed from GRI 3.0, Mechanism 101 shows the same track of species fractions with GRI 3.0, which indicates that compared with GRI 3.0, Mechanism 101 retains a smaller number of chemical species and reactions required to account for the essential features of the combustion process in this rocket chamber. At 2,200 K, with GRI 3.0 the methane oxidation primarily goes through the reaction path $CH_4 \rightarrow CH_3 \rightarrow CH_3O \rightarrow CH_2O \rightarrow HCO \rightarrow CO \rightarrow CO_2$, whose pathway is involved both in Mechanism 101 and REDRAM. Under 1,500 K, in this oxidation process another C_2 pathway appears:

$CH_4 \rightarrow CH_3 \rightarrow C_2H_6 \rightarrow C_2H_5 \rightarrow C_2H_4 \rightarrow C_2H_3 \rightarrow C_2H_2 \rightarrow CH_2 \rightarrow CH \rightarrow CO \rightarrow CO_2$,

while REDRAM's C2 pathway is:

$CH_4 \rightarrow CH_3 \rightarrow C_2H_5 \rightarrow C_2H_4 \rightarrow C_2H_3 \rightarrow CH_2O \rightarrow HCO \rightarrow CO \rightarrow CO_2$.

In REDRAM, the species C_2H_6 and C_2H_2 are retained but not involved in the C_2 reaction pathway. The differences between reactions of Mechanism 101 and REDRAM are detailed in the examination of the following contours of species. For instance, the reactions $OH+H_2<=>H+H_2O$ and $2OH<=>O+H_2O$ both have effects on the OH concentration. Mechanism 101 contains $OH+H_2<=>H+H_2O$ instead of $2OH<=>O+H_2O$, while in contrast REDRAM encompasses $2OH<=>O+H_2O$ instead of $OH+H_2<=>H+H_2O$. These reaction differences partially affect the mechanisms' prediction of species fractions, and detailed differences are shown and analyzed in the consideration of the following contours.

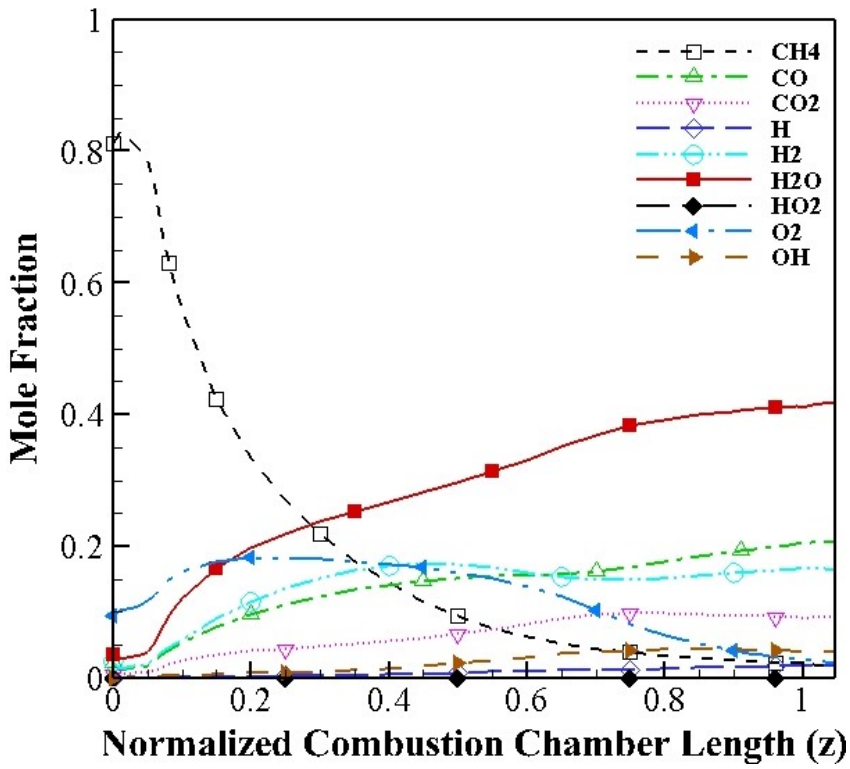

Figure 5.7 Species fractions in the simulation results of EDC GRI 3.0

Figure 5.7 depicts that near the inlet, where the two main components are methane and oxygen, the mole fraction of oxygen sharply increases because of the recirculation of the methane. Under attack by active radicals OH, H and O, CH_4 converts to CH_3, which is then oxidized to CH_2O by the O radical. Then CH_2O reacts with radicals such as O, O_2, H, OH, HO_2, and CH_3, or it decomposes to form HCO. After that, the production of CO is produced from the reactions between HCO and O, H, OH, and CH_3 radicals. In turn, CO_2 is produced when CO reacts with the O, O_2, OH, HO_2 and HCO radicals. In GRI 3.0, a part of CH_3 converts to CH_2(s), while in Mechanism 101, Slavinskaya and REDRAM, CH_2(s) has been removed. The investigation of soot formation requires more complicated mechanisms than GRI 3.0, such as the mechanisms from [102] and [103]. In their research, the formation of polycyclic aromatic hydrocarbons is a key issue, which requires a series of species including benzene (A1), naphthalene (A2), phenanthrene (A3) and pyrene (A4). Further studies to expand the current mechanism Slavinskaya are under development.

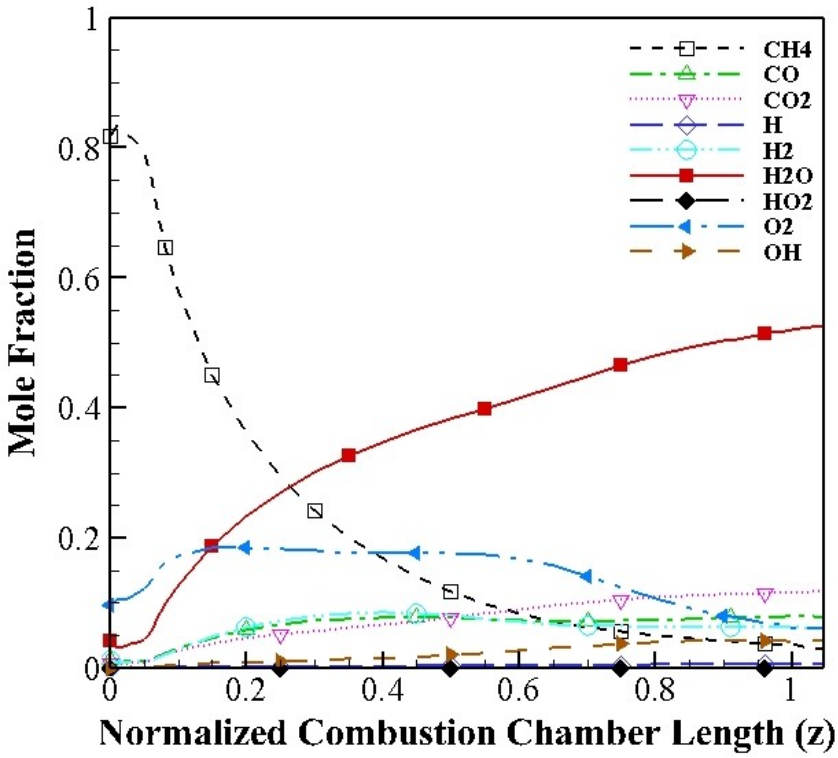

Figure 5.8 Species fractions in the simulation results of EDC REDRAM

In Figure 5.8, comparisons between the mole fractions with REDRAM and those with Mechanism 101 and GRI 3.0 illustrate that REDRAM predicts a much higher residual O_2 fraction than the others, presumably because of the three reactions' different coefficients between REDRAM and GRI 3.0. Compared with it, REDRAM predicts lower H radical fractions because of the higher consumption of H by O_2 through the reactions $H+O_2+M<=>HO_2+M$ and $H+O_2<=>O+OH$. REDRAM also predicts higher H_2O and lower H_2 fractions than do GRI 3.0 and Mechanism 101, due to the absence of a conversion from H_2O to H_2 through the reaction $OH+H_2<=>H+H_2O$. With higher H_2O and O_2 fractions, the REDRAM simulation predicts a much higher reaction rate of $H+O_2+M<=>HO_2+M$ than that in Mechanism 101 and GRI 3.0. Correspondingly, the HO_2 fraction with REDRAM is much higher than those predicted with Mechanism 101 and GRI 3.0. The higher amounts of HO_2 radicals in REDRAM further promote the conversion of CO to CO_2. As a result, REDRAM predicts lower CO and higher CO_2 fractions than do GRI 3.0 and Mechanism 101. In addition to the differences between the reactions in REDRAM and those in GRI 3.0, different reaction coefficients also largely contribute to the fraction differences between them, as the coefficients in GRI 3.0 have been modified from those of REDRAM. These coefficients are also under development in other studies [103].

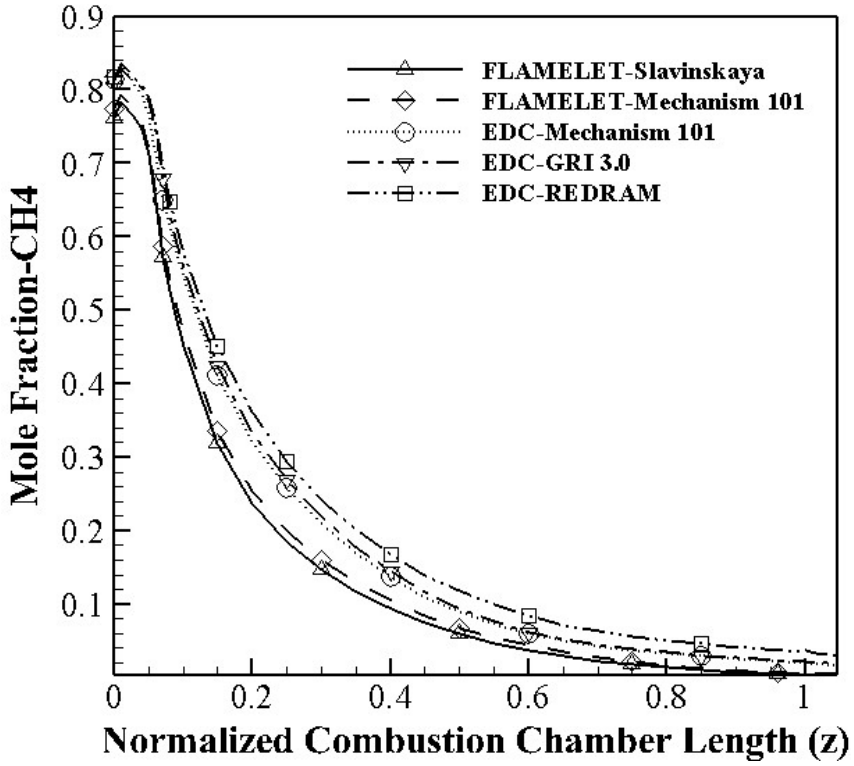

Figure 5.9 CH_4 mole fractions of different models

Figure 5.9 shows that the simulation results with the flamelet and EDC models have observable differences. Starting from approximately 0.8 on the Mole Fraction Axial, all results show that the mole fraction of CH_4 drops significantly along the chamber axis to 0.2 within the region $0<z<0.3$. Beyond that region, the decline then slows along the chamber axis to $z=0.6$, after which the rate of decline flattens at $z=1$ on the chamber axis. Comparing the two models, the flamelet results approach zero much more closely than the results of the EDC model. The different results are presumed to be caused by conditions near the nozzle region, where the temperature is higher than 3,000 K; above this temperature, the methane should have decomposed. As the results with the flamelet model are closer to the equilibrium condition, more CH_4 is consumed. In contrast with the EDC model, the decomposition of CH_4 appears unfinished. Within the flamelet model, the difference between different mechanisms is negligible. Within the EDC model, the difference between Mechanism101 and GRI 3.0 is undetectable, whereas the difference between EDC Mechanism101 and EDC REDRAM is minor and may come from two aspects. Firstly, both in REDRAM and Mechanism 101 CH_4 can convert through the reactions $HO_2+CH_3<=>O_2+CH_4$ and $H+CH_4<=>CH_3+H_2$. In these reactions, H radicals promote the consumption of CH_4 while HO_2 radicals inhibit. As shown in the following fraction results of HO_2 and H radicals, REDRAM predicts higher HO_2 and lower H fractions than those of Mechanism 101. Correspondingly, the predicted amounts of HO_2 and H radicals affect these two reactions, resulting in different CH_4 fractions. Secondly, the following images display observable differences between the flow stream lines of Mechanism101 and EDC REDRAM; this can be explained by the chemical reactions as well as the interaction of turbulence and combustion.

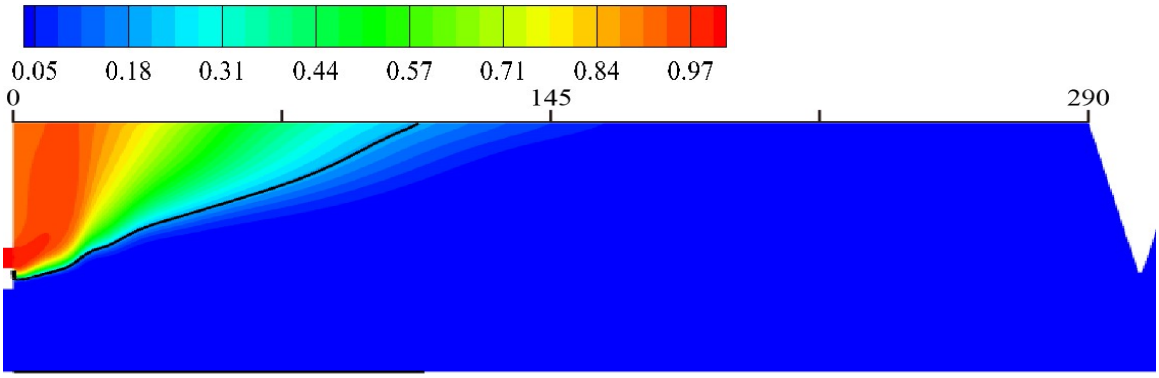

(a) EDC GRI 3.0

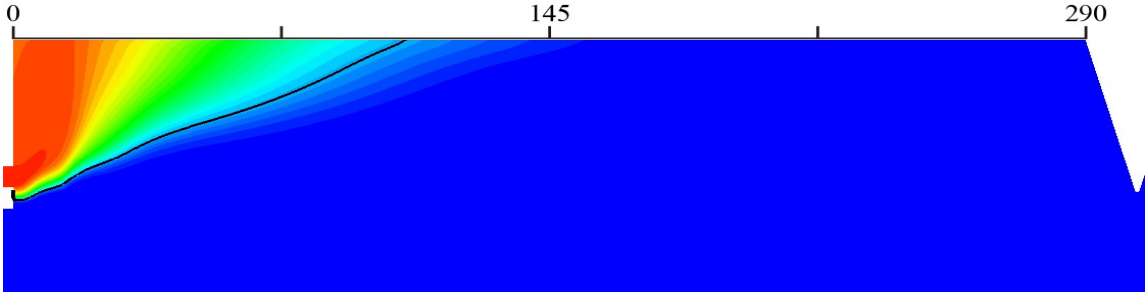

(b) EDC Mechanism 101

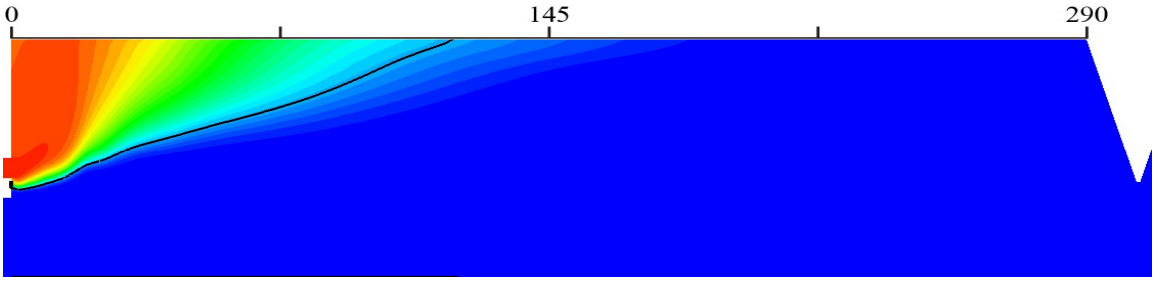

(c) EDC REDRAM

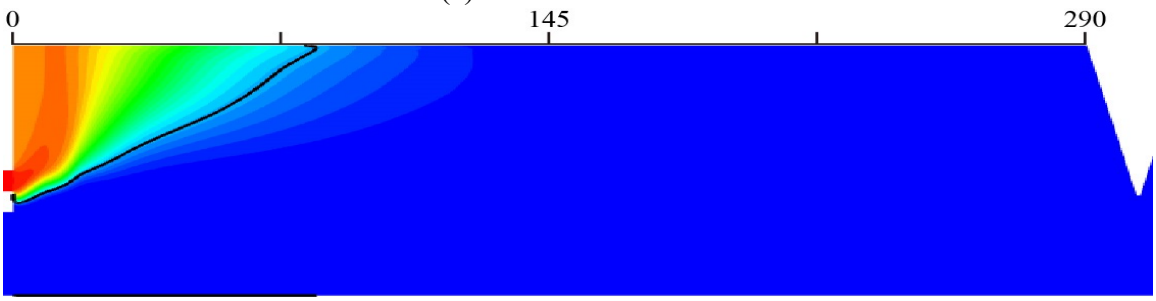

(d) FLAMELET Mechanism-101

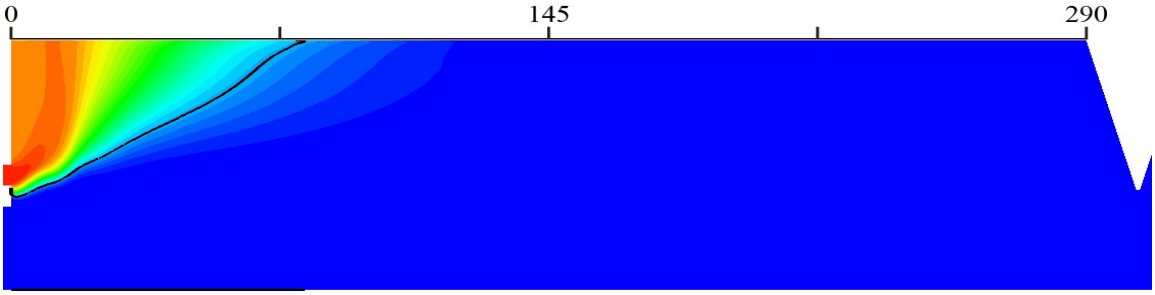

(e) FLAMELET Slavinskaya

Figure 5.10 CH_4 mole fraction contours at symmetry of different models with CH_4=0.2 line

The contour of the fraction of CH_4 in Figure 5.10 illustrates that once leaving the injectors, much of the methane accumulates in the recirculation region near the injector. As the methane is moved closer to the hot gas region, it decomposes into intermediate products as shown in the mole fraction results. In a comparison between the EDC and flamelet models, the EDC model accounts for the interaction between the chemical reactions and the turbulence flow, and methane's chemical reactions are finite rated, while the flamelet model assumes that the chemical reactions are infinitely fast. As a result, the methane is consumed at a lower rate under the EDC model than that under the flamelet model; consequently, the EDC model's region of highly concentrated methane is larger than that of the flamelet model.

Simulations conducted on the chambers in test cases [70] employing the flamelet model with the mechanisms of Slavinskaya and Mechanism 101 reveal negligible differences in performance. Just as with the mole fraction of methane, the results of Mechanism101 in simulations under the EDC model substantially agree with those of GRI 3.0. Among the three mechanisms, REDRAM has a higher concentration of methane nearby the injectors compared with the other models presumably because REDRAM underestimates the decomposition rate of methane near the recirculation region. With this estimated lower decomposition rate, the identical inlet mass flow rate as in the other mechanisms results in an elevated mole fraction of methane.

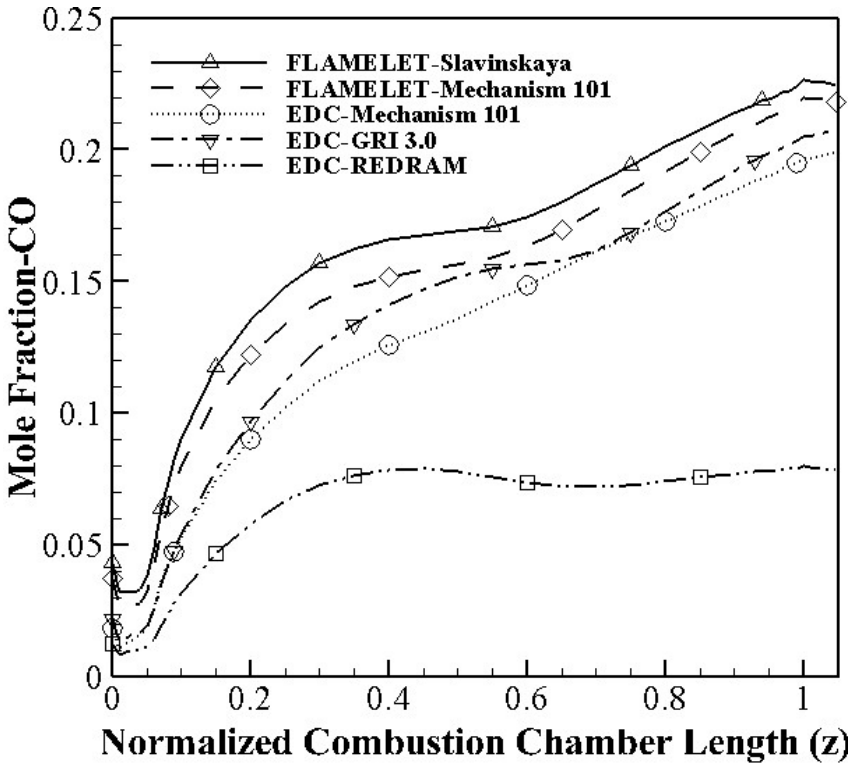

Figure 5.11 CO mole fractions of different models

As can be seen in Figure 5.11, the reactions in all simulations other than those in EDC-REDRAM result in an increase in the mole fraction of CO, as tracked on the chamber axis. It is presumed that the mole fraction of CO is largely influenced by the reactions $HCO+O_2<=>HO_2+CO$, $HCO+H_2O<=>H+CO+H_2O$ and $OH+CO<=>H+CO_2$. Starting from the z=0, the mole fraction of CO rises with the increase of OH fraction.

As the reactions progress, the mole fraction of OH rises, thus accelerating the transformation of CO to CO_2, and correspondingly increasing the consumption rate of CO. Accordingly, the rate of the increasing mole fraction of CO slows. Where 0.4<z, the influence of OH concentration on the mole fraction of CO is greater in the flamelet model than in the EDC model. This is presumed to be why the results form a plateau within the 0.4<z<0.6. Close to the nozzle most of the chemical reactions have been completed, and the mole fractions of H, CO_2 and OH increase accordingly.

Figure 5.11 shows that in contrast with the other four simulations, the EDC-REDRAM tracks differently along the chamber axis. The mole fraction of CO forms a plateau in the region beyond z=0.6, theoretically because the reaction HO_2+CO<=>OH+CO_2 consumes a portion of the CO in addition to the consumption of CO by the OH+CO<=>H+CO_2 reaction. The EDC-REDRAM's high mole fraction of HO_2 accelerates the forward reaction rate, and correspondingly the mole fraction of CO decreases while the mole fraction of CO_2 increases, which explains why the EDC-REDRAM's mole fraction of CO is much lower and CO_2 is much higher than that seen in the other simulation results.

In Figure 5.12, the intermediate product CO has a low mole fraction in the region where the methane recirculates. The continuation of the reactions increases the mole fraction, and the level of CO condensation near the wall is much higher compared with the level close to the center of the hot gas. This difference assumedly results from the concentration of the radical OH, which influences the forward reaction rate of OH+CO<=>H+CO_2. The OH concentration and the forward reaction rate are strong and fast, respectively, near the center of the hot gas. Close to the wall, on the contrary, these attributes are weaker and slower. Consequently the CO mole fraction near the wall is higher than that near the center. Compared with the EDC model, the flamelet model has a much larger high CO concentration region within the recirculation region; one possible cause is that the flamelet model employs the hypothesis that the chemical reactions are infinitely fast and that the mole fraction of CO is directly read from the table, whose results are at equilibrium conditions. In contrast, the EDC model assumes that the formation process of CO goes through the pathway CH_4→ CH_3 → CH_3O → CH_2O → HCO → CO. These assumptions may account for the much larger high concentration region of CO in the flamelet model compared with that in the EDC model.

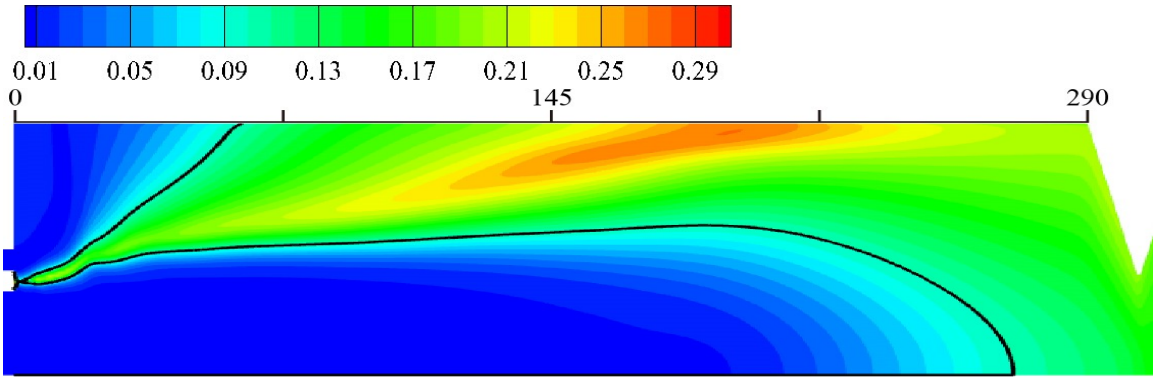

(a) EDC GRI 3.0

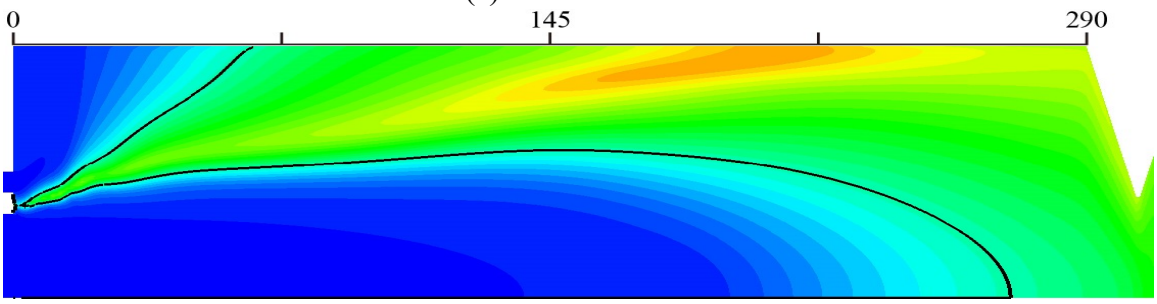

(b) EDC Mechanism 101

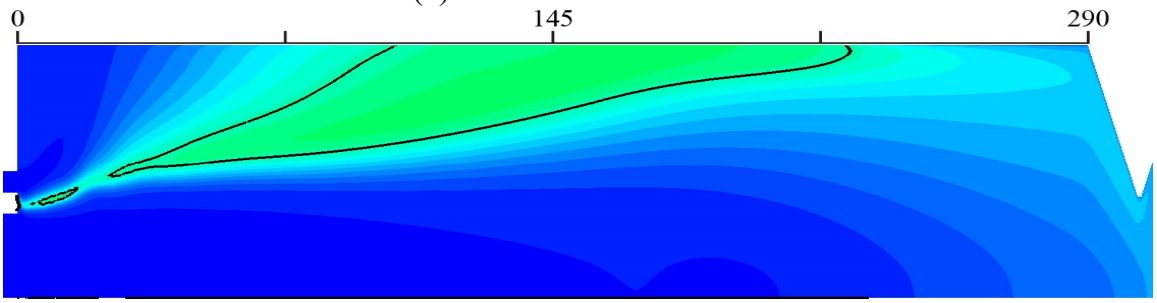

(c) EDC REDRAM

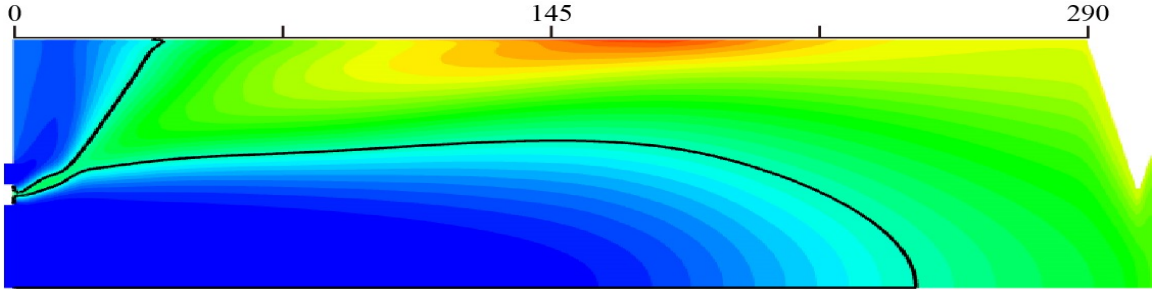

(d) FLAMELET Mechanism-101

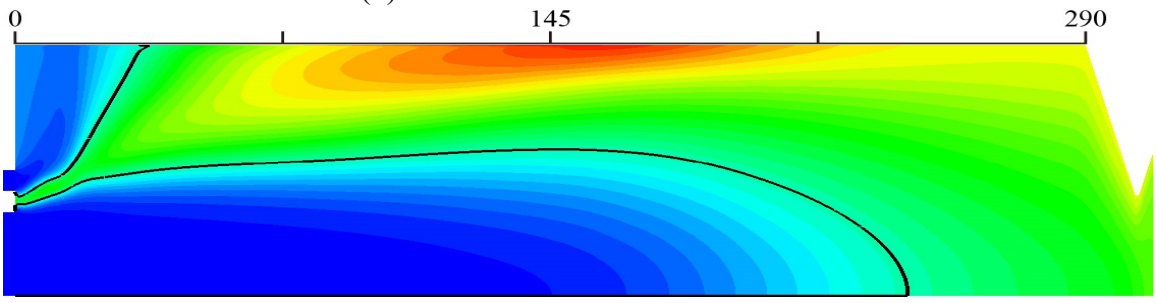

(e) FLAMELET Slavinskaya

Figure 5.12 CO mole fraction contours at symmetry of different models with CO=0.1 line

As shown in Figure 5.12, employing the EDC model several differences in the recirculation region and near the center of the hot gas exist among the GRI 3.0, Mechanism101 and REDRAM mechanisms, whose different predictions for the concentrations of O_2, HO_2 and H_2O can explain these variations. A supposition is that O_2 affects the mole fraction of CO via the reactions $HCO+O_2<=>HO_2+CO$ and $O_2+CH_2O<=>HO_2+HCO$; in turn, the HCO radicals participate in the reaction $HCO+O_2<=>HO_2+CO$ again. As shown in the following fraction results, REDRAM predicts higher levels of O_2, which increase the reaction rates of $CH_3+O_2<=>OH+CH_2O$, $H+O_2<=>O+OH$, $HCO+O_2<=>HO_2+CO$ and $H+O_2+M<=>HO_2+M$, leading to higher formations of OH and HO_2 radicals compared with the other results. A high concentration of HO_2 also accelerates the consumption of CO through the reaction $HO_2+CO<=>OH+CO_2$, with the result that EDC-REDRAM presages a much lower mole fraction of CO than predicted in the other simulation results. From the following contours of the fraction of HO_2 in the EDC-REDRAM model, HO_2 has a much higher mole fraction than in other results, which greatly reduces the mole fraction of the corresponding CO compared with the other models and mechanisms. In addition to the effects from O_2 and HO_2, H_2O also favors the generation of CO radicals through the reaction $H+O_2+M<=>HO_2+M$. EDC-REDRAM predicts a much high mole fraction of H_2O as shown in the following images of the fractions, which partially explain the low CO concentration in REDRAM. H_2O participates in this reaction as a very efficient partner, leading to HO_2 formation that favors the CO consumption in the aforementioned way.

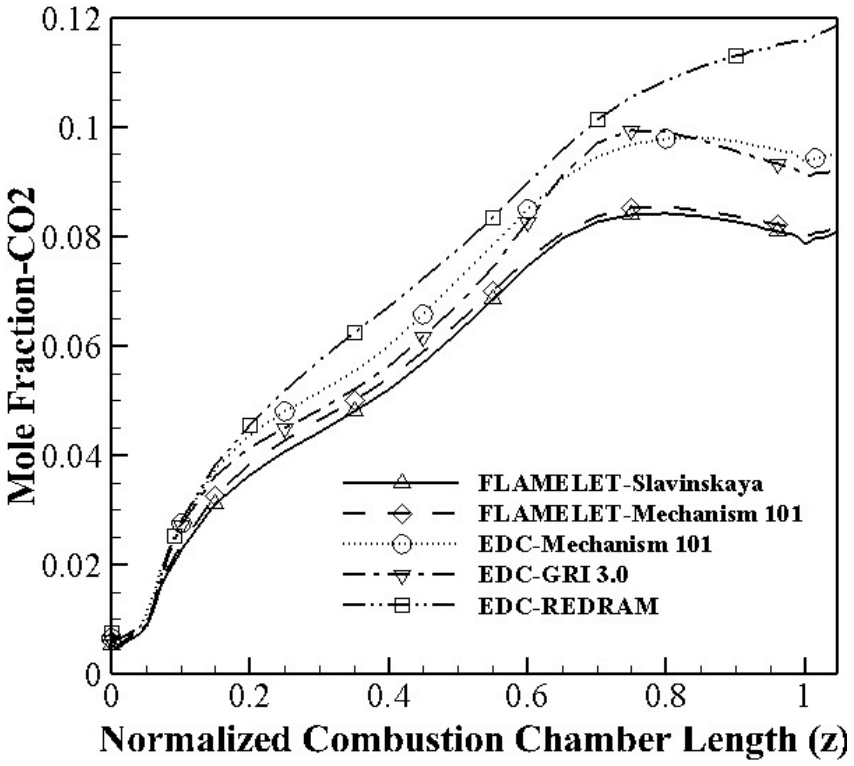

Figure 5.13 CO_2 mole fractions of different models

As shown in Figure 5.13, mainly throughout the pathways $CH_4 \rightarrow CH_3 \rightarrow CH_3O \rightarrow CH_2O \rightarrow HCO \rightarrow CO \rightarrow CO_2$, CO_2 gradually increases in the three EDC and two

flamelet results, with its concentration greater in the EDC models, presumably resulting from the calculated interaction between the turbulence and the combustion. In the near-injector region, the chemical reactions form an expanding shear layer which at a certain downstream position reaches the wall. As can be deduced from the pressure profiles most of the heat release has taken place within the first 150 mm. Hence, further downstream any heat release driven acceleration of the gases is much smaller. Furthermore, only within the first 150 mm will heat release in the reacting shear layer further the generation of turbulence. This is presumed to be the explanation for the gentle increment in the mole fraction of CO_2 in the region of $0.2<z<0.7$. In the region of $0.7<z<0.9$, the turbulence effects are weak, but the temperature increases to a sufficiently high degree, so the mole fraction of the CO_2 continues to increase in EDC REDRAM.

The results of the three EDC mechanisms in Figure 5.14 illustrate that the velocity difference between propellants generates turbulence, which strengthens the mixture and quickens the reactions. Correspondingly, the mole fraction of the final product CO_2 near the tip between the two injectors rises. The mole fractions of CO_2 in the flamelet results near the tip are much lower than those near the chamber, and at the same time the EDC results have a much higher increment near the tip compared with the flamelet results. Presumably this is caused by the EDC model's greater inclusion of the interaction between the turbulence and the chemical reactions than the flamelet model encompasses. All five simulation results demonstrate that as the reactions approach equilibrium, the mole fraction of CO_2 gradually increases with the highest result occurring in the rear of the central region of the hot gas. In the convergent part of the nozzle, thermal energy is converted to kinetic energy with correlated decreases in both the temperature and the mole fraction of CO_2. Among the EDC results, the EDC-REDRAM shows a much higher CO_2 concentration compared with that of the other mechanisms presumably because of the high concentration of HO_2 in the reaction $HO_2+CO<=>OH+CO_2$. With different reactions and Arrhenius parameters, much higher O_2 and HO_2 concentrations are predicted in the EDC-REDRAM model than in the other mechanisms. EDC-REDRAM's overestimation of the concentration of other species and reactions including HO_2 with different Arrhenius parameters further over predicts the mole fraction of HO_2. Similarly, the reaction $HO_2+CO<=>OH+CO_2$ over predicts the CO_2 concentration. The high residual concentration of O_2 is presumably the cause of the continuously increasing mole fraction of CO_2 through the nozzle.

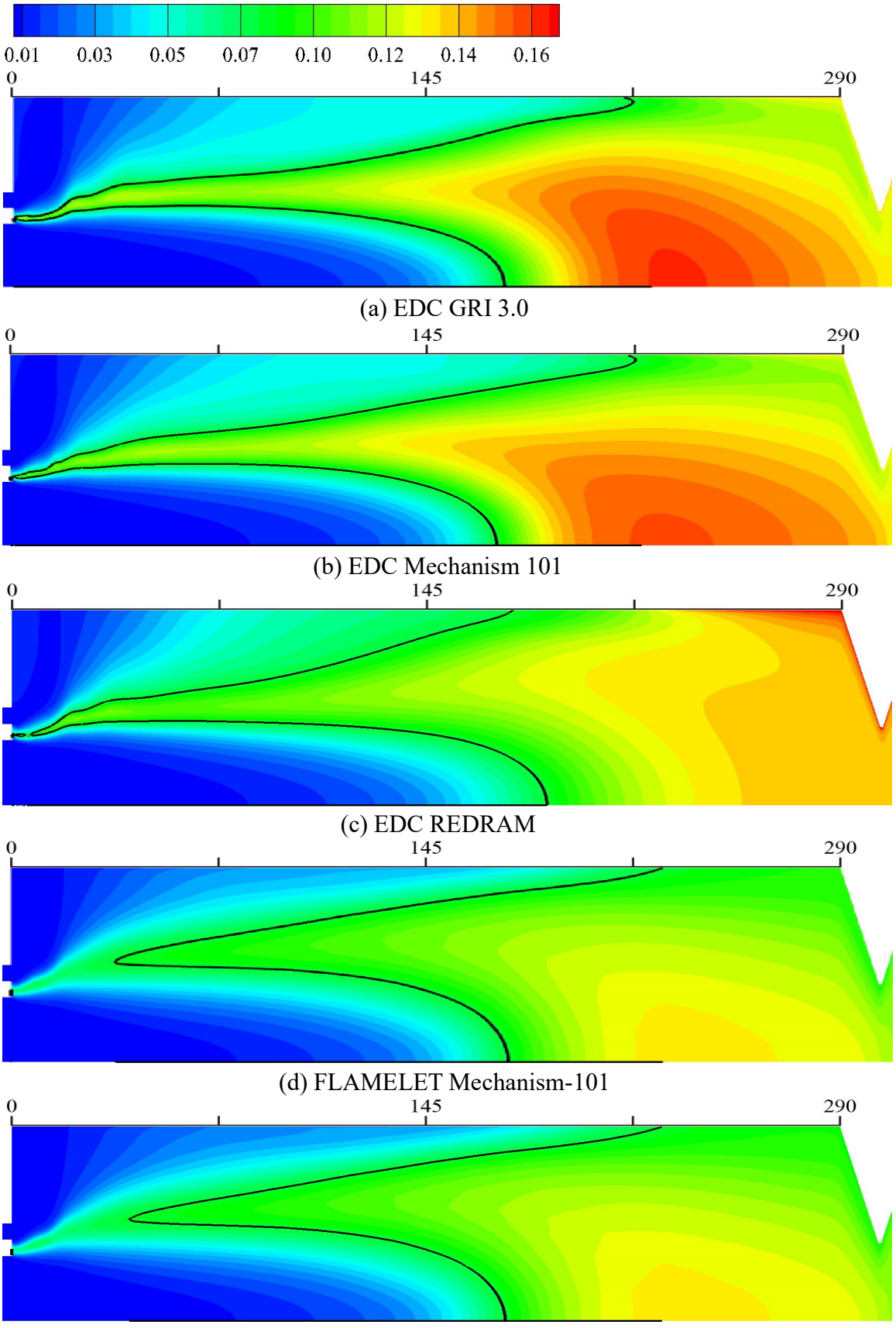

(a) EDC GRI 3.0

(b) EDC Mechanism 101

(c) EDC REDRAM

(d) FLAMELET Mechanism-101

(e) FLAMELET Slavinskaya

Figure 5.14 CO_2 mole fraction contours at symmetry of different models with CO_2=0.08 line

In Figure 5.14, comparing the EDC-Mechanism101 with the flamelet-Mechanism101 clearly shows that in the rear part of the chamber, the EDC simulation results have a much higher CO_2 concentration than seen in the flamelet results, presumably because the EDC model predicts a much higher temperature than does the flamelet model and a higher mole fraction of CO_2. As shown in Figure 4.2, the CO_2 abound within the high temperature region. This proves that the higher the temperature, the more the final product of CO_2 is produced. In addition, the CFD simulation results shown here correspond to the PSR results detailed in Table 4.2. During the combustion process, most of the energy is released in the form of heat in the reaction OH+CO<=>H+CO_2; the high mole fraction of the CO_2 in this reaction leads EDC's temperature to be higher than that in the flamelet model, which demonstrates the connection between the temperature and CO_2 fractions. Comparisons between the CO_2 fractions of REDRAM and GRI 3.0 illustrate that REDRAM predicts higher CO_2 fractions, presumably from the effect of H_2O fractions through the reactions H+O_2+M<=>HO_2+M and HO_2+CO<=>OH+CO_2. The reaction rate of H+O_2+M<=>HO_2+M is increased due to high H_2O concentrations in REDRAM, leading to HO_2 formation. In turn, the HO_2 radicals favor the conversion through the reaction HO_2+CO<=>OH+CO_2.

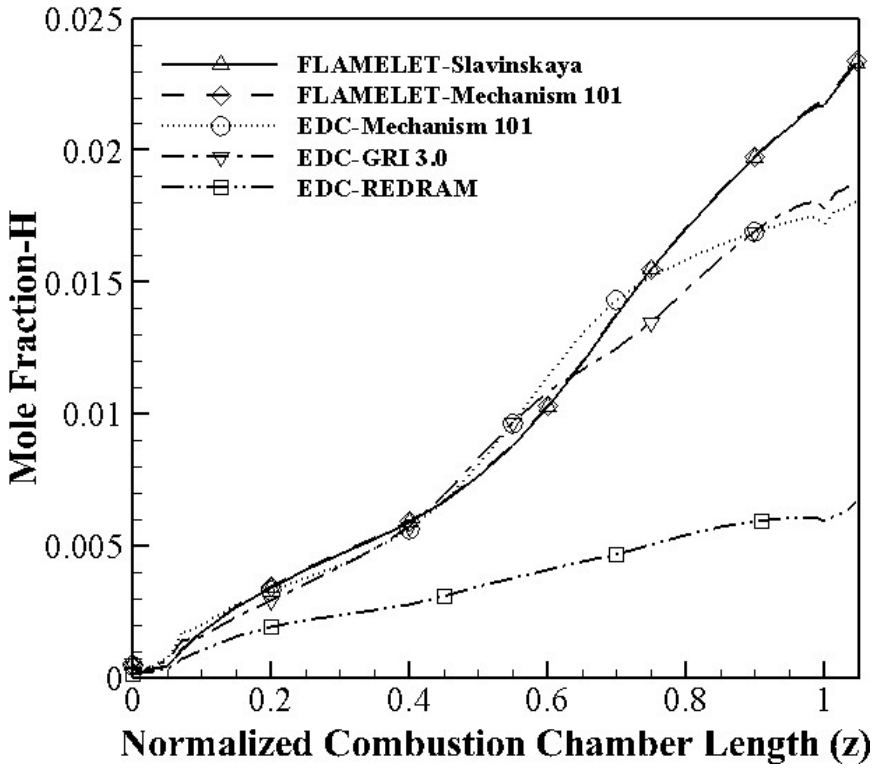

Figure 5.15 H mole fractions of different models

Typically small radicals attack the methane, which initiates its combustion, for instance, in a fuel-rich flame, the H atoms are a factor in the reaction H+CH_4<=>CH_3+H_2. Furthermore, H atoms are active not only throughout the pathway CH_2O→HCO→CO→CO_2, but also in the C_2 pathways. For example, each stage of the pathway C_2H_6→C_2H_5→C_2H_4→C_2H_3→C_2H_2 requires the participation of H atoms, which play indispensable roles in more than 10 reactions. Moreover, the generation of H starts the development of a pool of radicals in the reaction H+O_2<=>O+OH. The

establishment of O and OH radicals will stimulate other reactions.

Figure 5.15 presents that with the exception of EDC-REDRAM, all simulations result in an increase of the mole fraction of H atoms similar to that of the CO fraction. It is conjectured that this exception derives from both the reactions and the Arrhenius parameters based on the following:

1) Higher O_2 fractions with REDRAM increase the reaction rates of reactions $H+O_2+M<=>HO_2+M$ and $H+O_2<=>O+OH$, leading to higher H consumption compared with that of other mechanisms. Because of the different reaction rates of REDRAM and GRI 3.0, which are shown in the following discussions, REDRAM predicts higher O_2 fractions, resulting in higher H radical consumption and lower H radical fractions through these two reactions. The high H_2O concentration may also favor the consumption of H radicals through the reaction $H+CH_2O(+M)<=>CH_3O(+M)$, as in this reaction the third body efficiency of H_2O is 6, which indicates the amount of H_2O radicals largely determines this reaction rate. Furthermore, the REDRAM mechanism encompasses 12 reactions that include the H atom, while 27 such reactions are contained in Mechanism101. The reactions in REDRAM seem insufficient to predict the H radical concentration.

2) The Arrhenius parameters in REDRAM are distinguished from those of Mechanism101, which are the updated version of REDRAM. For instance, in REDRAM the pre-exponential factors of reactions $H+O_2+M<=>HO_2+M$ and $H+O_2<=>O+OH$ are 2.6E+19 and 8.3E+13, while they are 2.8E+18 and 2.65E+16 in Mechanism 101 and GRI 3.0. These differences indicate that the conversion of O_2 to HO_2 would be much faster than it would be in Mechanism 101, while the conversion of O_2 to O and OH would be much slower. This indication corresponds to the higher HO_2 fractions in REDRAM.

As with the CO_2 results, Figures 5.16 show a similar difference between the EDC model and the flamelet model, leading to a conjecture parallel to the CO_2 assumption in the earlier discussion. For the three EDC models of the H atom, it is reasoned that the velocity difference between the two propellants generates the shear force that enhances the turbulence, which accelerates the chemical reactions in this region, while the flamelet model of the H atom does not capture these phenomena. Similar to the heat flux's difference in Chapter 5.2, the difference between H mole fractions of flamelet model and EDC model may come from the PDF method, the flamelet model and the transport equations. The flamelet model adopts the mixture fraction and scalar dissipation to predict the intermediate species with an overall transport property, while the EDC model calculate reactions in fine scales, respecting time scales as determined by the Arrhenius law with transport equations for each species. The differences between the mole fractions of species between the flamelet and EDC models expose the consequences of their different assumptions.

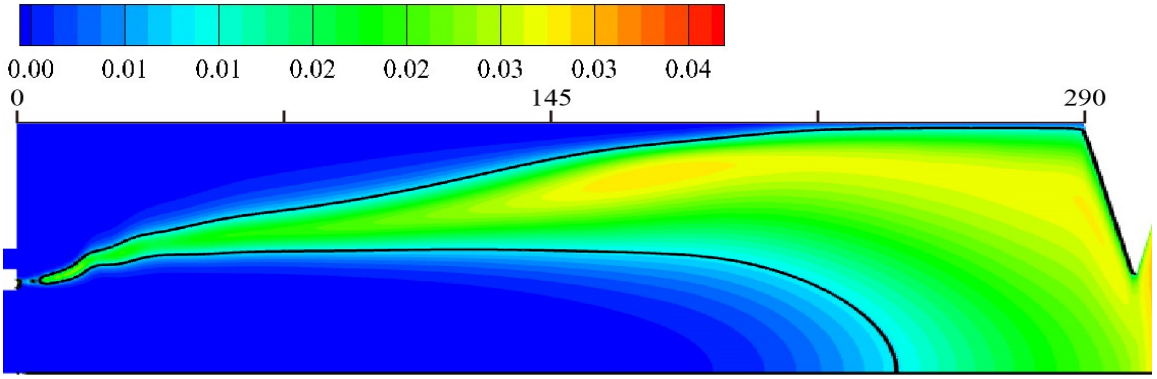

(a) EDC GRI 3.0

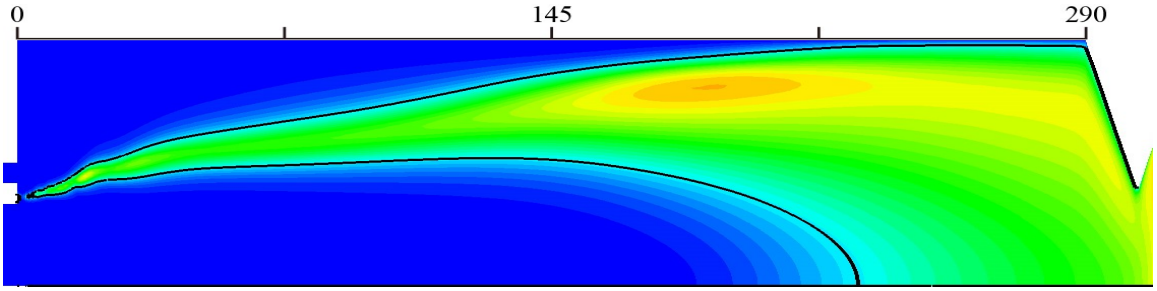

(b) EDC Mechanism 101

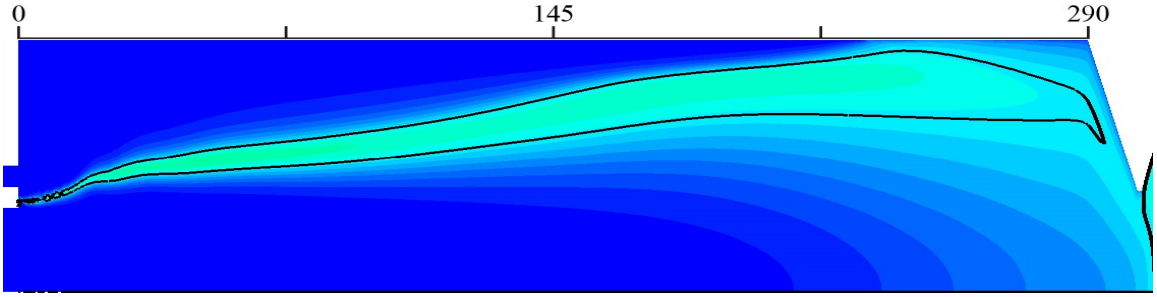

(c) EDC REDRAM

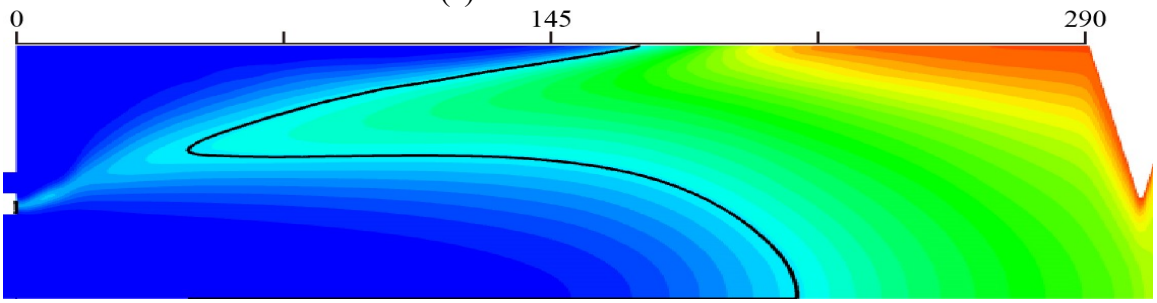

(d) FLAMELET Mechanism-101

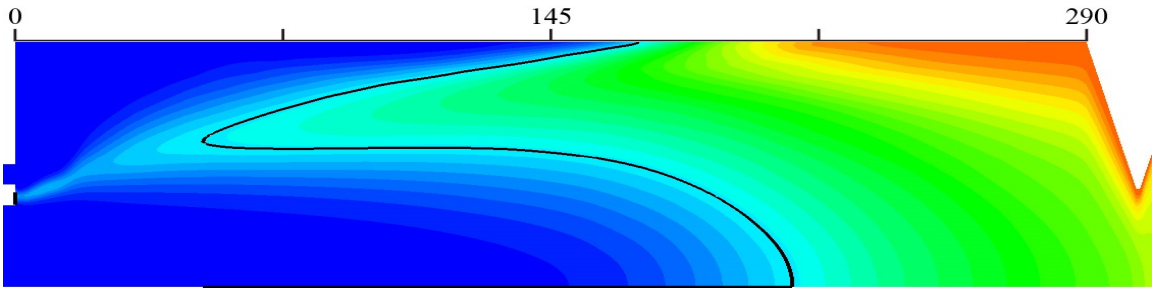

(e) FLAMELET Slavinskaya

Figure 5.16 H mole fraction contours at symmetry of different models with H=0.01 line

In Figure 5.16, compared with the flamelet results, the EDC results show that the concentration of H atoms is lower in the region near the rear part of the chamber wall. Furthermore the EDC results illustrate that the mole fraction of H atom close to the wall is around 0.02, gradually increasing to 0.035 as it nears the center region. Interestingly, it returns to about 0.02 in the center region, which may be caused by the effects from both the temperature and O_2 concentration. Near the rear part of the chamber wall, the heat flux through it decreases the temperature, and presumably the reaction rates are correspondingly moderate. As the gas nears the center region, the temperature increases and the rates of the reactions quicken. As the H atom approaches the hot gas region, the O_2 mole fraction rises, while the temperature's effect on the reaction rates declines. In the reactions $H+O_2+M<=>HO_2+M$, $H+2O_2<=>HO_2+O_2$, $H+O_2+H_2O<=>HO_2+H_2O$ and $H+O_2<=>O+OH$, the H atom is theoretically consumed by the O_2, and the higher O_2 concentration in the hot gas region, compared with that near the wall, may be one explanation for the decrease in the mole fraction of the H atom. Assuming the aforementioned O_2 consumption, its effect may account for the low H atom concentration in the EDC-REDRAM results. Because the O_2 residual concentration in EDC-REDRAM is higher than in the other mechanisms, the H atom's concentration in EDC-REDRAM is much lower than those in the other two EDC results, particularly in the central region where more O_2 accumulates compared with the amount measured in other mechanisms.

Figure 5.16 indicates that moving toward the wall in the EDC model, the H atom concentration in the hot gas gradually decreases, which contrasts with the incremental increase in the mole fraction of H in the flamelet model in the approach to the wall. This difference may be caused by the flamelet model capturing less of the temperature effect on the chemical reactions compared with that of the EDC model. Calculating the intermediate species with the mixture fraction in the flamelet model reduces the significance of the temperature compared with calculations in the EDC model, which considers reactions to occur within fine structures, those are treated as perfectly stirred reactors. From Figure 5.16 and Figure 5.24, it is assumed that in the flamelet results, the mole fraction of O_2 gradually decreases from the location of the hot gas to the wall, and given the reactions containing O_2 and H mentioned above, the mole fraction of H increases.

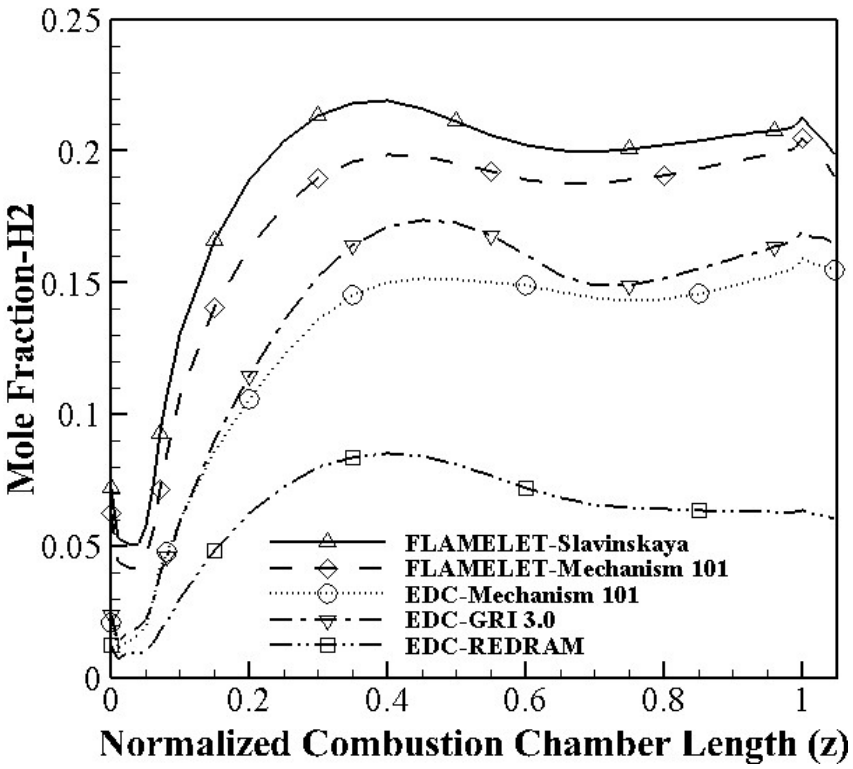

Figure 5.17 H_2 mole fractions of different models

As can be seen from the Figure 5.17 that in all simulation results, the mole fraction of the H_2 increases rapidly to the maximum value in the region between 0<z<0.4, after which it declines slightly throughout the region to z=0.7 before rising again along the chamber length in the region to z=1. Though H_2 is also an intermediate product like the H atom, their mole fraction graphs show large differences. From z=0, the H_2 mole fraction line increases sharply before going into a plateau, while the H fraction rises gradually in the region to z=0.45, and then continues its upward trajectory more steeply to z=1. The temperature may be a factor in these varying tracks: as the temperature increases in the rear chamber, a part of the H_2 radical decomposes, resulting in the plateau of the H_2 radical along the rise in temperature and the increase of the H radical. A comparison of the two results in the context of the flamelet model with the three results of the EDC model shows that the fractions of the two flamelet model results are both higher than those in the EDC models. A possible cause of this could be that the mole fraction of H_2 with the flamelet model is read from tables generated under equilibrium conditions. Consequentially, the flamelet predicts a higher H_2 fraction than does the EDC model.

Figure 5.17 depicts that in the context of the EDC model, the comparisons among Mechanism101, GRI 3.0 and REDRAM show that Mechanism101 and GRI 3.0 calculate higher fractions than REDRAM, perhaps as a result of the reactions and the Arrhenius parameters. The REDRAM model only contains four reactions including the H_2 radical, while Mechanism101 encompasses 11. Having only four reactions may account for the comparably lower fractions. For instance, REDRAM lacks the reaction $OH+H_2<=>H+H_2O$, through which H_2O converts to H_2 in Mechanism 101 and GRI 3.0. The absence of this transformation partially explains the higher H_2O and lower H_2

fractions with REDRAM compared with those of other mechanisms. The contours of the H_2 fraction illustrate that in the recirculation of methane and near the nozzle wall and the rear chamber wall, the H_2 fraction with REDRAM is much lower than that in GRI 3.0. In these regions, the H_2O fraction with REDRAM is higher than those in the other two mechanisms. Corresponding to the results in Figure 5.20, in the recirculation of methane the high H_2O concentration region with REDRAM is larger than those with GRI 3.0 and Mechanism 101. Furthermore, the H_2O fraction with REDRAM is much higher than those with GRI 3.0 and Mechanism 101. As discussed in Chapter 5.3, REDRAM's rate coefficients derive from RAMEC/GRI 1.2 and represent a further difference in addition to the number of reactions. Those rate coefficients have been upgraded to GRI 2.11, and then to GRI 3.0. The differences in coefficients between REDRAM and GRI 3.0 may be another cause of the predicted H_2 mole fractions of REDRAM and GRI 3.0.

The results in Figure 5.18 illustrate that in contrast to the H fraction's steady increase along the chamber length, the H_2 concentration increases before decreasing. When oxidation begins, near the injection plate, the H_2 fraction is low. The reactions gradually generate H_2 in the regions of methane's recirculation and the reaction, while the H_2 fraction decreases lightly as it nears the nozzle. As previously discussed, this decrease may occur because the increasing temperature hastens the decomposition of H_2. Nearing the chamber wall, the H_2 fraction apparently increases and is above the level in the hot gas region. These conditions may be accounted for by the fact that H is from CH_4, which is injected throughout the outer circle instead of the inner center. A comparison between the EDC-Mechanism101 and the EDC-REDRAM shows that the H_2 fraction in EDC-REDRAM is much lower than that in the former model, perhaps resulting from the differences in their reactions and Arrhenius parameters as mentioned above.

From Figure 5.18, it can be seen that similar to the H fraction, the recirculation region of CH_4 contains the H_2 fraction in the flamelet results higher than that in the EDC results. These similar phenomena may share the same reason because the flamelet model yields a result closer to the equilibrium condition than that of the EDC model.

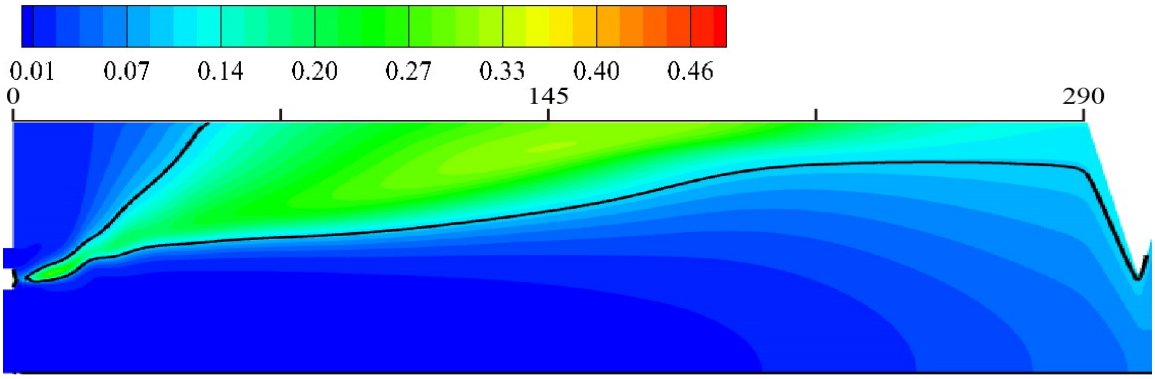

(a) EDC GRI 3.0

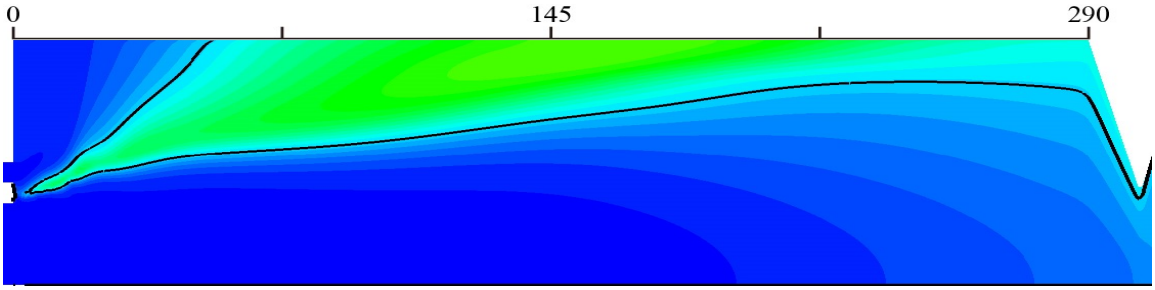

(b) EDC Mechanism 101

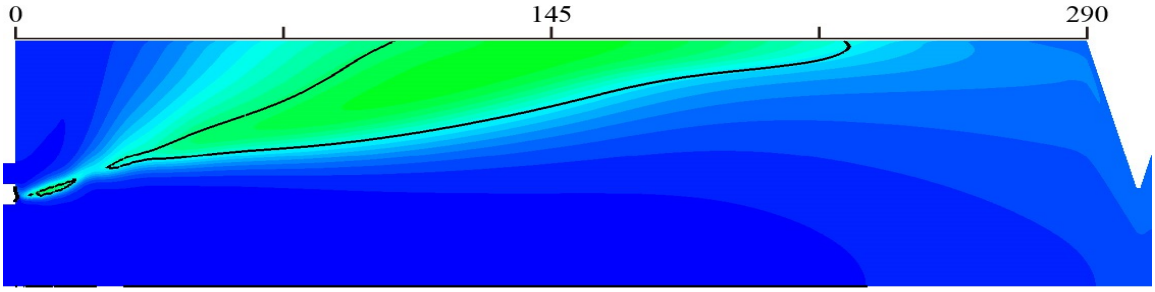

(c) EDC REDRAM

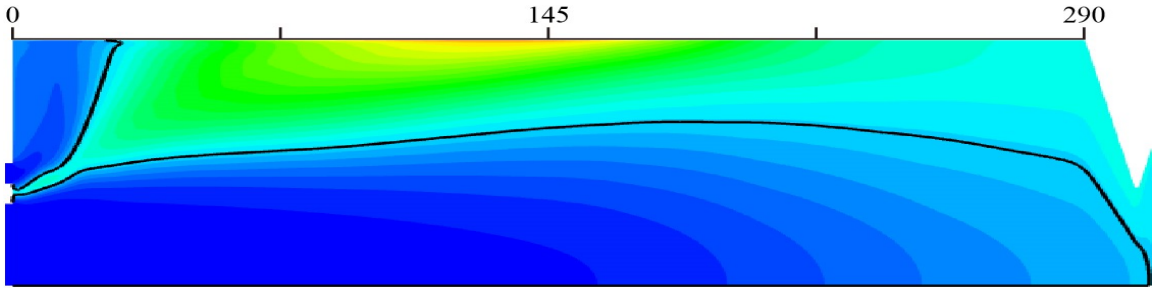

(d) FLAMELET Mechanism-101

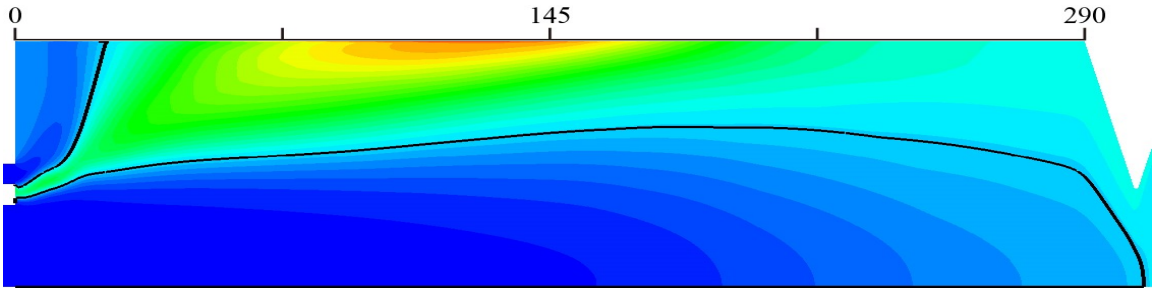

(e) FLAMELET Slavinskaya

Figure 5.18 H_2 mole fraction contours at symmetry of different models with H_2=0.1 line

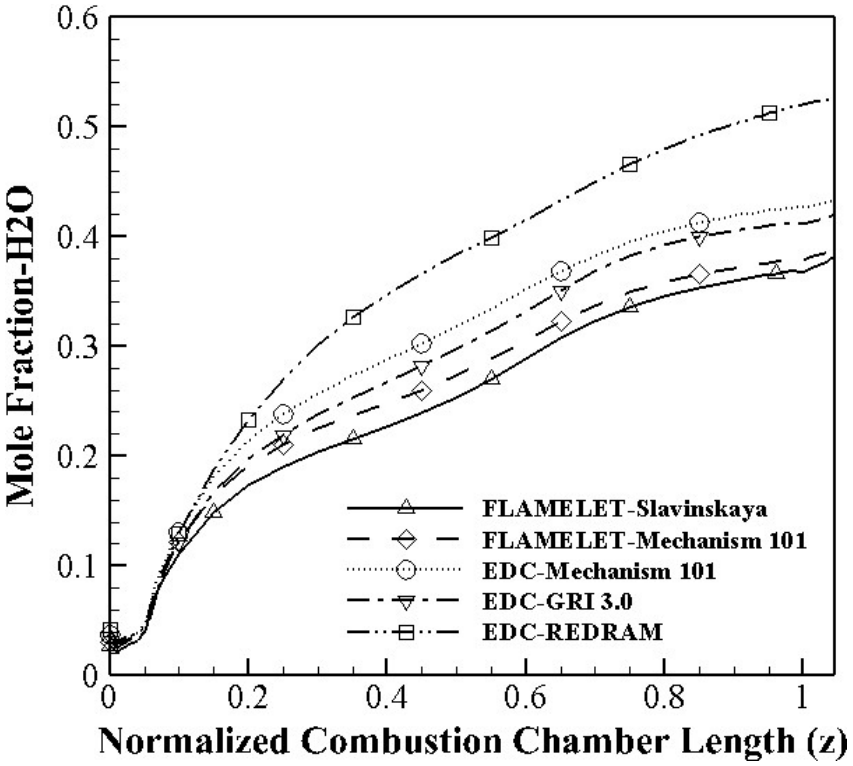

Figure 5.19 H_2O mole fractions of different models

In Figure 5.19, all five simulation results increase throughout 0<z<1, with the highest level reached by EDC-REDRAM, followed by EDC-GRI 3.0 and EDC-Mechanism 101, and the lowest by flamelet-Slavinskaya and flamelet-Mechanism 101. The REDRAM mechanism encompasses four reactions containing H_2O: 1) HCO is formed from the reaction $OH+CH_2O<=>HCO+H_2O$, 2) CO is generated by $HCO+H_2O<=>H+CO+H_2O$, and 3) two reactions, $OH+CH_4<=>CH_3+H_2O$ and $2OH<=>O+H_2O$, produce H_2O. These four reactions indicate that the OH fraction would significantly alter the H_2O fraction; however, no significant differences among the OH fractions of the REDRAM and other mechanisms are found. Differences are also absent among Arrhenius parameters in the REDRAM mechanism. Mechanism 101 includes 13 reactions containing H_2O. One possible explanation for this greater number compared with that of REDRAM and other mechanisms is that in Mechanism 101 or GRI 3.0, H_2O is decomposed by other reactions, for instance, the reaction $OH+H_2<=>H+H_2O$. In comparison with flamelet Mechanism 101, EDC-Mechanism 101 predicts a higher H_2O result that corresponds to the CO_2 result. As CO_2 and H_2O are the final products, they indicate higher combustion efficiencies.

In addition to the results in Figure 5.20, the impact of H_2O on methane oxidation has been researched in other studies [104,105,106,107], which also investigated the influences of amounts of H_2O molecules on the concentrations of CO, CO_2, OH, H_2 and HO_2. For instance, the consumption of CO is mainly through the reactions $OH+CO<=>H+CO_2$ and $HO_2+CO<=>OH+CO_2$, and thus the oxidation of CO is largely determined by the concentration of OH and HO_2 radicals. It is assumed that the high amounts of H_2O boost the CO oxidation due to two reasons:

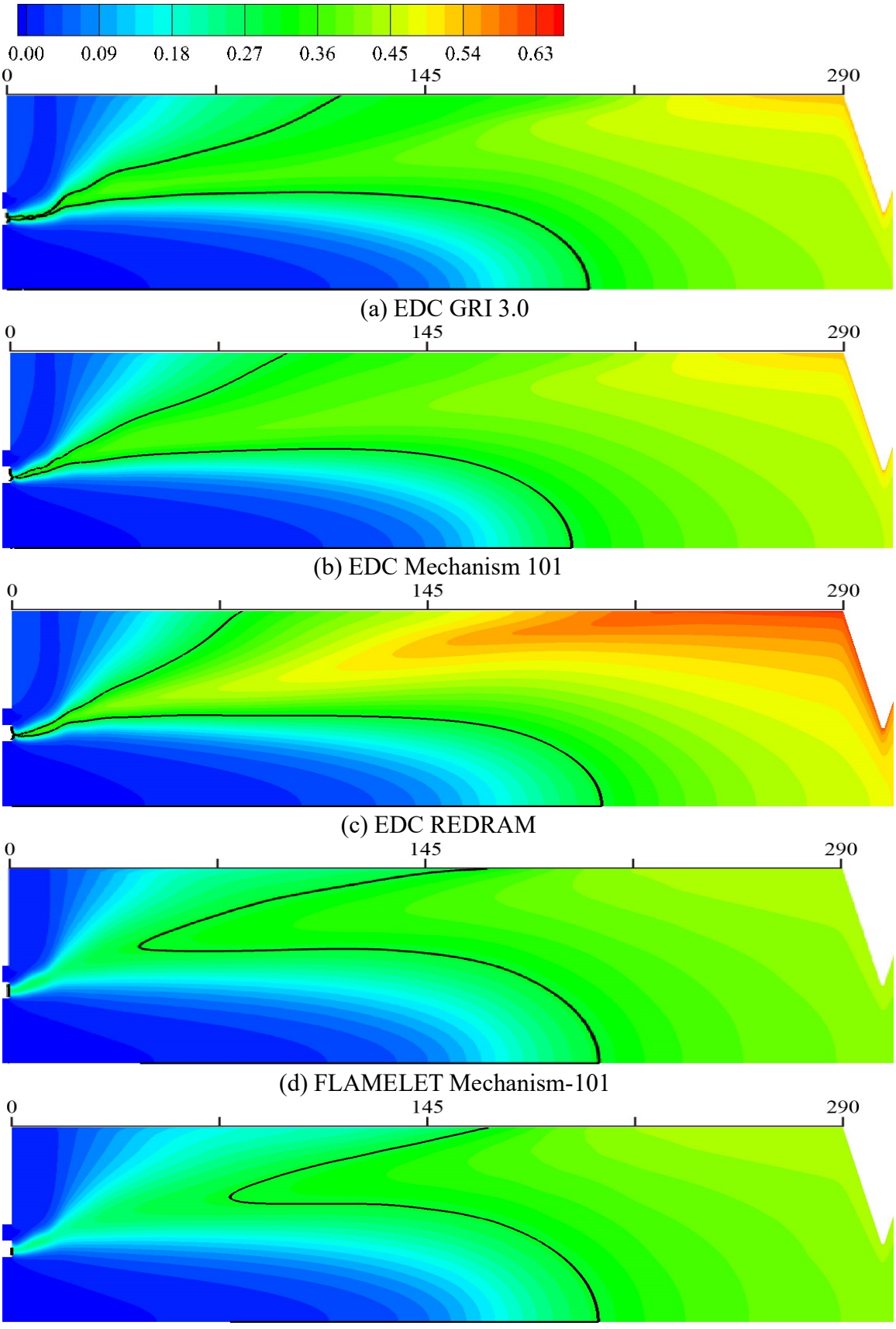

(a) EDC GRI 3.0

(b) EDC Mechanism 101

(c) EDC REDRAM

(d) FLAMELET Mechanism-101

(e) FLAMELET Slavinskaya

Figure 5.20 H_2O mole fraction contours at symmetry of different models with H_2O=0.3 line

1) H_2O radicals significantly modify the composition of the radical pool by regulating the production and consumption of OH radicals through the reactions $OH+H_2<=>H+H_2O$, and $OH+OH<=>O+H_2O$ [104, 106]. In these reactions, the increase of H_2O concentration quickens the production rate of OH radicals and consumption rate of H radicals. In turn, the generation of OH radicals favors the conversion of CO through the reaction $OH+CO<=>H+CO_2$.

2) H_2O participates in the reaction $H+O_2+M<=>HO_2+M$ as an efficient collision partner, affecting its rate with the chaperon efficiency [104,105,106,107]. In this reaction, M, comprised of O_2, H_2O, CO, CO_2, C_2H_6 and so on, affects the concentrations of H, O_2 and HO_2. In the REDRAM mechanism, the chaperon efficiency of H_2O is seven, much higher than that of any other species (N_2 is 1, O_2, 0.3; CO, 0.75; CO_2, 1.5; AR, 0.5; C_2H_6, 1.5) in this reaction, which signifies that H_2O greatly affects the reaction rate. As REDRAM predicts a much higher H_2O concentration than in other mechanisms, this reaction rate in simulation results with REDRAM is higher than those in other mechanisms. Correspondingly, more HO_2 is formed with REDRAM, which is shown in the HO_2 fraction results. In REDRAM, the conversion of CO to CO_2 follows reactions $HO_2+CO<=>OH+CO_2$ and $OH+CO<=>H+CO_2$. The high amounts of HO_2 raise the reaction rate of $HO_2+CO<=>OH+CO_2$, and as a result, the fraction of CO_2 is overpredicted and that of CO is underestimated, which are shown in their fraction results with REDRAM.

In REDRAM, H_2O is formed through three reactions: $OH+CH_2O<=>HCO+H_2O$, $OH+CH_4<=>CH_3+H_2O$ and $2OH<=>O+H_2O$. One explanation for REDRAM's overestimation of the concentration of H_2O and underestimation of H_2 is due to the absence of the reaction $OH+H_2<=>H+H_2O$ in REDRAM. The study [104] has shown that high levels of H_2O reduce the H radicals through this reaction. This study assumed that H_2O formed from the above three reactions partially converts to H_2 through the reaction $OH+H_2<=>H+H_2O$. In the contour of the fraction of H_2O with REDRAM, significant differences between REDRAM's H_2O fraction and those in other mechanisms show up in the rear of the chamber instead of the front, especially in the region near the walls. This is assumed to be because with REDRAM, the formed H_2O near the wall cannot be converted to H_2 due to REDRAM lacking the reaction $OH+H_2<=>H+H_2O$. The lower H_2 fraction of REDRAM compared with those of other mechanisms is shown in the H_2 fraction results. This hypothesis is supported by REDRAM's contours of H_2 and H_2O: the high concentration region of H_2O precisely overlaps the low concentration region of H_2. A comparison between H_2O's contour of REDRAM and those contours of other mechanisms shows the higher fraction of H_2O with REDRAM near the chamber walls; this region corresponds to the low H_2 region in the H_2 contours of REDRAM as shown in Figure 5.18. Theoretically, Mechanism 101 and GRI 3.0 both include the reaction $OH+H_2<=>H+H_2O$, through which H_2O is converted to H_2, and the accumulation of H_2O near the wall is weakened. However, in REDRAM, which lacks this reaction, H_2O gradually accumulates as the reactions progress.

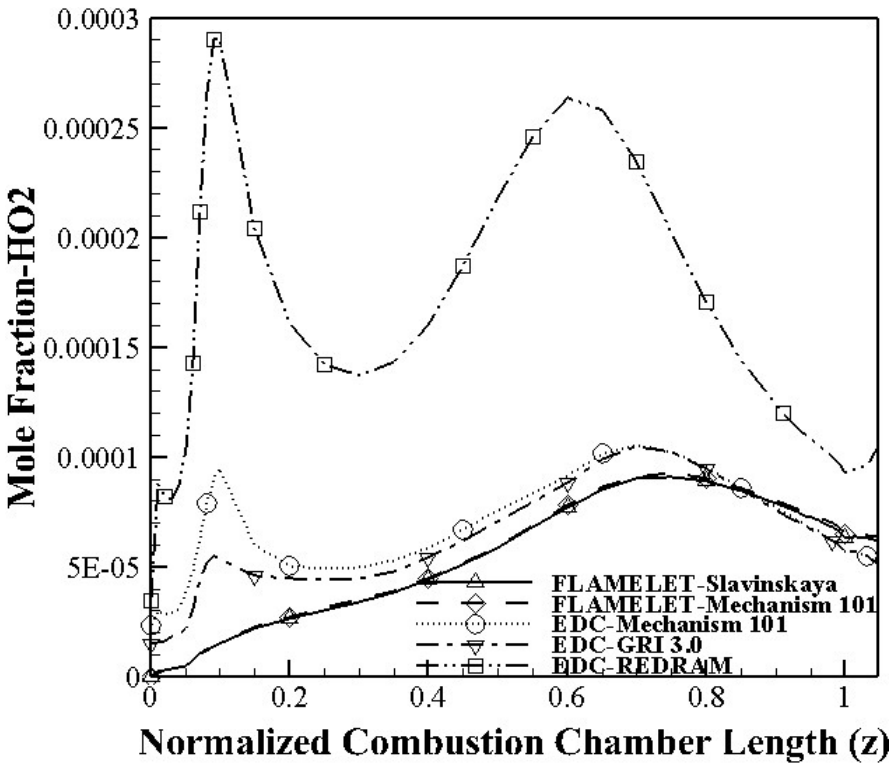

Figure 5.21 HO_2 mole fractions of different models

In Figure 5.21, the EDC-REDRAM and EDC-Mechanism 101 results both show a sharp increase in the HO_2 fraction after the injection followed by a severe decrease in the region of 0.1<z<0.2. Beginning at z=0.3, the fraction in EDC-Mechanism 101 rises steadily to z=0.7 and then diminishes through to z=1, presenting an identical result with that of the EDC-GRI 3.0. In contrast, the differences between the results of the flamelet approaches are negligible throughout the combustor length. With only negligible tracking of the fraction's first increase, the flamelet model indicates a steady climb in the HO_2 fraction. Comparing the flamelet results with those of the two EDC results (EDC-Mechanism 101 and EDC-GRI 3.0) demonstrates that near the injection plate, the initial increase in the fraction tracked by the EDC model is largely missed by the flamelet model. This may result from taking into account the influence of the turbulence generated by the injection on the reactions when calculating the interaction between chemistry and hydrodynamics.

As shown in Figure 5.22, a radical pool's formation and depletion generally regulates ignition chemistry. The relatively unreactive CH_3 and HO_2 comprised the controlling radicals under 1,100 K at 100 bar. When methane oxidation is subject to increased pressures, HO_2 and reactions such as $2CH_3(+M)<=>C_2H_6(+M)$ are of increased importance. For example, in REDRAM at 1,400 K, $HO_2+CH_3<=>OH+CH_3O$ and $O_2+CH_2O<=>HO_2+HCO$ are two of the four dominant fuel-rich ignition promoters, and $2HO_2<=>O_2+H_2O_2$ is one of the ignition inhibitors. At 1,100 K, different ignition promoters are substituted, but $HO_2+CH_3<=>OH+CH_3O$ remains among the top five. The influence of $HO_2+CH_2O<=>H_2O_2+HCO$ on the ignition is likely caused by the reaction's generation of hydrogen peroxide (H_2O_2), which rapidly decomposes into 2OH radicals.

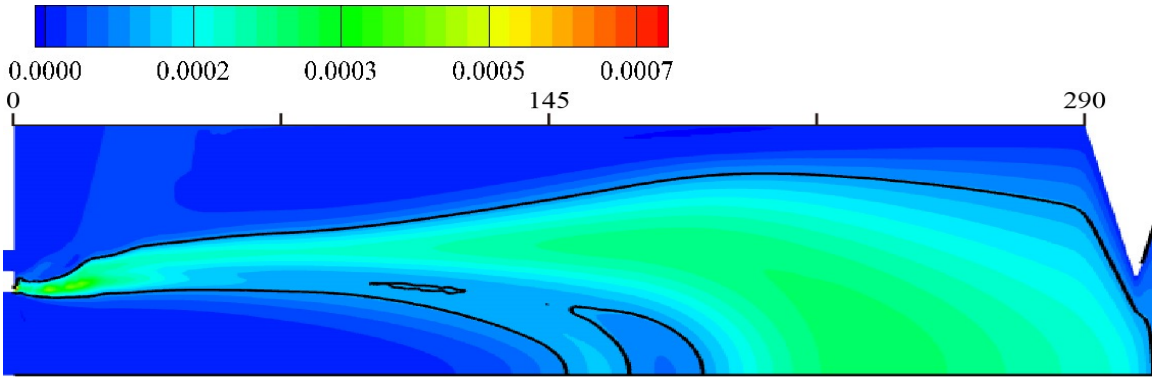

(a) EDC GRI 3.0

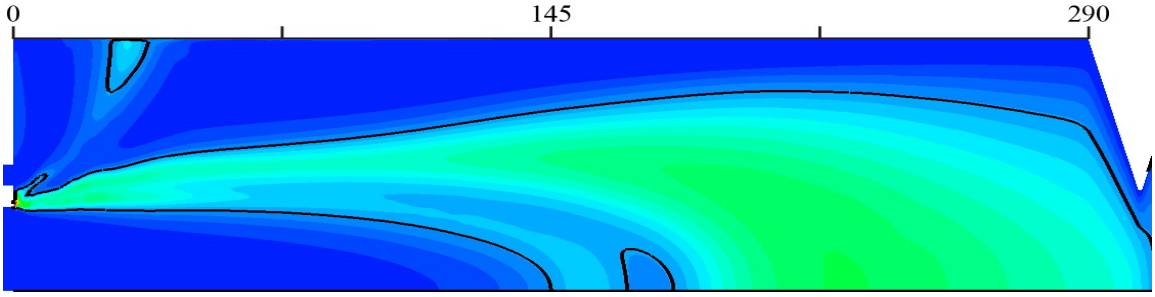

(b) EDC Mechanism 101

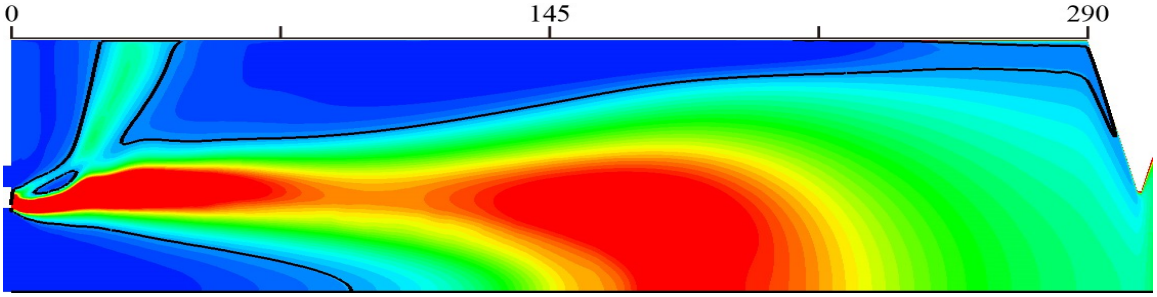

(c) EDC REDRAM

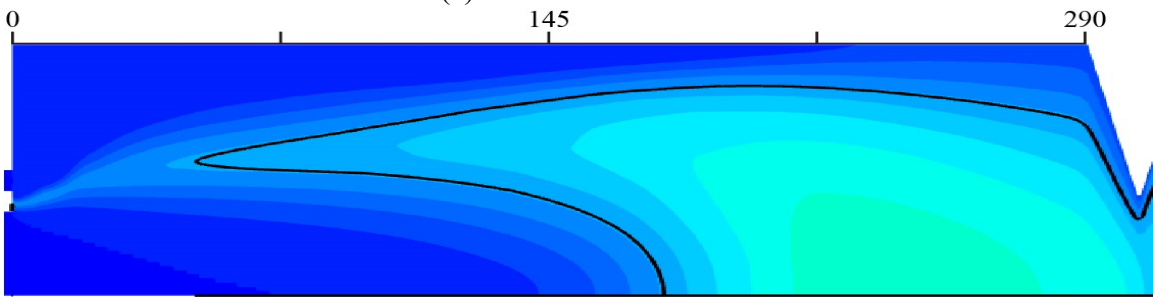

(d) FLAMELET Mechanism-101

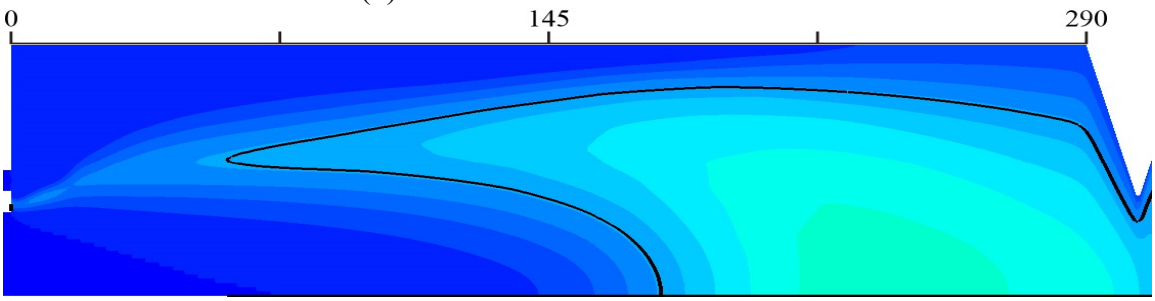

(e) FLAMELET Slavinskaya

Figure 5.22 HO_2 mole fraction contours at symmetry of different models with HO_2=0.0001 line

In Figure 5.22 the contours of the three EDC results show that HO_2 accumulates near the injector tip, which may occur from the intense mixture between the two propellants. As the propellants leave the intense mixture region, the HO_2 fraction decreases outside the region and increases in the rear part of the chamber. In theory, this climbing and descending process may be the result of a three step process. Under this conjecture, the first increase results from the shear force between the two propellants near the tip raising the turbulence intensity and correspondingly hastening the reactions; this acceleration is reflected in the increase of the HO_2 fraction, an intermediate species. As the propellants move away from the tip, the turbulence weakens and the fraction regresses. The second increase occurs as the temperature increases, a favorable factor of the reactions. Nearing the nozzle, the fraction decreases and the equilibrium condition is disrupted by the change in the static temperature.

Figure 5.22 shows that EDC-REDRAM predicts higher HO_2 fractions compared with those of Mechanism 101 and GRI 3.0. The HO_2 fraction is regulated by the O_2 and H_2O fractions through different reactions. For instance, in REDRAM the presence of high amounts of H_2O boost the reaction $H+O_2+M$ as an efficient collision partner [106]. In addition, the high O_2 levels promote the generation of HO_2 through the reactions $HO_2+CH_3<=>O_2+CH_4$, $O_2+CH_2O<=>HO_2+HCO$, $2HO_2<=>O_2+H_2O_2$, $CH_3O+O_2<=>HO_2+CH_2O$, $H+O_2+M<=>HO_2+M$ and $HCO+O_2<=>HO_2+CO$. The pre-exponential factors (A) are other causes of the different O_2 fractions of EDC-REDRAM and EDC-Mechanism101. A comparison between the factors in EDC-REDRAM and those of the EDC-Mechanism101 illustrates the differences in several reactions, with $HO_2+CH_2O<=>H_2O_2+HCO$ being the most representative. The pre-exponential factor of this reaction in REDRAM is 1.0E+12, while in Mechanism 101 it is 5.6E+6. The different pre-exponential factors in the two mechanisms are presumed to be a source of the variations in the HO_2 fraction among different mechanisms.

As Figure 5.23 presents, the O_2 fractions track similarly, which at z=0 (the inlet) approximate 0.1, and then rise sharply as they approach 0.2 at z=0.2. In the region of $0.2<z<0.5$, they begin to level off before declining to z=1. This process can be explained with the following theory: because methane accumulates near the injection plate during its recirculation, the oxygen fraction increases in the region between $0<z<0.2$. In the region of $0.2<z<0.6$, even though CH_4 falls, several species such as the CO, H_2O and CO_2 rise as shown in Fig. 5.4-5.8. As a result, the fractions of the three EDC results descend as those of the two flamelet results ascend. Beyond z=0.6, as the reactions consume oxygen, each result shows a moderate decline.

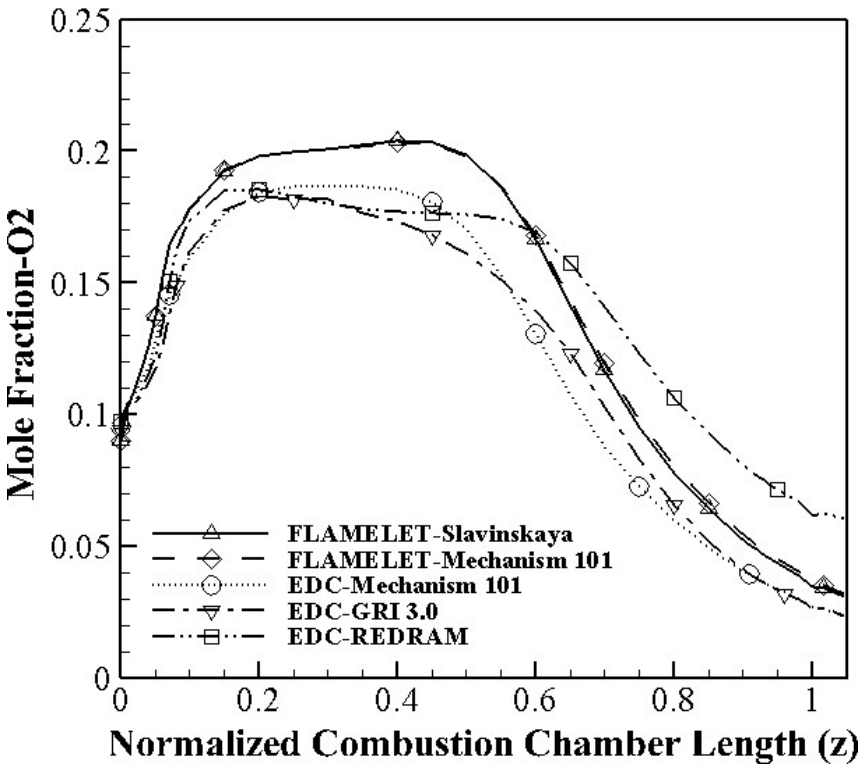

Figure 5.23 O_2 mole fractions of different models

In Figure 5.23, at z=1.046 (the outlet), all results track oxygen residual fractions above 0.02, which represent incomplete combustion inside the chamber. The respective O_2 residual fractions of flamelet-Slavinskaya and flamelet-Mechanism101 are 0.031 and 0.037, while those of EDC-GRI 3.0, EDC-Mechanism101 and EDC-REDRAM are 0.023, 0.023 and 0.06. Comparing the EDC-Mechanism 101 and flamelet-Mechanism 101 fractions reveals that the EDC model consumes more oxygen and predicts higher combustion efficiency than the flamelet model; this results from the former model's more complex turbulence chemistry interaction model. Seller et al. [98] conducted a numerical simulation study of this test case implementing a LES model in which the flame/eddies interaction is fully resolved on the grid without an additional model; their study predicted complete combustion without residual oxygen. Upon examining the combustion efficiencies of the flamelet, EDC and LES models, it would appear that the more detailed description of turbulence/combustion interaction, the higher the predicted combustion efficiency.

Figure 5.23 demonstrates that comparing the residual oxygen fractions of EDC-Mechanism 101 and EDC-REDRAM proves that the former model predicts a higher combustion efficiency, which is presumably caused by the differences among the reactions and the Arrhenius parameters, as heretofore discussed.

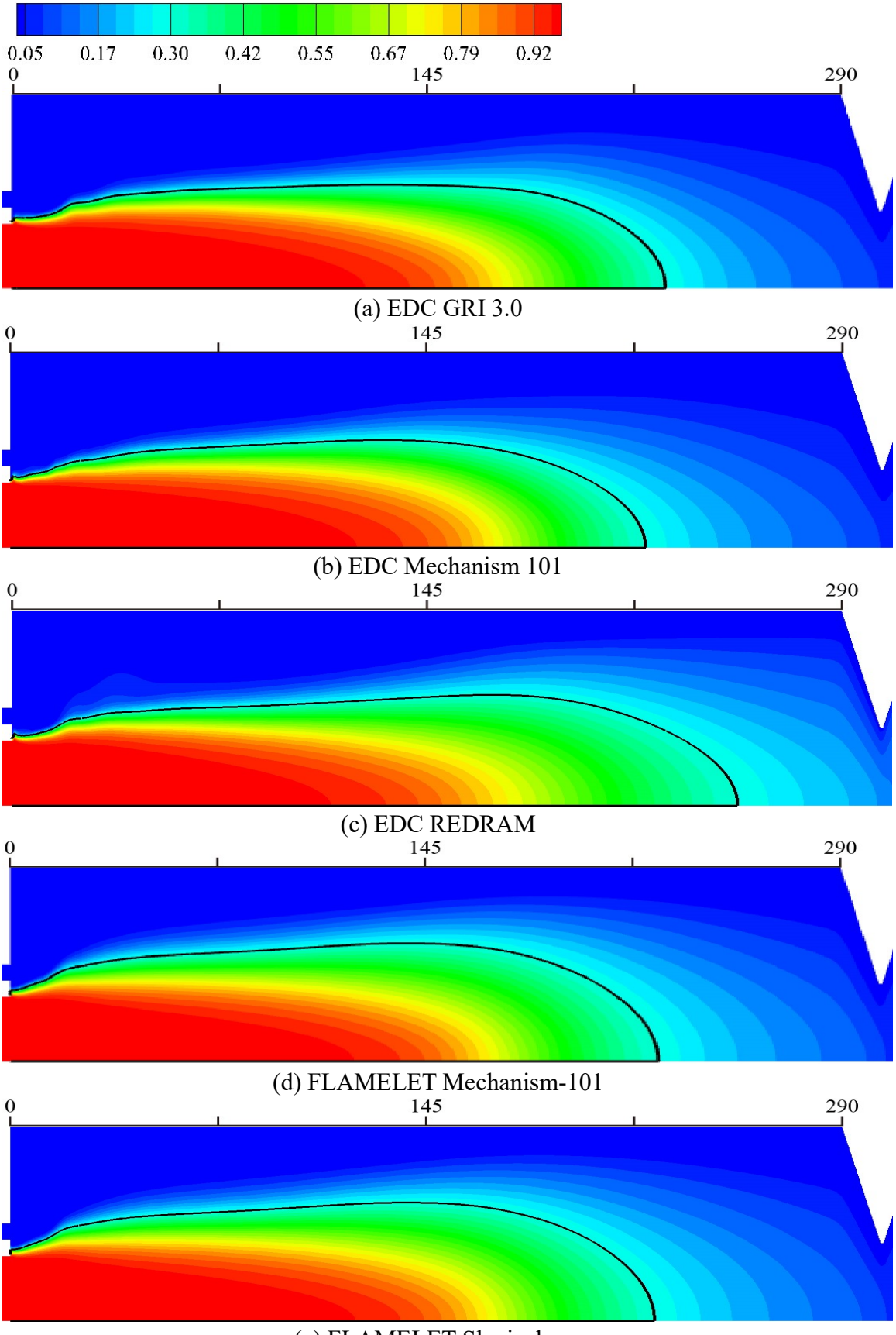

Figure 5.24 O_2 mole fraction contours at symmetry of different models with O_2=0.3 line

Contours in Figure 5.24 show primarily consistent results: in the chamber's front half,

the O_2 concentration is highly elevated, while it decreases in the rear half as the reactions occur and oxygen is consumed. The EDC-REDRAM has a longer rich oxygen region than seen in other results, possibly because of the aforementioned reactions and Arrhenius parameters. Comparing GRI 3.0 and REDRAM indicates that REDRAM's overestimation of the oxygen fraction is due to the Arrhenius parameters of three representative reactions. The pre-exponential factor of the reaction $H+O_2<=>O+OH$ in REDRAM is 8.3E+13, while in GRI 3.0 it is 2.65E+16; the factor of the reaction $CH_3+O_2<=>OH+CH_2O$ in REDRAM is 3.6E+10, while in GRI 3.0 is 2.31E+12; and the factor of the reaction $C_2H_3+O_2<=>HCO+CH_2O$ in REDRAM is 3.98E+12 while in GRI 3.0 is 4.58E+16. Three factors in REDRAM are several orders lower than those in GRI 3.0, which implies slower consumption rates of O_2 radicals and results in a higher O_2 residual fraction at the outlet.

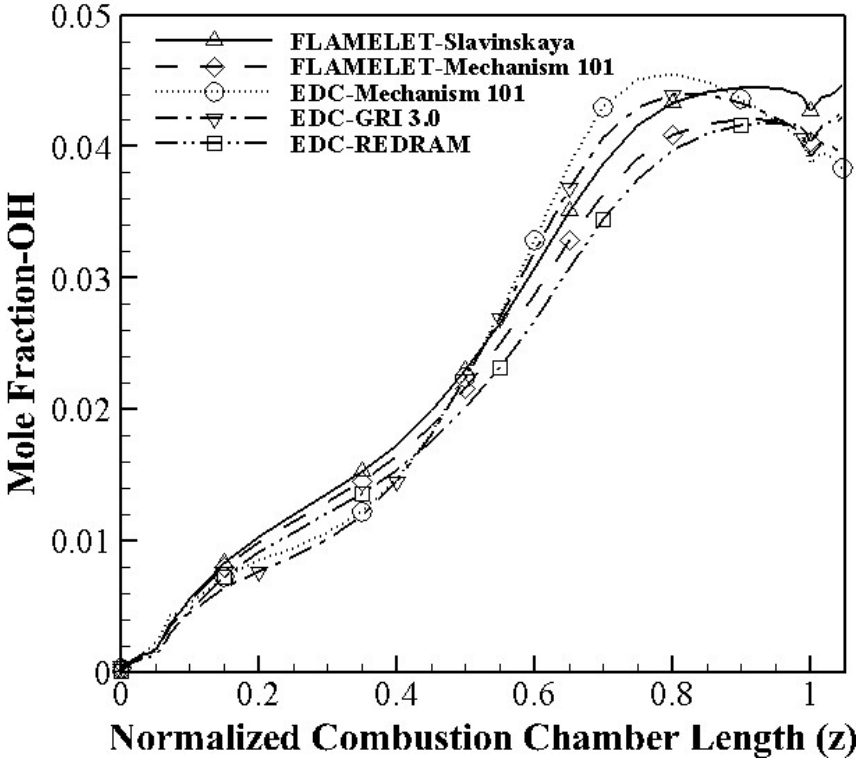

Figure 5.25 OH mole fractions of different models

An accepted method to visualize rocket flames is the use of the excited hydroxyl radical (OH*) [108]. Radiation from this radical is often approximated in a comparison with simulated OH mass fractions because numerical simulations in most cases contain no OH* radiation [108,109]. In Figure 5.25, the OH fractions track similarly: zero at the beginning of the chamber (z=0). As the reactions occur, the OH fractions gradually increase to z=0.4, and then rise more rapidly to their peaks at approximately z=0.8, at which the flamelet-Slavinskaya and EDC-REDRAM continue rising slightly before following the other three results in a sudden decline to z=1 (the nozzle). They all then increase again to z=1.046 (the outlet). All these results have different peaks, with the EDC-REDRAM model dropping from its peak of 0.0417473 at z=0.94. The comparison between the OH fractions of EDC-Mechanism 101 and flamelet-Mechanism 101 expresses the following predictions regarding the EDC model: 1) an EDC-Mechanism

101 peak width narrower than that of the flamelet-Mechanism 101, which indicates a slower rate of change of the OH fraction; 2) a higher OH fraction than that of the flamelet model, which indicates stronger combustion at the peaks; and 3) an earlier peak in the EDC-Mechanism 101 model, which indicates a shorter flame length. The comparison between the flamelet-Slavinskaya and the flamelet-Mechanism 101 shows that the former mechanism predicts a higher, later and wider peak in contrast with the latter mechanism. The OH fractions of EDC-Mechanism 101 and EDC-GRI 3.0 follow nearly identical tracks.

It is difficult to obtain precise measurements of flames in rocket motors owing to the high levels of temperature and pressure during combustion. In this hostile environment, the parameters relevant to combustion, such as the temperature or species mole fractions, are especially problematic to measure. Without precise data regarding such parameters, the causation and validation of the simulation results remain subject to investigation.

Figure 5.26 illustrates that as the reactions occur the fractions gradually increase. The acceleration of reactions by a shear force in the three EDC results track similarly to the contours of the distribution of species CO_2. As discussed above, the shear force creates the elevated turbulence and correspondingly accelerates the EDC model's chemical reactions. While the flamelet model introduces a non-equilibrium approach, some differences with the EDC model have been cited to argue for the superiority of the EDC model over the flamelet model. In addition to the differences between two TCI models, the contours in Figure 5.26 highlight the differences between the mechanisms. REDRAM contains 10 reactions that encompass OH, while Mechanism 101 involves 21 such reactions. In the contours, the difference between the OH fractions of EDC-Mechanism 101 and EDC-REDRAM may come from the formation and decomposition of OH, as well as the reactions and the Arrhenius parameters. The REDRAM contains five reactions that produce OH, in contrast with Mechanism 101 which includes seven such reactions. The REDRAM reactions contain HO_2+CO<=>OH+CO_2, unlike the Mechanism 101 reactions. These two sets of reactions also differ significantly in their Arrhenius parameters. For pre-exponential factors, H+O_2<=>O+OH in REDRAM is 8.300E+13; in Mechanism 101, it is 2.650E+16. In REDRAM, CH_3+O_2<=>OH+CH_2O is 3.600E+10; in Mechanism 101, it is 2.310E+12.

Regarding decomposition in REDRAM, OH is consumed in the five such reactions by CO, CH_4, CH_2O, 2OH<=>O+H_2O and OH (+M) <=>H_2O_2(+M). In Mechanism 101, they are consumed by H_2, HO_2, H_2O_2, CH_2, CH_3, CH_4, CO, CH_2O, C_2H_2, C_2H_5, HO_2 and CH_3. As a result, the above species may alter the OH fraction of Mechanism 101, especially in the rear chamber, where the difference is large. No obvious difference between the Arrhenius parameters of the REDRAM and Mechanism 101 has been seen.

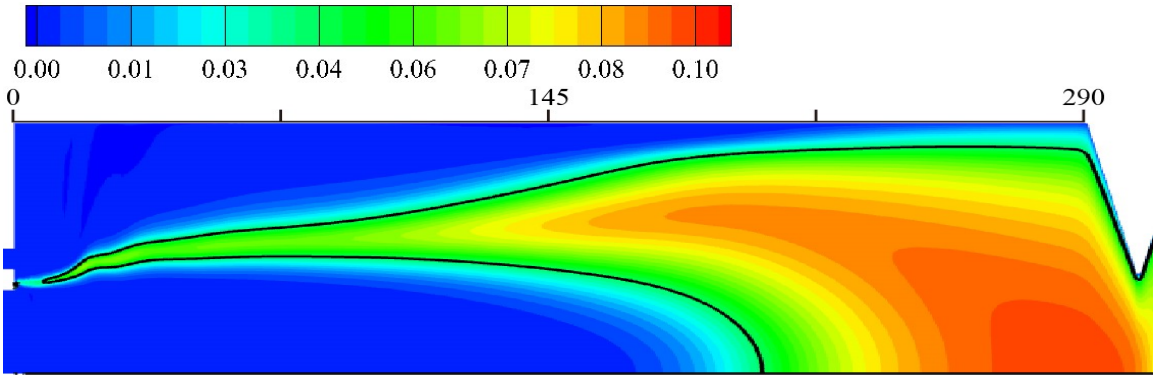

(a) EDC GRI 3.0

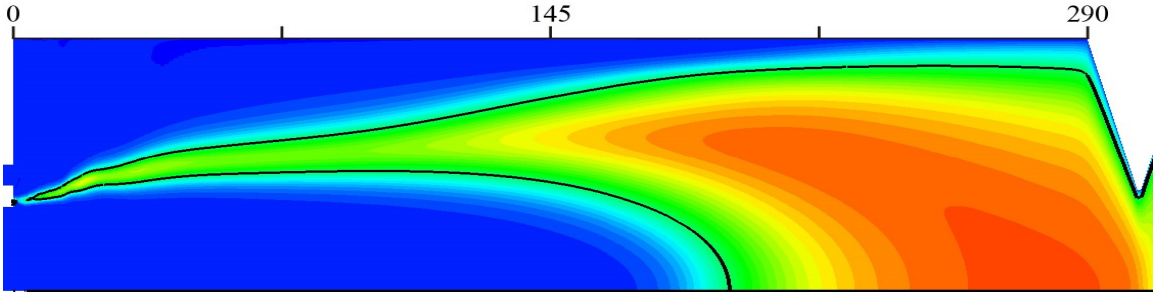

(b) EDC Mechanism 101

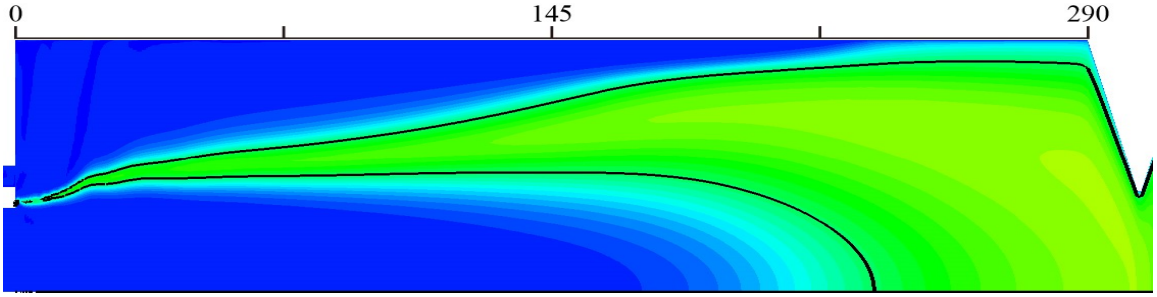

(c) EDC REDRAM

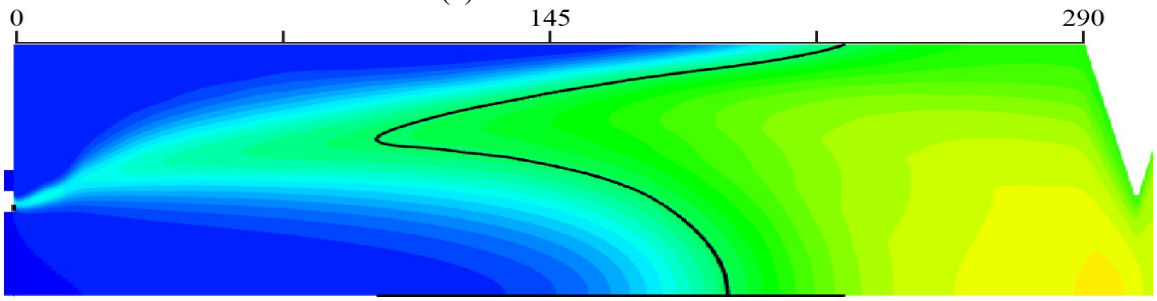

(d) FLAMELET Mechanism-101

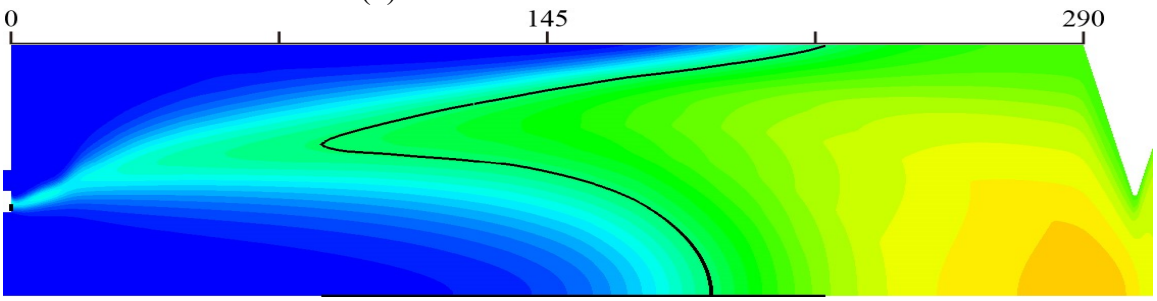

(e) FLAMELET Slavinskaya

Figure 5.26 OH mole fraction contours at symmetry of different models with OH=0.04 line

6. Conclusion and Future Work

In this dissertation, a newly reduced finite-rate gas-phase CH_4/O_2 reaction mechanism for CFD simulations of turbulent combustion in combustors is developed, validated and implemented. This mechanism (22 species and 58 reactions) is reduced from GRI 3.0 based on reaction path analyses and sensitivity analyses and proposed for a campaign of numerical simulations of gas oxygen-gas methane combustion at 20 bar in rocket engines.

The applicability of Mechanism101 is validated for ignition delay times and laminar flame speeds over a wide range of mixture ratios and operating pressures, in comparison with the simulation results with GRI 3.0. Results obtained with Mechanism101 coincide with experimental data and predictions from GRI 3.0 and show improvement of the ignition delay prediction compared with GRI 3.0 in temperatures lower than 1,100 K because of the addition of CH_3O_2.

The effects of the chemistry mechanism and combustion model on the predictions of the species fractions, wall heat flux, and wall pressure profiles in a chamber are examined. Numerical predictions are validated based on a single-element GO_2/GCH_4 combustor test case conducted at the Institute of Turbomachinery and Flight Propulsion of Technical University of Munich.

The interaction between the turbulence and chemical reactions is considered by adopting the eddy dissipation concept model and flamelet model. In the simulation results, the temperature contour illustrates that the hot zone near the tip denotes that the velocity difference between the two propellants generates the shear force that enhances the turbulence, which quickens the chemical reactions in this region. In both the experiment and simulation results, the heat flux increases rapidly within the first 20 mm of the chamber, after which it declines slightly before rising again along the chamber length in the region to 290 mm; in the recirculation region of methane, the pressure rises sharply to its peak and, in turn, gradually declines and slowly plateaus. In general, it can be concluded that the current simulations can predict the flow and combustion processes in terms of the validation of the two typical rocket design parameters, i.e., wall heat flux and chamber pressure. Nevertheless, the simulation results have some quantitative discrepancies with the test data, either with heat flux or chamber pressure.

Comparing Mechanism 101's predictions in the different contexts of the EDC model and flamelet model illuminates that the EDC model predicts more precise results than does the flamelet model. For instance, the flamelet predicts an earlier plateau of the heat flux than does the EDC model, presumably because of the different assumptions posited by the two combustion models and different computational methods of the transport properties. In addition, differences of fractions of several species, such as H_2, H_2O and HO_2, are observed theoretically due to the different descriptions of the turbulence-chemistry interaction. The simulation results of LES have also been compared with those of RANS, represented by the EDC and flamelet results. In simulations of high Reynolds number turbulent flows, the requirement of fine mesh near walls, typically associated with expensive computational costs, limits the

implementation of LES models; alternatively, in such simulations the RANS EDC model provides comparable results in a more economical manner.

The differences among simulation results of the four mechanisms (Mechanism 101, GRI 3.0, REDRAM and Slavinskaya) illustrate that the predictions of several species, such as O_2, HO_2, CO_2, CO and HO_2, are significantly influenced by the chemistry mechanisms. With different reactions and their parameters, REDRAM predicts a higher residual oxygen fraction that indicates less oxygen is consumed than in GRI 3.0. In addition, lacking the reaction OH+H2<=>H+H_2O, REDRAM underestimates the H_2 fraction and overpredicts the H_2O fraction. Under the regulations of O_2 and H_2O fractions, and effects from the reactions and their coefficients, HO_2 is overpredicted by REDRAM, resulting in a higher conversion of CO to CO_2. Correspondingly, REDRAM predicts higher CO_2 and H_2O fractions than predicted by other mechanisms. Moreover, the fraction results show that in the downstream region, where turbulence decays and temperature rises, the predictions become more sensitive to reaction mechanisms in the EDC model. The differences among fractions of different mechanisms gradually increase as the reactions progress. Comparing the pressures of EDC GRI 3.0 and EDC REDRAM shows that REDRAM predicts a lower pressure than does GRI 3.0 due to REDRAM's higher residual oxygen fraction. Correspondingly, less heat is released by the reactions, which contributes to lower heat flux and pressure.

Although a comparable simulation result is yielded with the current approach, it is necessary to note that the chamber wall boundary is imposed with a temperature profile obtained from the test data. In principle, to a given issue, a simulation should be independent of any experimental data. In that case, however, the solid enclosing the chamber must be conjugated to the current computational domain and a coupled simulation should be performed, which would add greatly to the simulation's complexity.

Even though Mechanism 101 exactly predicts the trend of the pressure and heat flux in the combustion chamber, what is noticeable is that this reduced mechanism is incapable of reflecting the soot formation process during combustion because it is a derivative of GRI 3.0 that contains insufficient species, except CH_2(s), to investigate the formation process of soot. The possibility to format soot under fuel rich conditions, such as in the gas generators and film cooling regions in the chambers, is noticeably high. Based on the Slavinskaya mechanism [103], further investigation of the conversion from CH_4 to soot is ongoing.

Bibliography

1 Schneider, D., & Genin, C. (2016). Impact of different chemical models on the numerical prediction of dual-bell nozzle transition. *SFB/TR 40 Annual Report*.
2 Klepikov, I. A., Katorgin, B. I., & Chvanov, V. K. (1997). The new generation of rocket engines, operating by ecologically safe propellant "liquid oxygen and liquefied natural gas (methane)". *Acta Astronautica*, *41*(4-10), 209-217.
3 Smith, G.P., Golden, D.M., Frenklach, M., Moriarty, N.W., Eiteneer, B., Goldenberg, M., Bowman, C.T., Hanson, R.K., Song S., Gardiner, W.C….&Qin, Z., http://www.me.berkeley.edu/gri mech/
4 Metcalfe, W. K., Burke, S. M., Ahmed, S. S., & Curran, H. J. (2013). A hierarchical and comparative kinetic modeling study of C1−C2 hydrocarbon and oxygenated fuels. *International Journal of Chemical Kinetics*, *45*(10), 638-675.
5 Zhukov, V. P. (2009). Kinetic model of alkane oxidation at high pressure from methane to n-heptane. *Combustion Theory and Modelling*, *13*(3), 427-442.
6 Sutton, G., Biblarz, O., (2010), Rocket propulsion elements, 8th ed, John Wiley & Sons, Hoboken, New Jersey.
7 Seregin, A.V., Liquid rocket propellants (Zhidkiye raketnyye topliva), Voyennoye Izdatel'stvo Ministerstva Oborony SSSR, Moscow, 1962.
8 Unnikrishnan, U., Oefelein, J. C., & Yang, V. (2018). Direct numerical simulation of a turbulent reacting liquid-oxygen/methane mixing layer at supercritical pressure. AIAA 2018-4564, In *2018 Joint Propulsion Conference,* doi: 10.2514/6.2018-4564.
9 Herrera, M., Garcia, M. B., Adams, J., Choudhuri, A. R., & Chessa, J. (2018). Design and development of a 500 lbf liquid oxygen/liquid methane engine. AIAA 2018-4605, In *2018 Joint Propulsion Conference*, doi: 10.2514/6.2018-4605.
10 Hardi, J. S., Traudt, T., Bombardieri, C., Börner, M., Beinke, S. K., Armbruster, W., ... & Oschwald, M. (2018). Combustion dynamics in cryogenic rocket engines: research programme at DLR Lampoldshausen. *Acta Astronautica*, 147, 251-258.
11 Haidn, O. J., Adams, N., Radespiel, R., Schröder, W., Stemmer, C., Sattelmayer, T., & Weigand, B. (2018). Fundamental technologies for the development of future space transport system components under high thermal and mechanical loads. AIAA 2018-4466, In *2018 Joint Propulsion Conference*, doi: 10.2514/6.2018-4466.
12 Takahashi, H., Tomita, T., Génin, C., & Schneider, D. (2018). LOX/CH4 hot-flow testing of dual-bell nozzles with rapid-expansion extension. *Journal of Propulsion and Power*, *34*(5), 1214-1224.
13 Hurlbert, E. A., Ueno, H., Alexander, L., Klem, M. D., Daversa, E., Rualt, J. M., ... & Whitley, R. J. (2016). International space exploration coordination group assessment of technology gaps for LOX/methane propulsion systems for the global exploration roadmap. AIAA 2016-5280, In *AIAA SPACE 2016*, doi: 10.2514/6.2016-5280.
14 Fang, X. X., & Shen, C. B. (2017). Study on atomization and combustion characteristics of lox/methane pintle injectors. *Acta Astronautica*, *136*, 369-379.
15 Dai, J., Cai, G., Zhang, Y., & Yu, N. (2016). Experimental investigations of coaxial injectors in a laboratory-scale rocket combustor. *Aerospace Science and Technology*, *59*, 41-51.
16 Lapenna, P. E., Amaduzzi, R., Durigon, D., Indelicato, G., Nasuti, F., & Creta, F. (2018). Simulation of a single-element GCH4/GOx rocket combustor using a non-adiabatic flamelet method. AIAA 2018-4872, In *2018 Joint Propulsion Conference,*doi: 10.2514/6.2018-4872.
17 Leccese, G., Bianchi, D., & Nasuti, F. (2018). Numerical investigation on the role of thermal radiation in hybrid rocket fuel pyrolysis. AIAA 2018-4924, In *2018 Joint Propulsion Conference,* doi: 10.2514/6.2018-4924.
18 Pizzarelli, M., Nasuti, F., Votta, R., & Battista, F. (2016). Validation of conjugate heat transfer model for rocket cooling with supercritical methane. *Journal of Propulsion and Power*, 32(3), 726-733.
19 Huo, H., & Yang, V. (2017). Large-Eddy simulation of supercritical combustion: model validation against gaseous H2–O2 Injector. *Journal of Propulsion and Power*, *33*(5), 1272-1284.
20 Betti, B., Bianchi, D., Nasuti, F., & Martelli, E. (2016). Chemical reaction effects on heat loads of CH_4/O_2 and H_2/O_2 rockets. *AIAA Journal*, *54*(1), 1693-1703.

21 Eiringhaus, D., Rahn, D., Riedmann, H., Knab, O., & Haidn, O. (2017). Numerical investigation of a 7-element GOX/GCH4 subscale combustion chamber. In *7th European Conference for Aeronautics and Space Sciences*, Milan, doi: 10.13009/EUCASS2017-173.
22 Chen, J. H. (2011). Petascale direct numerical simulation of turbulent combustion—fundamental insights towards predictive models. *Proceedings of the Combustion Institute*, *33*(1), 99-123.
23 Van Kalmthout, E., & Veynante, D. (1998). Direct numerical simulations analysis of flame surface density models for nonpremixed turbulent combustion. *Physics of Fluids*, *10*(9), 2347-2368.
24 Im, H. G., Arias, P. G., Chaudhuri, S., & Uranakara, H. A. (2016). Direct numerical simulations of statistically stationary turbulent premixed flames. *Combustion Science and Technology*, *188*(8), 1182-1198.
25 Gruber, A., Sankaran, R., Hawkes, E. R., & Chen, J. H. (2010). Turbulent flame–wall interaction: a direct numerical simulation study. *Journal of Fluid Mechanics*, *658*, 5-32.
26 Pitsch, H. (2006), Large-eddy simulation of turbulent combustion, *Annual Review of Fluid Mechanics*, 38, 453-482.
27 Pitsch, H., & De Lageneste, L. D. (2002). Large-eddy simulation of premixed turbulent combustion using a level-set approach. *Proceedings of the Combustion Institute*, *29*(2), 2001-2008.
28 Vreman, A. W., Van Oijen, J. A., De Goey, L. P. H., & Bastiaans, R. J. M. (2009). Subgrid scale modeling in large-eddy simulation of turbulent combustion using premixed flamelet chemistry. *Flow, Turbulence and Combustion*, *82*(4), 511-535.
29 Oefelein, J. C., Schefer, R. W., & Barlow, R. S. (2006). Toward validation of large eddy simulation for turbulent combustion. *AIAA Journal*, *44*(3), 418-433.
30 Deardorff, J. W. (1970). A numerical study of three-dimensional turbulent channel flow at large Reynolds numbers. *Journal of Fluid Mechanics*, *41*(2), 453-480.
31 Sabelnikov, V., & Fureby, C. (2013). LES combustion modeling for high Re flames using a multi-phase analogy. *Combustion and Flame*, *160*(1), 83-96.
32 Fureby, C. (2009). Large eddy simulation modelling of combustion for propulsion applications. *Philosophical Transactions of the Royal Society A: Mathematical, Physical and Engineering Sciences*, *367*(1899), 2957-2969.
33 Urbano, A., Selle, L., Staffelbach, G., Cuenot, B., Schmitt, T., Ducruix, S., & Candel, S. (2016). Exploration of combustion instability triggering using large eddy simulation of a multiple injector liquid rocket engine. *Combustion and Flame*, *169*, 129-140.
34 Grilli, M., Hickel, S., & Adams, N. A. (2013). Large-eddy simulation of a supersonic turbulent boundary layer over a compression–expansion ramp. *International Journal of Heat and Fluid Flow*, *42*, 79-93.
35 Hickel, S., Adams, N. A., & Domaradzki, J. A. (2006). An adaptive local deconvolution method for implicit LES. *Journal of Computational Physics*, *213*(1), 413-436.
36 Stolz, S., Adams, N. A., & Kleiser, L. (2001). An approximate deconvolution model for large-eddy simulation with application to incompressible wall-bounded flows. *Physics of Fluids*, *13*(4), 997-1015.
37 Hickel, S., & Adams, N. A. (2008). Implicit LES applied to zero-pressure-gradient and adverse-pressure-gradient boundary-layer turbulence. *International Journal of Heat and Fluid Flow*, *29*(3), 626-639.
38 Fu, L., Han, L., Hu, X. Y., & Adams, N. A. (2019). An isotropic unstructured mesh generation method based on a fluid relaxation analogy. *Computer Methods in Applied Mechanics and Engineering*. 350(15), 396-431.
39 Spalart, P. R., Jou, W-H., Strelets, M., Allmaras, S.R. (1997). Comments on the feasibility of LES for wings, and on a hybrid RANS/LES approach. In *Proceedings of First AFOSR International Conference on DNS/LES*. Greyden Press.
40 Spalart, P.R. (2009), Detached-eddy simulation, *Annual Review of Fluid Mechanics*, 41, 181-202.
41 Mansouri, Z., Aouissi, M., & Boushaki, T. (2016). Detached eddy simulation of high turbulent swirling reacting flow in a premixed model burner. *Combustion Science and Technology*, *188* (11-12), 1777-1798.
42 Chaouat, B. (2017). The state of the art of hybrid RANS/LES modeling for the simulation of turbulent flows. *Flow, Turbulence and Combustion*, *99*(2), 279-327.
43 Ladeinde, F., Alabi, K., Ladeinde, T., Davis, D., Satchell, M., & Baurle, R. (2010). CFD

enhancements for supersonic combustion simulation with VULCAN. AIAA 2010-6876, In *46th AIAA/ASME/SAE/ASEE Joint Propulsion Conference & Exhibit* doi: 10.2514/6.2010-6876.
44 Johnson R W. (1998), *The Handbook of Fluid Dynamics*, Ed. CRC Press, Boca Raton, Florida.
45 Peyret, R., & Krause, E. (Eds.). (2000). *Advanced Turbulent Flow Computations*. CISM courses and Lectures, Springer Wein, New York.
46 Wilcox, D. C. (2006). *Turbulence Modeling for CFD*. 3rd ed, LA, USA: DCW industries.
47 Spalart, P., & Allmaras, S. (1992). A one-equation turbulence model for aerodynamic flows. AIAA 1992-0439, In *30th Aerospace Sciences Meeting and Exhibit*, doi :10.2514/6.1992-439.
48 Lauder, B. E., & Spalding, D. B. (1972). Lectures in mathematical models of turbulence. London: AP.
49 Ansys 18.0 Theory Guide, 2016
50 Wilcox, D. C. (1998). *Turbulence Modeling for CFD*. 3rd ed, La Canada, CA: DCW industries.
51 Zhukov, V. P. (2015). Computational fluid dynamics simulations of a GO2/GH2 single element combustor. *Journal of Propulsion and Power*, *31*(6), 1707-1714.
52 Benmansour, A., Liazid, A., Logerais, P. O., & Durastanti, J. F. (2016). A 3D numerical study of LO2/GH2 supercritical combustion in the ONERA-Mascotte Test-rig configuration. *Journal of Thermal Science*, *25*(1), 97-108.
53 Shine, S. R., & Nidhi, S. S. (2018). Review on film cooling of liquid rocket engines. *Propulsion and Power Research*, *7*(1), 1-18.
54 Wang, X. W., Cai, G. B., & Jin, P. (2010). Scaling of the flowfield in a combustion chamber with a gas–gas injector. *Chinese Physics B*, *19*(1), 019401.
55 Wang, X. W., Jin, P., & Cai, G. B. (2009). Method for investigation of combustion flowfield characteristics in single element gas/gas injector chamber. *J Beijing Univ Aeronaut Astronaut*, *35*(9), 1095-9.
56 Yu, N., Zhang, Y., Li, F., & Dai, J. (2018). Numerical and experimental investigations of single-element and double-element injectors using gaseous oxygen/gaseous methane. *Aerospace Science and Technology*, *75*, 24-34.
57 Tucker, P., Menon, S., Merkle, C., Oefelein, J., & Yang, V. (2007). An approach to improved credibility of CFD calculations for rocket injector design. AIAA 2007-5572, In *43rd AIAA/ASME/SAE/ASEE Joint Propulsion Conference & Exhibit* doi: 10.2514/6.2007-5572.
58 Hong, Y., Dai, B., Beck, P., Sternin, A., Slavinskaya, N.， Haidn, O.J., & Wei, X.G. (2018), Development and validation of a reduced chemicalkineticmechanism for CFD simulation of combustion in a GCH4/GO2 combustor. AIAA 2018-4766, In *2018 Joint Propulsion Conference*, doi: 10.2514/6.2018-4766.
59 Yimer, I., Campbell, I., & Jiang, L. Y. (2002). Estimation of the turbulent Schmidt number from experimental profiles of axial velocity and concentration for high-Reynolds-number jet flows. *Canadian Aeronautics and Space Journal*, *48*(3), 195-200.
60 McBride, B. J., Zehe, M.J., & Gordon, S. (2002).NASA Glenn coefficients for calculating thermodynamic properties of individual species, NASA TP-2002-211556.
61 Bird, R. B., Stewart, W. E., & Lightfoot, E. N. (2006). *Transport Phenomena*. 2nd ed, John Wiley & Sons, Madison, New York.
62 Petersen, E. L., & Hanson, R. K. (1999). Reduced kinetics mechanisms for ram accelerator combustion. *Journal of Propulsion and Power*, *15*(4), 591-600.
63 Slavinskaya, N., Abbasi, M., Starcke, J. H., Mirzayeva, A., & Haidn, O. J. (2016). Skeletal mechanism of the methane oxidation for space propulsion applications. AIAA 2016-4781, In *52nd AIAA/SAE/ASEE Joint Propulsion Conference* doi: 10.2514/6.2016-4781.
64 Wolfshtein, M. (1969). The velocity and temperature distribution in one-dimensional flow with turbulence augmentation and pressure gradient. *International Journal of Heat and Mass Transfer*, *12*(3), 301-318.
65 Pointwise, Software Package, Ver. 18.0, Pointwise, Inc., TX, 2016.
66 Beck, P., Wagner, B., & Haidn, O. (2017). The influence of secondary flows in the thrust acting on the axis of a radial Lox pump. In *12th European Conference on Turbomachinery Fluid Dynamics & Thermodynamics,* Stockholm, Sweden, doi: 10.29008/ETC2017-141.
67 Roache, P. J. (1998). Systematic rid convergence studies and the grid convergence index (GCI). Verification and validation in computational science and engineering, Ed., Hermosa, Albuquerque.
68 Warnatz, J., Maas, U., & Dibble, R. W. (2006). Physical and chemical fundamentals, modeling

and simulation, experiments, pollutant formation. Springer, Berlin.
69 Troe, J. (1979). Predictive possibilities of unimolecular rate theory. *Journal of Physical Chemistry*, *83*(1), 114-126.
70 Celano, M. P., Silvestri, S., Schlieben, G., Kirchberger, C., Haidn, O. J., & Knab, O. (2016). Injector characterization for a gaseous oxygen-methane single element combustion chamber. *Progress in Propulsion Physics*, 8, 145-164.
71 Goodwin, D. G., Moffat, H. K., & Speth, R. L. (2009). Cantera: An object-oriented software toolkit for chemical kinetics, thermodynamics, and transport processes. Caltech, Pasadena, CA.
72 Kee, R.J., Coltrin, M.E., & Glarborg, P., (2003). Chemically reacting flow theory and practice, John Wiley & Soins, Inc. Hoboken, New Jersey.
73 Spadaccini, L.J., & Colket, M.B.(1994). Ignition delay characteristics of methane fuels. *Progress in Energy and Combustion Science, 20 (5)*, 431-460.
74 Lindstedt, R. P., & Maurice, L. Q. (2000). Detailed chemical-kinetic model for aviation fuels. *Journal of Propulsion and Power*, *16*(2), 187-195.
75 Law, C. K., Sung, C. J., Wang, H., & Lu, T. F. (2003). Development of comprehensive detailed and reduced reaction mechanisms for combustion modeling. *AIAA Journal*, *41*(9), 1629-1646.
76 Lam, S. H. (1993). Using CSP to understand complex chemical kinetics. *Combustion Science and Technology*, *89*(5-6), 375-404.
77 Turanyi, T., Berces, T., & Vajda, S. (1989). Reaction rate analysis of complex kinetic systems. *International Journal of Chemical Kinetics*, *21*(2), 83-99.
78 Huang, J., Hill, P. G., Bushe, W. K., & Munshi, S. R. (2004). Shock-tube study of methane ignition under engine-relevant conditions: experiments and modeling. *Combustion and Flame*, *136*(1-2), 25-42.
79 Wang, J., Hu, E., Huang, Z., Ma, Z., Tian, Z., Wang, J., & Li, Y. (2008). An experimental study of premixed laminar methane/oxygen/argon flames doped with hydrogen at low pressure with synchrotron photoionization. *Chinese Science Bulletin*, *53*(8), 1262-1269.
80 Perez-Ramirez, Y., Santoni, P., Darabiha, N., Leroy-Cancellieri, V., & Leoni, E. (2012). A global kinetic model for the combustion of the evolved gases in wildland fires. *Combustion Science and Technology*, *184*(9), 1380-1394.
81 Zhukov, V. P., & Kong, A. F. (2018). A compact reaction mechanism of methane oxidation at high pressures. *Progress in Reaction Kinetics and Mechanism*, *43*(1), 62-78.
82 Li, J., Zhao, Z., Kazakov, A., Chaos, M., Dryer, F. L., & Scire Jr, J. J. (2007). A comprehensive kinetic mechanism for CO, CH2O, and CH3OH combustion. *International Journal of Chemical Kinetics*, *39*(3), 109-136.
83 Xu, C., & Konnov, A. A. (2012). Validation and analysis of detailed kinetic models for ethylene combustion. *Energy*, *43*(1), 19-29.
84 Blanquart, G., Pepiot-Desjardins, P., & Pitsch, H. (2009). Chemical mechanism for high temperature combustion of engine relevant fuels with emphasis on soot precursors. *Combustion and Flame*, *156*(3), 588-607.
85 Miller, J. A., & Klippenstein, S. J. (2004). The H+ C2H2 (+ M)= C2H3 (+ M) and H+ C2H2 (+ M)= C2H5(+ M) reactions: Electronic structure, variational transition-state theory, and solutions to a two-dimensional master equation. *Physical Chemistry Chemical Physics*, *6*(6), 1192-1202.
86 Cao, J.-R., & Back, M.H.(1983). Kinetics of the reaqction H+C2H6→H2+C2H5 in the temperature region of 1000K. *Canadian Journal of Chemistry, 62*(1), 86-91.
87 Petersen, E. L., Davidson, D. F., & Hanson, R. K. (1999). Kinetics modeling of shock-induced ignition in low-dilution CH4/O2 mixtures at high pressures and intermediate temperatures. *Combustion and Flame*, *117*(1-2), 272-290.
88 Sankaran, R., Hawkes, E. R., Chen, J. H., Lu, T., & Law, C. K. (2007). Structure of a spatially developing turbulent lean methane–air Bunsen flame. *Proceedings of the Combustion Institute*, *31*(1), 1291-1298.
89 Metcalfe, W. K., Burke, S. M., Ahmed, S. S., & Curran, H. J. (2013). A hierarchical and comparative kinetic modeling study of C1− C2 hydrocarbon and oxygenated fuels. *International Journal of Chemical Kinetics*, *45*(10), 638-675.
90 Petersen, E. L., Davidson, D. F., & Hanson, R. K. (1999). Ignition delay times of Ram accelerator CH/O/diluent mixtures. *Journal of Propulsion and Power*, *15*(1), 82-91.

91 Petersen, E. L., Hall, J. M., Smith, S. D., de Vries, J., Amadio, A. R., & Crofton, M. W. (2007). Ignition of lean methane-based fuel blends at gas turbine pressures. *Journal of Engineering for Gas Turbines and Power*, *129*(4), 937-944.
92 El Merhubi, H., Kéromnès, A., Catalano, G., Lefort, B., & Le Moyne, L. (2016). A high pressure experimental and numerical study of methane ignition. *Fuel*, 177, 164-172.
93 Burke, U., Somers, K. P., O'Toole, P., Zinner, C. M., Marquet, N., Bourque, G., ... & Curran, H. J. (2015). An ignition delay and kinetic modeling study of methane, dimethyl ether, and their mixtures at high pressures. *Combustion and Flame*, *162*(2), 315-330.
94 Goy, C. J., Moran, A. J., & Thomas, G. O. (2001). Autoignition characteristics of gaseous fuels at representative gas turbine conditions. In *ASME Turbo Expo 2001: Power for Land, Sea, and Air* (pp. V002T02A018-V002T02A018), doi:10.1115/2001-GT-0051.
95 Rozenchan, G., Zhu, D. L., Law, C. K., & Tse, S. D. (2002). Outward propagation, burning velocities, and chemical effects of methane flames up to 60 atm. *Proceedings of the Combustion Institute*, *29*(2), 1461-1470.
96 Mc Bride, B. J., & Gordon, S. (1994). Computer Program for Calculation of Complex Equilibrium Composition and Applications. *NASA RP*, *1311*.
97 Roth, C. M., Haidn, O. J., Chemnitz, A., Sattelmayer, T., Frank, G., Müller, H., ... & Cuenot, B. (2016). Numerical investigation of Flow and Combustion in a Single Element GCH4/Gox Rocket Combustor. AIAA 2016-4995, In *52nd AIAA/SAE/ASEE Joint Propulsion Conference* doi: 10.2514/6.2016-4995.
98 Maestro, D., Cuenot, B., & Selle, L. (2017.) Large eddy simulation of flow and combustion in a single-element GCH4/GOX rocket combustor. In *7th European Conference for Aeronautics and Space Sciences*, Milan, doi: 10.13009/EUCASS2017-605.
99 De Giorgi, M., Sciolti, A., & Ficarella, A. (2014). Application and comparison of different combustion models of high pressure LOX/CH4 jet flames. *Energies*, *7*(1), 477-497.
100 Minotti, A., & Sciubba, E. (2010). LES of a meso combustion chamber with a detailed chemistry model: Comparison between the flamelet and EDC models. *Energies*, *3*(12), 1943-1959.
101 Frenklach, M., Wang, H., Yu, C.-L., Goldenberg, M., Bowman, C.T., Hanson, R.K....& Lissianski, L., http://www.me.berkeley.edu/gri mech/.
102 Marchal, C., Delfau, J. L., Vovelle, C., Moréac, G., Mounaı, C., & Mauss, F. (2009). Modelling of aromatics and soot formation from large fuel molecules. *Proceedings of the Combustion Institute*, *32*(1), 753-759.
103 Slavinskaya, N. A., Chernov, V., Whitside, R., Starke, J. H., Mirzayeva, A., Abassi, M., & Auyelkhankyzy, M., A modeling study of acetylene oxidation and pyrolysis. *Combustion and Flame* (in press).
104 Hong, D., Liu, L., Huang, Y., Zheng, C., & Guo, X. (2016). Chemical effect of H2O on CH4 oxidation during combustion in O2/H2O environments. *Energy & Fuels*, *30*(10), 8491-8498.
105 Glarborg, P., Kubel, D., Kristensen, P. G., Hansen, J., & Dam-Johansen, K. (1995). Interactions of CO, NOx and H2O under post-flame conditions. *Combustion Science and Technology*, *110*(1), 461-485.
106 Abián, M., Giménez-López, J., Bilbao, R., & Alzueta, M. U. (2011). Effect of different concentration levels of CO2 and H2O on the oxidation of CO: Experiments and modeling. *Proceedings of the Combustion Institute*, *33*(1), 317-323.
107 Le Cong, T., & Dagaut, P. (2009). Experimental and detailed modeling study of the effect of water vapor on the kinetics of combustion of hydrogen and natural gas, impact on NOx. *Energy & Fuels*, *23*(2), 725-734.
108 Fiala, T., & Sattelmayer, T. (2013). A posteriori computation of OH* radiation from numerical simulations in rocket combustion chambers. In *5th European Conference for Aeronautics and Space Sciences, Munich*, doi: 10.13140/2.1.1852.0966.
109 Pohl, S., Jarczyk, M. M., & Pfitzner, M. (2011). A real gas laminar flamelet combustion model for the CFD-Simulation of LOX/GH2 combustion. In *5th European Combustion Meeting* (Vol. 86).